

POLITECNICO DI MILANO

School of Industrial and Information Engineering

Department of Electronics, Information and Bioengineering (DEIB)

Master of Science in Electronics Engineering



Processing Methods for Position Reconstruction of Detected Gamma Events in Gamma Ray Detectors

Supervisor: Prof. Carlo Ettore Fiorini

Co-Supervisor: Ing. Luca Buonanno

Master Thesis by:

Adriano Minerva

Matr. 881090

Academic Year 2018 - 2019

Contents

List of Figures	V
List of Tables	IX
Sommario	XI
Abstract	XV
1 INSERT and GAMMA projects	1
1.1 Gamma rays detection and applications	1
1.1.1 Gamma radiation interaction with matter	2
1.1.2 Spectroscopy	6
1.1.3 Imaging	9
1.1.4 Multimodal Medical Imaging Techniques	12
1.1.5 Silicon Photomultipliers	17
1.2 INSERT project	19
1.2.1 Ring architecture	21
1.2.2 Gamma detection module	22
1.2.3 3D tomography	26
1.3 GAMMA project	26
1.3.1 Doppler Effect Induced Peak Broadening	29
1.3.2 Lanthanum Bromide Scintillator Crystal	30
1.3.3 GAMMA-Project Silicon Photodetectors	35
2 INSERT: DOI Reconstruction	39
2.1 DOI: motivation and reconstruction method	39

2.1.1	Importance of DOI information	39
2.1.2	DOI reconstruction method	42
2.2	Simulation results	45
2.2.1	ANTS2 Toolkit	45
2.2.2	Calibration phase	48
2.2.3	Results	53
2.3	Experimental results	62
2.3.1	Tilted beam and experimental set-up	62
2.3.2	Measurements and results	63
2.3.3	Crystal borders	70
3	GAMMA: position reconstruction	75
3.1	GAMMA imaging: motivation and experimental setup de- description	75
3.1.1	Position reconstruction in GAMMA system	75
3.1.2	Experimental setup	78
3.2	Cross-correlation reconstruction algorithm	81
3.2.1	Algorithm working principle	82
3.2.2	Border light contribution	85
3.2.3	Reconstruction of intermediate positions	86
3.2.4	Reconstruction of XY coordinates	88
3.3	Machine Learning reconstruction algorithms	89
3.3.1	Data distribution analysis	90
3.3.2	K-NN reconstruction method	93
3.3.3	Principal Component Analysis	108
3.3.4	Decision tree reconstruction method	110
3.3.5	Final considerations	115
4	Embedded Machine Learning	119
4.1	Introduction	119
4.2	System Architecture	121
4.3	Embedded reconstruction algorithm	125
4.4	Experimental Results	129

5	Conclusions and Future Developments	133
5.1	Conclusions	133
5.1.1	INSERT project	133
5.1.2	GAMMA project	134
5.1.3	Embedded Machine Learning	136
	Bibliography	137
	List of Abbreviations	145

List of Figures

1.1	Electromagnetic Spectrum	2
1.2	Radiation interactions with matter	5
1.3	Total photon attenuation of Si	6
1.4	Incidence of interaction processes vs energy	7
1.5	Example of energy spectrum	8
1.6	Energy resolution	8
1.7	Collimator principle and types	10
1.8	Classical gamma camera and Anger camera	11
1.9	Example of co-registration of SPECT and MRI images	14
1.10	Multimodal Scanner Architectures	16
1.11	SiPM equivalent circuit and picture	18
1.12	SPAD equivalent circuit and operation cycle	19
1.13	Clinical INSERT System Model	20
1.14	INSERT ring architectures	21
1.15	Clinical INSERT Scintillation Crystal	23
1.16	INSERT SiPM Tile	24
1.17	Single INSERT Module	26
1.18	Reconstruction Chain - Schematic	27
1.19	GAMMA final instrument	28
1.20	Doppler induced photopeaks broadening	30
1.21	Intrinsic resolution of scintillator crystals	32
1.22	Scintillator crystal cross section	34
1.23	LaBr ₃ crystal internal radioactivity	35
1.24	Crystals light yield linearity	36

2.1	Parallax error	41
2.2	Projections of the slits and slats FOV	41
2.3	DOI Groups	42
2.4	Scintillation light distribution	43
2.5	Grid Collimator Holes Position	45
2.6	Clinical INSERT Detection Module Model	47
2.7	Single-Hole Collimator Model	48
2.8	Calibration Spot Position	52
2.9	Signals Correlation with DOI	54
2.10	Ideal DOI Reconstruction	55
2.11	Lambert-Beer Law	55
2.12	Lambert-Beer Law-based Initialization	56
2.13	Single Spot Calibration - Results on Simulated Data - SiPM center	60
2.14	Single Spot Calibration - Results on Simulated Data - SiPM corner	61
2.15	Mapping between DOI ranges and X ranges	62
2.16	Lead Collimators	63
2.17	Single Module Set-up	64
2.18	Planar Reconstruction of the Tilted Irradiation	65
2.19	Planar Reconstruction of the Calibration Spots	66
2.20	Histograms of the Reconstructed X Coordinate for the Dif- ferent DOI Groups	67
2.21	Depth of Interaction Reconstruction for the Oblique Irra- diation	68
2.22	ANTS2 Oblique Irradiation Simulation	68
2.23	Corrected Spot Image	70
2.24	Original and Recovered Spot	71
2.25	Calibration Spot on Crystal Corner	71
2.26	DOI Calibration for Spots at the Borders	73
2.27	DOI Calibration for Borders - Part 2	73
3.1	LaBr ₃ crystal optical model	77

3.2	Dependence of the light patterns on the position of interaction	78
3.3	SiPMs merging strategies	80
3.4	Setup for the imaging measurements	81
3.5	Spots irradiated during calibration in the two readout configurations	82
3.6	Average signal distribution	83
3.7	Histograms of the reconstructed X coordinates using cross-correlation method	85
3.8	Histograms of the reconstructed X coordinates using cross-correlation method and employing a ring mask	86
3.9	Histograms of the reconstructed X coordinates of events not belonging to calibration positions using cross-correlation method and employing a ring mask	87
3.10	Histograms of reconstructed XY coordinates using cross-correlation method	89
3.11	Matrix of the pixel signals dataset	91
3.12	Training data scatter plots	92
3.13	Example of 3-dimensional features space	94
3.14	Example of K-NN classification in a 3-dimensional system	95
3.15	Confusion matrix for the X coordinate reconstruction using K-NN algorithm with $K = 100$ and Euclidean metric . . .	96
3.16	Histograms of the reconstructed X coordinates using the K-NN method with $K = 100$ and Euclidean metric	97
3.17	K-NN hyperparameters optimization results	99
3.18	K-NN K and p exponent optimization results	100
3.19	Classification results adopting the K-NN method with optimized hyperparameters	101
3.20	K-NN hyperparameters optimization results for the XY coordinates reconstruction	102
3.21	Classification results for the XY coordinates reconstruction adopting the K-NN method with optimized hyperparameters	104
3.22	Histograms of the reconstructed X coordinates using the K-NN method with $K = 100$ and Euclidean metric	105

3.23	Absorption efficiency of BrillanCe TM 380 (LaBr ₃ (Ce)) . . .	106
3.24	Histograms of the reconstructed X coordinates using the K-NN method with Euclidean metric and sweeping K . . .	106
3.25	Comparison between reconstructed and theoretical X coord- inates distribution for side irradiation events	107
3.26	Example of a 2-dimensional data distribution	108
3.27	Example of classes separation in a 2-dimensional data dis- tribution	110
3.28	Training data scatter plots after PCA	110
3.29	Decision tree example	111
3.30	Decision tree hyperparameters optimization results	113
3.31	Classification results adopting the decision tree method with optimized hyperparameters	114
3.32	Classification results for the XY coordinates reconstruction adopting the decision tree method with optimized hyper- parameters	116
4.1	Schematic illustration of system application	121
4.2	Overall system components and working principle	122
4.3	Photographs of the prototype front-end	123
4.4	Architecture of the prototype based on LAILA module . .	124
4.5	Relocation of reconstruction algorithm computations . . .	127
4.6	Embedded reconstruction experimental results	130
4.7	Embedded direction reconstruction decision tree hyperpa- rameters optimization results	131
4.8	Embedded reconstruction cross-validated confusion matrix	132

List of Tables

1.1	Summary of X and γ -photons interaction with matter. . .	5
1.2	CsI(Tl) Characteristics	23
1.3	RGB-HD Technical Parameters	25
1.4	Impact of Doppler effect on energy resolution	31
1.5	Scintillator crystals specifications	33
2.1	DOI Groups Ranges	43
2.2	Single Spot Calibration - Results on Simulated Data - SiPM center	61
2.3	Single Spot Calibration - Results on Simulated Data - SiPM corner	61

Sommario

La rivelazione di radiazione gamma trova molte applicazioni in diversi ambiti, tra cui l'astrofisica, la diagnostica medica e la fisica nucleare.

Nel campo della diagnostica medica, la realizzazione di scanner per imaging multimodale rappresenta uno dei principali argomenti di ricerca e sviluppo, poiché l'integrazione di informazioni funzionali e anatomico-morfologiche permette di aumentare l'accuratezza delle diagnosi e di migliorare il monitoraggio e la valutazione dell'efficacia delle terapie mediche. In questo ambito si colloca il progetto INSERT, finanziato dalla Comunità Europea nel contesto del programma FP7- HEALTH, che ha portato alla realizzazione del primo scanner SPECT clinico basato su SiPM compatibile con la risonanza magnetica.

Nel contesto di esperimenti di fisica nucleare con energie che vanno da 100 keV a 20 MeV si inserisce il progetto GAMMA, sostenuto dall'Istituto Nazionale di Fisica Nucleare (INFN), che consiste nella progettazione, sviluppo e caratterizzazione sperimentale di uno spettrometro gamma, basato su cristalli scintillatori di Bromuro di Lantanio di grandi dimensioni accoppiati a Silicon Photomultipliers (SiPMs), caratterizzato da risoluzione energetica allo stato dell'arte e capacità di imaging, in una struttura compatta, modulare e robusta.

L'obiettivo di questo lavoro di tesi è quello di implementare algoritmi per la ricostruzione di immagine in diversi ambiti accomunati dal contesto della rivelazione di raggi gamma tramite cristalli scintillatori accoppiati a una matrice di SiPMs. In particolare, per quanto riguarda il progetto INSERT, lo scopo finale da raggiungere è quello della ricostruzione della terza coordinata di scintillazione del singolo fotone gamma assorbito.

Dalla conoscenza di questo parametro è possibile effettuare una compensazione dell'errore di parallasse e ottenere un miglioramento della qualità dell'immagine finale. In merito al progetto GAMMA l'obiettivo è quello di ricostruire la posizione di scintillazione del singolo fotone gamma lungo la sua direzione di emissione. Grazie a questa informazione, negli esperimenti di fisica nucleare che utilizzano acceleratori di particelle, è possibile ricavare l'angolo tra la direzione della sorgente in movimento e quella di emissione del fotone e, conseguentemente, correggere l'effetto Doppler. Infine, nel contesto di un nuovo dispositivo costituito da un rivelatore in grado di localizzare la posizione di una sorgente di radiazione gamma nello spazio, l'obiettivo da conseguire è l'implementazione di un algoritmo di ricostruzione che possa essere eseguito direttamente dal microcontrollore montato sul rivelatore. In questa maniera può essere eseguita una ricostruzione in tempo reale e, nel caso di reti cooperative, la complessità di calcolo può essere distribuita in più nodi periferici così da rilassare i requisiti in termini di quantità di dati da trasmettere e ottenere un sistema più veloce e performante.

Struttura della tesi

Il testo della tesi è così strutturato:

Nel primo capitolo, dopo una breve introduzione riguardante la rivelazione della radiazione gamma e le sue principali applicazioni, vengono presentati i progetti INSERT e GAMMA. Sono illustrate, in seguito, le motivazioni per la scelta dei Silicon Photomultipliers come rivelatori. Infine è presentata una descrizione degli obiettivi, delle specifiche principali e dei componenti base dei due progetti.

Il secondo capitolo tratta del contributo apportato dal lavoro di tesi al progetto INSERT: viene proposto il metodo per la ricostruzione della terza coordinata di scintillazione e sono illustrati i risultati ottenuti sia tramite simulazione che sperimentalmente.

Il terzo capitolo tratta degli algoritmi per la ricostruzione della posizione di interazione di un fotone gamma all'interno del cristallo scintillatore del progetto GAMMA. Nella prima parte viene proposto un metodo basato sulla cross-correlazione di due segnali ottenuti dalla matrice dei pixel accoppiata al cristallo. Nella seconda parte vengono trattati diversi algoritmi basati sulle tecniche di Machine Learning. Per tutti gli algoritmi discussi vengono illustrati i risultati sperimentali ottenuti.

Nel quarto capitolo viene presentato un sistema innovativo costituito da un rivelatore di raggi gamma in grado di localizzare la direzione di provenienza della radiazione assorbita. Il processo di ricostruzione della direzione viene effettuato, in tempo reale, direttamente dal microcontrollore utilizzando la tecnica dell'albero decisionale, ottimizzata per il contesto specifico.

Nel quinto capitolo i risultati ottenuti nei tre progetti discussi vengono riassunti e viene fornita una visione delle loro prospettive e sfide future.

Abstract

Gamma radiation detection finds many applications in different fields, including astrophysics, medical diagnostics and nuclear physics.

In the area of medical diagnostics, the realization of multimodal imaging scanners represents one of the main research and development topics, since the combination of techniques providing correlated functional and anatomical information, increases the accuracy of disease diagnosis and improves therapy monitoring and assessment. In this scenery is defined INSERT project, founded by 7th Framework Program of European Commission, which has brought to the development of the first SiPM-based clinical SPECT scanner suitable for insertion inside a commercial MRI.

In the context of nuclear physics experiments with energies ranging from 100 keV to 20 MeV, is placed GAMMA project, supported by Istituto Nazionale di Fisica Nucleare (INFN), which consists in the design, development and experimental characterization of a γ -ray spectrometer, based on large Lanthanum Bromide scintillator crystals coupled with Silicon Photomultipliers (SiPMs), characterized by state-of-the-art energy resolutions and imaging capability in a compact, modular and robust structure.

The goal of this thesis work is to implement algorithms for image reconstruction in different applications having in common the context of gamma radiation revelation employing scintillator crystals coupled with a SiPMs matrix. In particular, for what concerns INSERT project, the objective to be achieved is the reconstruction of the third coordinate of the scintillation position of the single absorbed gamma photon. From the knowledge of this parameter is possible to compensate the parallax error and obtain an

improvement of the final image quality. As regards GAMMA project the goal to reach is the reconstruction of the scintillation position of the single gamma photon along its emission direction. Exploiting this information, in nuclear physics experiments adopting particles accelerators, is possible to derive the angle between the direction of the moving source and that of the emitted photon and, therefore, correct the Doppler effect. Eventually, in the context of a new device constituted by a spectrometer able to localize the position of a gamma source in space, the objective to be attained is the implementation of a reconstruction algorithm that can be directly executed in the micro-controller mounted in the detector. In this way the reconstruction task can be performed in real time and, in case cooperative networks are adopted, the computational complexity can be distributed in the peripheral nodes, obtaining more relaxed constraints in terms of communication speed and getting a faster and with higher performances system.

Outline

The thesis is organized as follows:

In the first chapter, after a brief introduction to gamma radiation detection and its main applications, INSERT and GAMMA projects are presented. The motivations for the choice of Silicon Photomultipliers as detectors are discussed afterwards. Eventually a description of the objectives, the main specifications and the basic components for the two projects is carried out.

The second chapter illustrates the contribution brought by this thesis work to INSERT project: the method for the reconstruction of the third scintillation coordinate is proposed and the results obtained both by simulations and through experimental measurements are shown.

The third chapter describes the algorithms for the reconstruction of the interaction position of a gamma photon inside the scintillator

crystal of GAMMA project. In the first part a method based on the cross-correlation between two signals provided by the pixel matrix coupled to the crystal is proposed. In the second part different algorithms based on Machine Learning techniques are discussed. For all the treated algorithms the obtained experimental results are illustrated.

In the fourth chapter an innovative system constituted by a gamma radiation detector able to localize the direction of the absorbed gamma rays source is presented. The reconstruction process is executed in real time directly by the micro-controller employing the decision tree technique, optimized for the specific context.

In the fifth chapter the obtained results for the three projects are summarized and a view of their future perspectives and challenges is given.

Chapter 1

INSERT and GAMMA projects

This chapter contains an introduction to gamma radiation detection and its main applications: spectroscopy and imaging. A brief deepening on medical imaging and on Silicon Photomultipliers working principle is also carried out. Eventually the INSERT and the GAMMA projects are presented one after the other along with their main specifications and goals.

1.1 Gamma rays detection and applications

Gamma rays are an electromagnetic radiation characterized by energies typically higher than tens of keV. In the electromagnetic spectrum, the fraction of the gamma radiation produced by radioactive decay is usually located in a low energy range that spans from a few keV to tens of MeV. Thus there is an energy interval in which γ -rays and X-rays coexist (figure 1.1 on the following page). The distinction between these two types of radiation is made looking at their physical origin: γ -rays originate from the nucleus of a radionuclide after radioactive decay or from positron annihilation, whereas X-rays are emitted via fluorescence, when an excited atom falls back into its quiescent state, Bremsstrahlung phenomena and synchrotron light. A second difference is constituted by the physical process governing the interaction of radiation with matter: since γ -rays have on average more energy, they primarily interact through Compton scat-

tering, while X-rays mainly interact through photoelectric absorption.

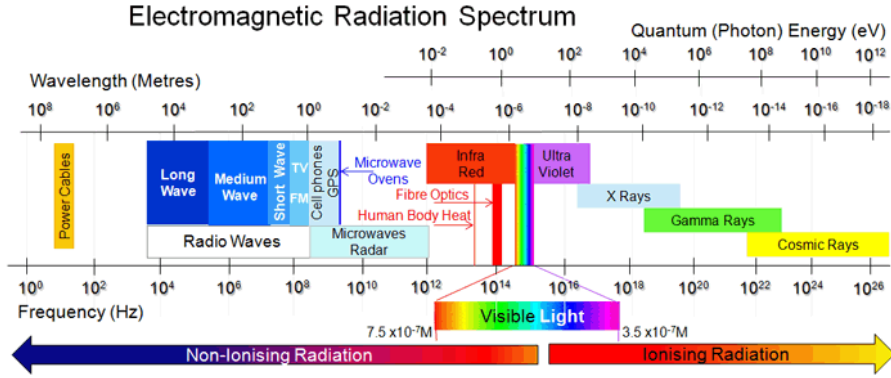


Figure 1.1: The electromagnetic spectrum. X-rays and γ -rays regions overlap.

1.1.1 Gamma radiation interaction with matter

As well known, the three main processes through which radiation is absorbed in matter are photoelectric absorption, Compton scattering and pair-production [1].

Photoelectric absorption is a process in which an incident photon is completely absorbed in the material. The incoming photon has sufficient energy to generate a photoelectron from an inner shell of an atom of the material, with kinetic energy E_k equal to the difference of the incoming photon energy and the binding energy of the photoelectron in its original shell.

$$E_{loss} = E_k = E_{ph} - E_{bind} \quad (1.1)$$

As a result of the photoelectron emission a vacancy is created. Electrons of close shells quickly fill up this vacancy by exchanging energy through radiative process (fluorescence) or non-radiative process (Auger effect). In case of fluorescence an X-ray will be emitted, travelling some distance, depending on the medium, before being re-absorbed through other photoelectric interactions. This mechanism

is favored at low energy and by materials with large atomic number (Z). The probability of occurrence of this process becomes maximum when the impinging photon energy E_{ph} is equal or slightly larger than binding energy E_{bind} of the shell. However there is a finite probability that the fluorescence photon escapes from the material, typically when the gamma-ray is absorbed close to the surface or when the absorbing medium is thin. If this occurs often enough, in the reconstructed spectrum a peak denoted as escape peak will be visible beside the gamma photon one.

Compton scattering (or *incoherent scattering*), is an interaction process in which the incoming photon exchange just a fraction of its energy. Differently from photoelectric absorption, in this mechanism the gamma photon is scattered by external, loosely bound valence electrons, e.g. outer shell electrons, losing part of its energy. The scattered photon energy corresponds to the difference between the incident photon energy and the emitted electron one. This directly implies that the probability of Compton interaction depends on the number of valence electrons of the medium. As well as energy, also the momentum of the incoming photon must be conserved. As a result, its energy transfer and interaction probability depend on the angle of collision (θ), governed by Klein-Nishina distribution and can be computed as [1]:

$$E_{loss} = E_{ph} \cdot \left(1 - \frac{1}{1 + \frac{E_{ph}}{m_0c^2}(1 - \cos \theta)} \right) \quad (1.2)$$

It is worth mentioning also **Rayleigh scattering** (or *coherent scattering*), which is the interaction process occurring when the incoming photon has less energy than the binding energy of the hit electron, and therefore it does not have enough energy to release a tightly bounded electron, so it gets deflected without energy transfer. As the direction of the photon is altered, but its energy is not, this effect should be considered in imaging applications.

Pair production process consists in the absorption of energy by the generation of an electron-positron pair. The minimum energy necessary for the electron-positron generation is equal to twice the rest-mass energy of an electron, so pair production absorption can occur only for photon energies larger than 1,022 MeV. Through this process, the impinging γ -photon will lose an energy equal to $2m_0c^2 = 1,022$ MeV (actually a higher energy is needed since the momentum of the two particles must be added to the energy needed for their production, however this contribution is usually negligible). The process, happening in the coulomb field of a nucleus, becomes dominant only for energies above some MeV.

The three interaction processes just described are summarized in figure 1.2 on the next page. In figure 1.3 on page 6 is represented the total photon attenuation as a function of the incoming radiation energy. It can be observed that for energies lower than 100 keV, typical of X-rays, the dominant process is the photoelectric absorption, while in the energy range of gamma photons, the dominant processes are Compton scattering and pair production. The total photon attenuation is not only function of the incoming radiation energy, but also of the atomic number of the absorbing material. In figure 1.4 on page 7 is shown the incidence of the three processes as a function of the incoming radiation energy and of the atomic number of the absorbing material [1]. Table 1.1 on the facing page summarizes the properties of each type of interaction treated in this section.

A radiation detector has two objectives to achieve: it has to absorb all of the incoming radiation and it has to provide an electrical signal proportional to the absorbed energy. A highly efficient detector should generate as many as possible free carriers in order to develop a significant electrical signal for a given energy. Usually the conversion factor ϵ , defined as the ratio between the radiation energy and the number of electron/holes pair generated in the absorbing medium, is used as figure of merit of the absorption material.

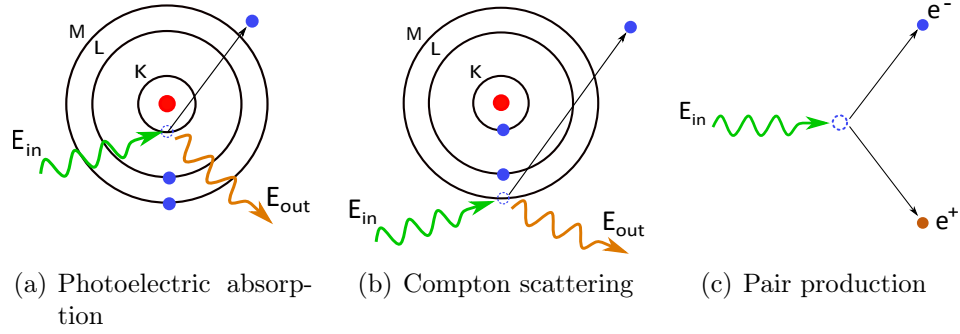


Figure 1.2: Radiation interaction with matter processes

Interaction	Energy loss	Energy range	σ
Photoelectric	$\simeq E_{bind}$	≤ 100 keV	$\propto Z^{4\sim 5}/(h\nu)^{3.5}$
Coherent (Rayleigh)	$\simeq 0$	Low energies	$\propto Z^2$
Incoherent (Compton)	$\left(E_{ph} - \frac{E_{ph}}{1 + \frac{E_{ph}}{m_0 c^2} (1 - \cos \theta)} \right)$	100 keV \div 10 MeV	$\propto \rho/h\nu$
Pair production	$\simeq 2m_0 c^2$	$\geq 1,022$ MeV	$\propto Z^2$

Table 1.1:

Summary of X and γ -photons interaction with matter. The cross-section σ is related to the probability of interaction.

Detectors in which the absorbing material is also the material generating the electrical signal are called *direct conversion detectors*. For instance, silicon features a conversion factor $\epsilon = 3,66$ eV/pair [2], which is remarkable. However, silicon is characterized by a low stopping power, due to the relatively low density and the low atomic number, and only radiation up to few tens of keV can be efficiently absorbed. For this reason silicon cannot be used as direct detector for gamma rays, but an intermediate medium called scintillator crystal, characterized by high density and large atomic number, is used to absorb the impinging radiation. The absorption of radiation causes the scintillator crystal to produce a scintillation light, which consists in a certain number of visible photons proportional to the absorbed radiation energy. The visible photons can then be easily detected by means of photodetectors like photomultiplier tubes, or solid

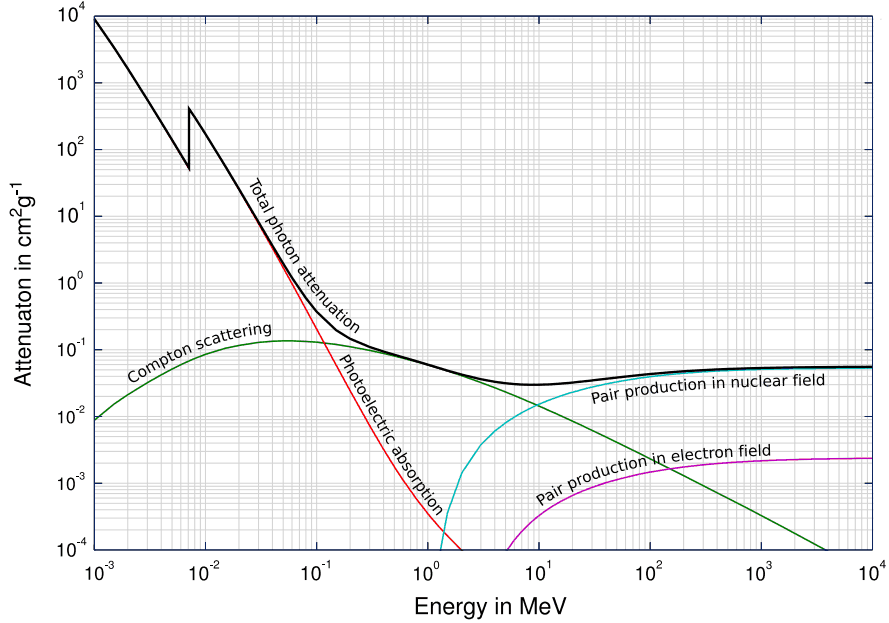


Figure 1.3: Total photon attenuation of silicon and its contributions.

state photodetectors like photodiodes. Such a detector is called *indirect conversion detector*.

1.1.2 Spectroscopy

From the data collected from a γ -ray detector, the spectrum of the γ -ray emitter can be built by simply plotting an histogram of the sampled data event by event. Since each radionuclide is characterized by a typical emission peak, through the study of the spectrum of a sample it is possible to identify the γ -emitter in the analyzed sample. Spectroscopy measurements are of particular interest for nuclear physics [3] and astronomy applications [4]. The main quantitative data that can be recovered from an energy spectrum analysis are resumed in figure 1.5.

Considering an efficient detector, most of the times the whole incoming radiation is absorbed through the combined effects of Compton and photoelectric absorption, and effectively readout by the detector: all these contributions constitute the main peak in the spectrum, referred to as

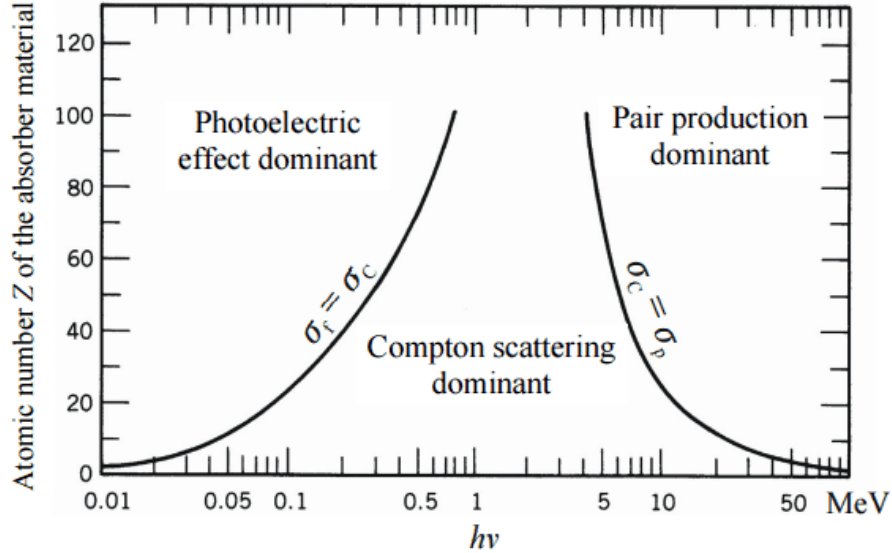


Figure 1.4: Incidence of interaction processes as function of the incoming radiation energy.

photopeak. Since each Compton interaction involves an energy loss which depends on the scattering angle (refer to equation 1.2 on page 3) and in normal conditions all the scattering angles will occur in the detector, an energy continuum distribution is usually visible in the spectrum, constituted by Compton scattered photons not absorbed by the medium. As the maximum energy that can be lost through Compton mechanism is smaller than the photopeak energy, the energy continuum is bounded by the Compton edge.

The lower energy peaks, are caused by the non complete absorption of Compton scattered photons within the detector volume: the peaks can be due to an X-ray photon that manages to escape, building up the X-ray escape peaks, or by the electron - positron annihilation, that generates two 511 keV γ -rays, that will result in peaks corresponding to $E_{ph} - 511$ keV or $E_{ph} - 1,022$ MeV if one or both of the two generated photons manage to escape from the absorbing medium.

The main figure of merit of a spectrum, that is used to quantify the accuracy and the performances of the detector is energy resolution. The higher is the resolving power of a detector, which corresponds to a low

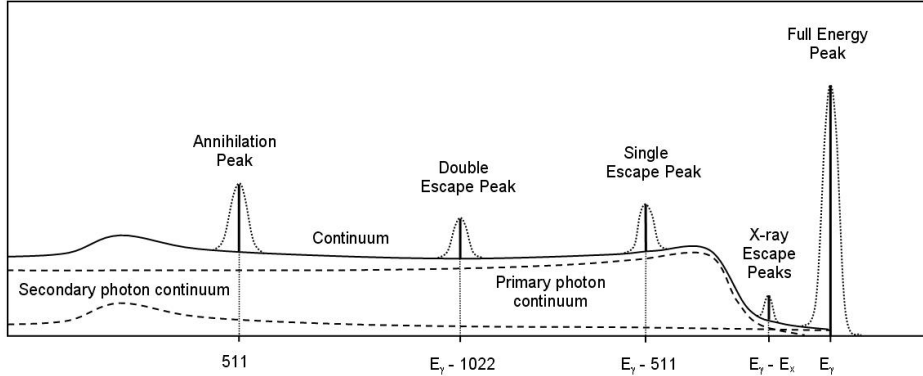


Figure 1.5: Example of an energy spectrum, illustrating different peaks that can be observed.

value of the resolution R , the higher is the ability to distinguish two close photopeaks, and in the end, the higher the capability to detect different emitters. Ideally a perfect detector should feature a delta-like spectrum, however, unavoidable non-idealities will cause a non-zero width of the peak, and the energy resolution can be defined as the ratio between the Full Width at Half Maximum (FWHM) of the photopeak and the mean energy of the photopeak E_0 , as represented in figure 1.6.

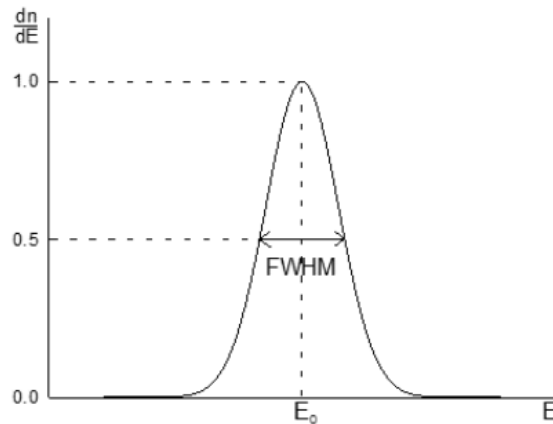


Figure 1.6: Detector resolution: the narrower the peak, the higher the resolving power of the detector.

Considering that for a high number of counts in the energy spectrum, the Poisson distribution (which describes the statistics of this type of inter-

actions) can be approximated with a Gaussian distribution, the resolution can be written as a function of the standard deviation σ (recalling that $FWHM = 2.355 \cdot \sigma$):

$$R_{tot} = \frac{FWHM}{E_0} = \frac{2.355 \cdot \sigma}{E_0} \quad (1.3)$$

The total energy resolution is given by three main independent stochastic processes contributions: scintillator non-idealities, photoelectrons generation statistics and electronic noise [1]. If we consider a Gaussian distribution it holds:

$$\sigma_{out} = \sqrt{\sigma_{int}^2 + \sigma_{stat,out}^2 + \sigma_{noise,out}^2} \quad (1.4)$$

thus, the overall resolution of the detector is influenced by the performances of all the components of the readout chain, from the scintillator crystal to the electronic front-end [1], and it can be computed as:

$$R_{tot} = \frac{2.355 \cdot \sigma_{out}}{S_{out}} = \sqrt{R_{int}^2 + R_{stat}^2 + R_{noise}^2} \quad (1.5)$$

R_{int} accounts for the crystal non-idealities: the main reason for this effect is the non-proportional light output of the scintillator to different energies [5] and also the local fluctuations in the scintillation yield; R_{stat} is related to the collection of photoelectrons statistics and R_{noise} is the resolution limit imposed by the noise of the electronics front-end.

1.1.3 Imaging

Gamma ray detection opened new possibilities in medicine, in particular in medical diagnostics. Single Photon Emission Tomography (SPECT) and Positron Emission Tomography (PET) have been developed in years and nowadays they are commonly used. The interest in medical diagnostics is related to the possibility of creating images of the distribution of γ -rays emitters distributed throughout the patient: a receptor-binding substance tagged with a radionuclide is injected intravenously in the patient's body;

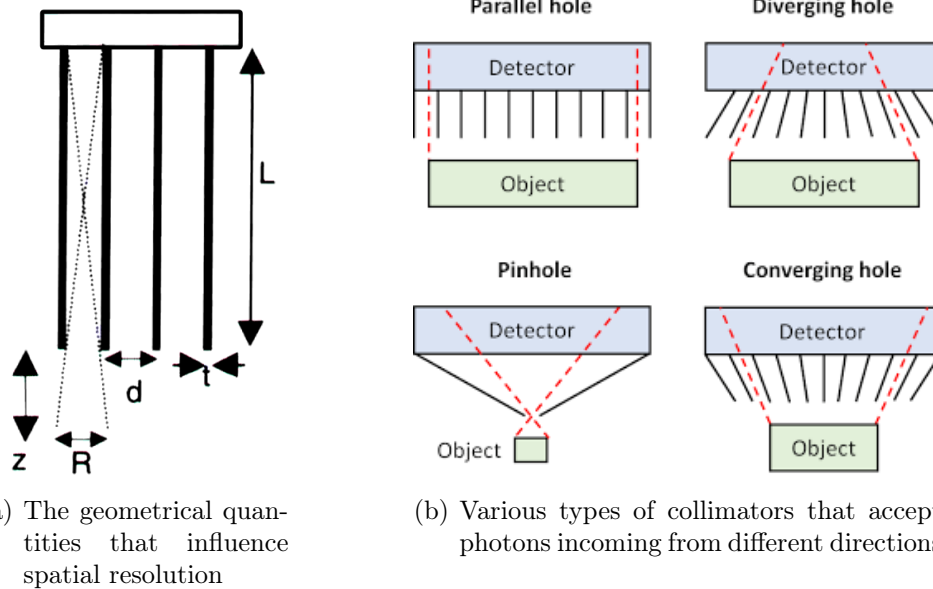


Figure 1.7: Through the collimator only photons coming from a specific direction can reach the scintillator crystal and be detected. The spatial resolution is influenced by the aperture dimension, the collimator length and the distance from source.

the flow tracer is assumed to accumulate in different areas proportionally to the rate of delivery of nutrients to tissues; eventually the high energy radiation emitted by the tracers is detected by the imaging device to reconstruct a 3D volume of its distribution.

In SPECT, spatial resolution is introduced in the system by the use of lead collimators, that absorb γ -photons not coming from a specific direction, as depicted in figure 1.7. As a result, only photons emitted from a specific direction are detected by the system and the emission position can be ascertained.

The main drawback of using collimator is the reduced efficiency of the detector, since many emitted photons are absorbed by the collimator itself and not detected. In order to collect a significant amount of signal, the dose injected into the patient may be increased. Moreover it exists a trade-off between the geometrical efficiency of the collimator and the achievable spatial resolution.

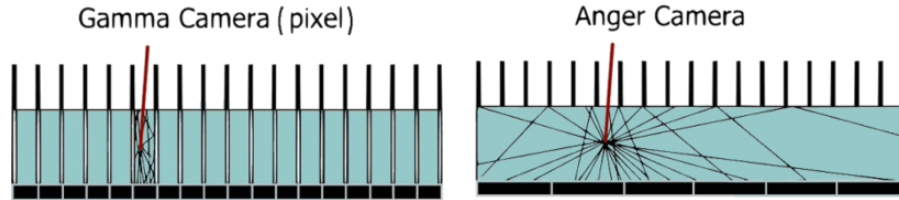


Figure 1.8: *Gamma cameras are based on pixelated scintillators coupled 1:1 with photodetectors, or on Anger architecture, with a monolithic scintillator crystal and a lower-complexity pixelated photodetector.*

Conversely, PET systems do not make use of physical collimators as they perform an electronic collimation: by detecting and localizing externally the two γ -rays, generated simultaneously and in opposite directions by the annihilation event, it can be obtained the line joining the detected locations, which passes directly through the point of annihilation. For this reason PET systems reach higher efficiency, but they pose other challenges on electronics design due to timing requirements, especially for Time Of Flight PET (TOF-PET), in which timing resolution specifications can reach values as low as 30 ps [6] with the purpose of using the time of flight measurement to improve the overall spatial resolution of the instrument.

Gamma imaging systems can be realized with pixelated or Anger architectures: nowadays, the majority of these systems are based on Anger cameras, which use a single monolithic scintillator and pixelated photodetectors as represented in figure 1.8, since, for a given collimator geometry, they allow to reach the same spatial resolution of pixelated structures, but employing a simpler (non-pixelated) scintillator crystal and a lower number of photodetectors and thus of electronics readout channels [7].

Imaging systems are characterized by few differences with respect to spectroscopy systems, since typically the energy resolution requirements are relaxed and the focus is posed on the spatial resolution. To start with, the scintillator crystal thickness is usually quite different in the two cases, since in medical imaging the energy of the γ -rays involved in the process are lower than the high energies that need to be detected, for instance, in physics experiments and thus they can be efficiently absorbed with thinner

crystals. A thin crystal facilitate the interaction position reconstruction since the scintillation light is originated close to the photodetector, while a thicker one spreads the light among many photodetectors. This light diffusion is sought in spectroscopy systems since it helps to reduce the photodetector saturation effects at higher gamma energies. Moreover for imaging systems reflections of the scintillation light represent a critical issue during operation and should be avoided, as they make the task of reconstructing the emitter position harder, so the crystal is usually coated with absorbing materials; on the other hand, in spectroscopy the interest is in collecting all the scintillation light, so the crystal coating has to be reflective and wrapped with diffusive layers in order to minimize the light not reaching the photodetector.

As it will be illustrated in next chapters, INSERT project belongs to the category of medical imaging systems, so the task of the position of interaction reconstruction is facilitated because of the thinner crystal (101,2 mm x 51,6 mm for the Clinical module, with 8 mm thickness), while GAMMA project main focus is on the spectroscopy task so it is characterized by a much thicker scintillator crystal (3 inches diameter and 3 inches height) and the imaging task is harder. However, the requirements that need to be met in terms of spatial resolution are more relaxed in the case of GAMMA project compared to INSERT project (1 cm with respect to less than 1 mm).

1.1.4 Multimodal Medical Imaging Techniques

A widely spread distinction applied to diagnostic imaging modalities is based on the nature of the provided information. Therefore, structural (or, equivalently, anatomical) and functional imaging techniques can be identified. The SPECT and PET systems just described in section 1.1.3 belong to the the category of functional imaging techniques: they do not provide good spatial resolution capability but they show very high detection sensitivity. Indeed, they can detect physiological abnormalities or disturbed biochemical processes by localizing tracer concentration in the

picomolar or nanomolar range.

On the other hand, structural imaging techniques, such as Computerized Tomography (CT) and Magnetic Resonance Imaging (MRI) provide high-resolution anatomical information of tissues under investigation. CT produces medical images, characterized by great spatial resolution and strong contrasts between tissues of different densities, in short acquisition times, by measuring the attenuation of X rays performed by body structures. Moreover some contrast media can be employed to highlight structures of interest that, otherwise, would be difficultly distinguished from their surroundings. The main drawback of this imaging technique regards the employment of ionizing radiation.

On the other hand, MRI shows extremely good capabilities to discriminate soft tissues with high spatial resolution, even in absence of contrast agents, and without employing any ionizing radiation. Indeed, this imaging technique is able to excite hydrogen atoms of water molecules building biological tissues by means of a strong static magnetic field and radio-frequency pulses. Moreover; MRI has proved to be a highly versatile imaging technique, capable of producing a variety of chemical, physical and also functional data. Conversely, main disadvantages are represented by long acquisition times and limitation of application for patient with metallic implanted objects, such as pacemakers or prostheses.

In this context, it appears advantageous to merge images from different medical modalities in order to get a combination of anatomical and functional information. Indeed, their ensemble provides a more complete clinical framework that allows to better address pathology diagnosing and therapy outcome monitoring. Systems following this kind of approach are referenced as "multimodal techniques". In figure 1.9 on the next page is shown an example of combination of SPECT and MRI techniques.

A first way to perform this merging is by retrospective software registration; however this approach presents several challenges concerning registration of images that are hard to cope with. These ones are due to:

- changes in patient positioning with respect to the two separate imaging devices;

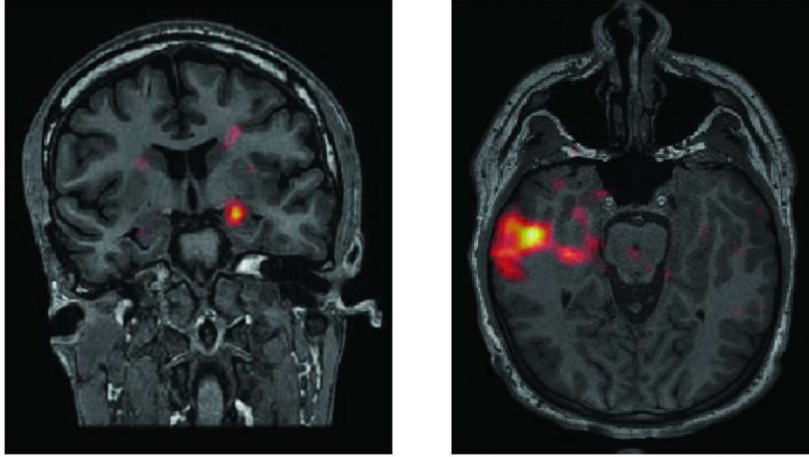


Figure 1.9: Example of co-registration of SPECT (colored) and MRI (gray) brain images to detect epileptic seizure onset zone. During a seizure, more blood flows to the area where the seizure comes from, and the region appears brighter.

- organ motions (e.g. respiratory movements);
- anatomical changes between the two scans, since that may be acquired days or even weeks apart.

In the early 2000s the first commercial implementations of devices allowing multimodality on a hardware basis were introduced. These were SPECT/CT and PET/CT scanners, in which nuclear medicine provided functional information by using radioactive tracers and γ -photon detectors, whereas CT was employed to image anatomical structures. The introduction of combination of modalities through dedicated hardware instruments proved to possess the ability to address scientific or clinical questions that would be impossible on separate systems. However, despite this significant advantage, multimodal hardware systems require a redesign with respect to the stand-alone solutions in order to match new compatibility and geometrical constraints necessary to achieve hardware combination.

Commercial available architectures allowing multimodal imaging on a hardware basis can be distinguished in three main categories [8]:

- *Separate system approach*: imaging scanners have separate gantries positioned in separate adjacent rooms: the patient is positioned and

immobilized on a dedicated imaging table which is moved from one system to the other. This approach permits less critical registration procedure since the acquisition of two modalities is performed over a limited time interval. Moreover, the two devices need no particular redesign since they are separated; therefore, performances regarding the respective images are preserved.

- *Sequential approach*: imaging scanners are spatially arranged in sequence and share the handling system that moves the patient from a device to the other in a faster, more accurate and more reliable way, with respect to separate system approach, despite still not allowing simultaneous acquisitions. Images of the two modalities can be registered applying a fixed coordinate transformation, established between imaging devices, in order to enhance the co-registration precision.
- *Integrated approach*: merges the two imaging modalities on a hardware basis, allowing simultaneous acquisition by multiple scanners. From a technical point of view, this approach is the most challenging one since it requires to adapt the design of the two systems, in order to avoid functional mutual interferences in operating conditions, and to design volumes dedicated to one or both the scanners, in order to match constraints imposed by the manoeuvrability of the patient into the gantry and by the geometry dependence of some imaging performance. Despite these difficulties, the simultaneous acquisition is of particular interest since it represents the only way to follow fast dynamic events with more than one modality, to reduce the overall time of an imaging session and to allow a high precision co-registration.

In figure 1.10 on the following page are schematized the sequential and the integrated scanner architectures.

At present time, one of the most active areas of research regarding multimodal systems is focused at the integration of PET or SPECT systems

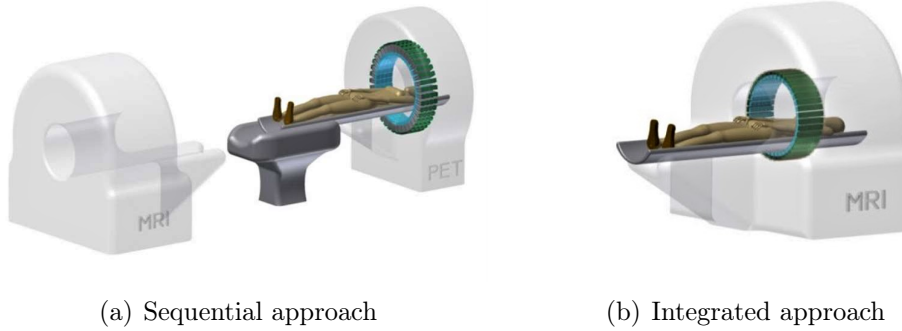


Figure 1.10: *Scanner architectures of two types of multimodal systems.*

with MRI. This latter is adopted, firstly, to provide anatomic information with superior soft-tissue contrast and by delivering an inferior radiation dose if compared to CT and, secondly, to combine molecular imaging, provided by PET/SPECT, with both anatomical and functional information achievable by MR techniques [9].

The main challenge concerning the realization of nuclear medicine scanners integrated with magnetic resonance is the necessity to cope with constrained technical issues, above all the mutual electromagnetic interference between different devices. Indeed, the SPECT or PET system must operate inside or in proximity of a high magnetic field environment: this precludes the use of conventional photomultiplier tube-based equipment and introduces the problem of interference affecting the signal produced by γ -ray detectors. Indeed, high power RF pulses generated by magnetic resonance devices can be easily picked up by SPECT or PET electronics and, conversely, these latter can radiate electromagnetic waves that can interfere with the MR signal. Finally, the MR system requires a high level of magnetic field uniformity, which is altered by foreign elements placed inside or around the magnet gantry since they introduce perturbations due to their magnetic permeability.

1.1.5 Silicon Photomultipliers

Photomultiplier Tubes (PMTs), due to their good performances in terms of energy and spatial resolution, were the conventional choice between indirect conversion detectors for both spectroscopy and imaging applications. However they are characterized by many drawbacks such as: sensitivity to magnetic fields, bulkiness, fragility and high operating voltages (up to 2kV), that make it difficult to create a compact low-power system [1].

With the only exception of linearity, which can however be improved by carefully choosing the detector parameters, solid state photodetectors overcome all of these problems and allow to reach both good energy resolution and good position sensitivity.

Among the different types of Silicon solid state detectors, Silicon Photomultipliers (SiPMs), which consist in a matrix of Single Photon Avalanche Diodes (SPADs) sharing a single output node, were selected as photodetectors for both INSERT and GAMMA projects.

Silicon Photomultipliers structure and working principle are illustrated below.

A SiPM is constituted by a parallel array of photon counting microcells (figure 1.11 on the next page).

Each microcell consists of a SPAD (also called Geiger Mode Avalanche Photodiodes) with an integrated quenching element. While Avalanche Photodiodes are biased below the breakdown voltage, so they operate with a linear amplification and their output current is proportional to the number of absorbed photons, SPADs are operated above the breakdown voltage and thus are characterized by a high internal gain (above 1×10^6): both electrons and holes contribute to the multiplication process and the current is self-sustained due to the feedback effect.

The peculiarity of SPADs consists in a bi-stable operating mode, meaning that the output signal does not depend on the number of impinging photons, but a self-sustaining current due to feedback is generated as response to the detection of just one photon. Furthermore, considering that the avalanche is self-sustaining, it has to be quenched in order to make

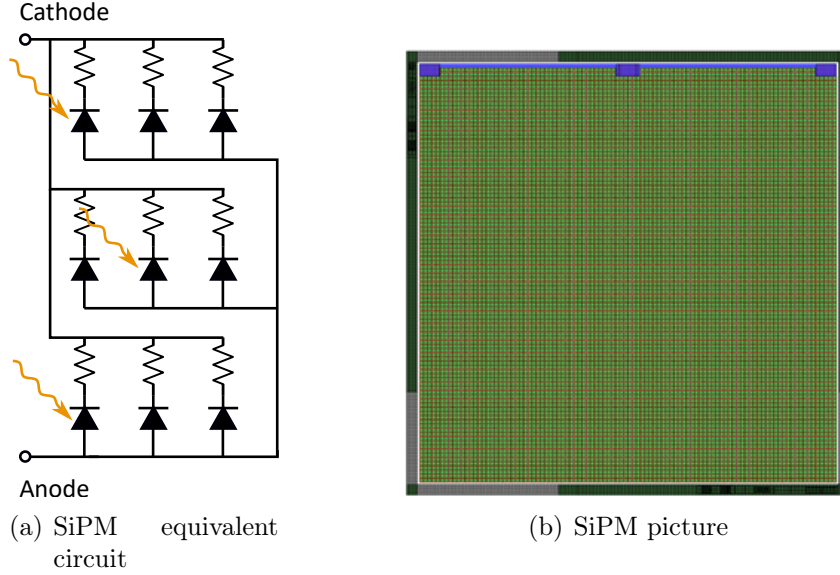


Figure 1.11: *SiPM equivalent circuit and picture of a 4 mm×4 mm SiPM from FBK with cell area of 40 μm×40 μm.*

the SPAD able to detect a new photon, usually by a passive quenching resistor that brings the bias voltage below the breakdown voltage. Due to its nature, a single SPAD is unsuitable for spectroscopy application, but an array of this devices can be used to detect different photons at a time, thus allowing multi-photon resolution in addition to single-photon capability, proper of this device. The operation cycle of a SPAD is reported in figure 1.12(b) on the facing page along with the equivalent circuit of a microcell.

In Silicon Photomultipliers, as a consequence of their design, each pixel operates digitally as a binary device, but the output signal varies linearly with the number of incident photons (at least up to a certain amount where saturation effect become visible), thus the SiPM acts as an analog detector.

These photodetectors have very fast timing, high gain ($> 1 \times 10^6$) at low-bias voltage (less than 50 V), which makes the electronic noise of the front-end negligible, an excellent single photoelectron resolution and they are rugged and insensitive to magnetic fields. They also feature an Excess

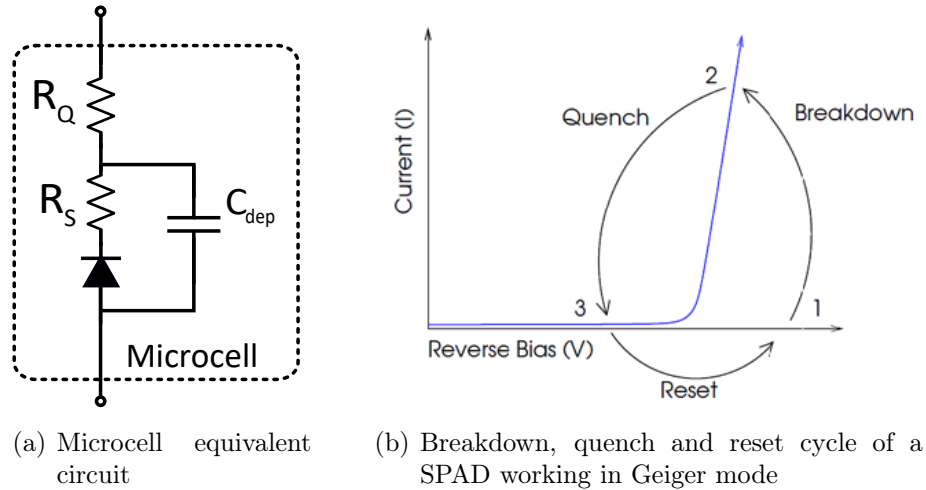


Figure 1.12: *SPAD equivalent circuit and operation cycle.*

Noise Factor (ENF) typically lower than 1,2 [10].

1.2 INSERT project

INSERT is a research project funded by the Seventh Framework Program of the European Commission and started on March 1st, 2013 [11]. Its acronym refers to the project aim of developing compact insertable SPECT system to be fit inside of commercial MR scanners for enhanced stratification of brain tumor and early assessment of treatment efficacy. In particular, the Project wants to address the need of a more powerful tool for the diagnosis and therapy of gliomas [12], a type of tumor that starts in the glial cells of the brain or spine and represents the 33% of the central nervous system tumors.

In terms of brain cancer treatments, the one producing the most relevant results is radiotherapy, which requires a precise localization and identification of the tumor and its environment. Therefore the possibility of a simultaneous multimodal acquisition allows to obtain multiple parameters to better define not only the position of the tumor in the patient-specific morphology but also its functional and biological behaviour. In figure 1.13

on the next page is shown a conceptual illustration of the INSERT system.

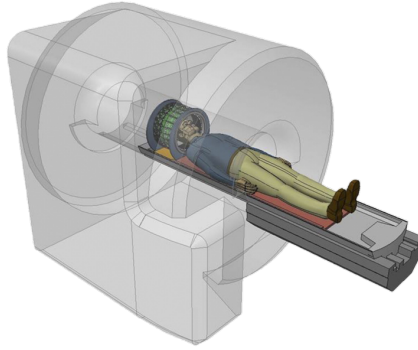


Figure 1.13: *Conceptual draw of clinical INSERT system. The SPECT ring (around the patient's head) is inserted in the MR scanner (gray).*

Although the design of an insertable SPECT rises many technical challenges, it represents the most flexible typology of hardware fusion with MRI. The system allows the simultaneous multimodal image acquisition with limited hardware cost, since the two systems are independent and only the SPECT system is appositely redesigned for MR compatibility (with the exception of the RF coils).

In INSERT Project framework, Politecnico di Milano group was responsible for the development of the γ -ray detection modules of the SPECT system, equipped with scintillator crystals, photodetectors (Silicon Photomultipliers (SiPMs) from Fondazione Bruno Kessler (FBK)), electronics for the readout of the SiPMs signal, cooling and other ancillary systems. The single detection module, which populates the final complete system, was designed to work in both the following devices:

- *Preclinical system:* (10 anger cameras - 36 channels each) for small animal imaging.
- *Clinical system:* (20 anger cameras - 72 channels each) for human head/neck imaging.

The target performance requirements that the final system must reach are: intrinsic spatial resolution (computed not considering the contribu-

tion of the collimator) of less than 1 mm FWHM ¹ and energy resolution of 12%, to allow the discrimination of ^{99m}Tc and ¹²³I energy peaks (respectively at 140 keV and 159 keV) in order to perform dual-tracer imaging.

1.2.1 Ring architecture

The aim of the INSERT system is to acquire 3D images of the distribution of radioactive probes in the whole human brain, without a prior knowledge of tumor location from other modalities. To achieve this goal a stationary ring architecture composed by gamma cameras (or, equivalently, gamma detection modules) is used, as illustrated in figure 1.14.

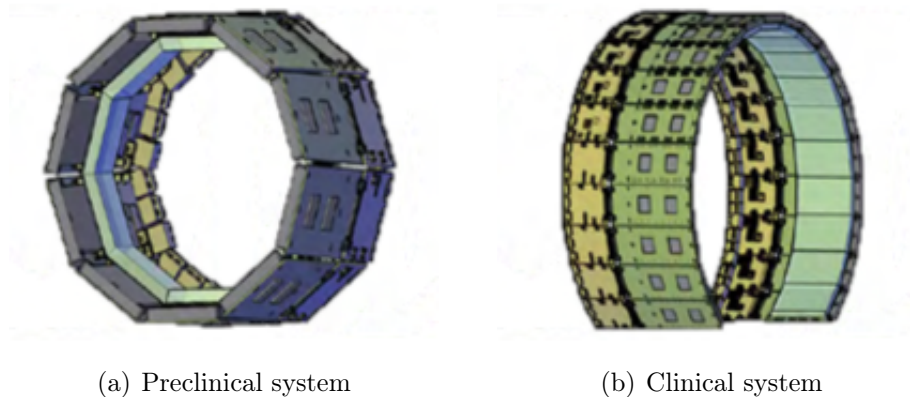


Figure 1.14: *INSERT stationary ring architecture, composed by gamma cameras.*

Gamma cameras acquire several projections on external planes differently oriented in space; subsequently these are combined by dedicated reconstruction algorithms, such as Filtered Back-Projection (FBP) or iterative methods (e.g. Ordered Subset Expectation Maximization (OSEM)). The result of this process is a set of tomographic slices, showing the radiomolecule distribution in different cross-sectional planes composing the 3D volume of the patient's area under examination.

¹Spatial resolution is frequently measured as the FWHM of the Point Spread Function (PSF), which represents the spatial response of the gamma imaging system to a point source.

Another technique to explore different projection planes in SPECT would be the *rotational approach*: the system is composed by a limited number of gamma cameras (typically from 1 to 4) that are positioned around the region to be imaged and are mechanically connected to a rotational engine which moves them around the region, in order to change the projection plane to be imaged. However, in the perspective of realizing SPECT-MR integrated systems, this second method cannot be employed and the stationary *ring approach* is the only applicable solution. Indeed the presence of a stationary magnetic field and the activation of gradient fields during MR acquisition make the engineerization of the movement required in the rotational approach extremely difficult.

In the interest of limiting weight, shielding was designed for a maximum emission energy of 210 keV, which may permit imaging of ^{177}Lu .

1.2.2 Gamma detection module

In INSERT Project, single detection modules are implemented, based on the Anger architecture, using compact indirect detectors.

Since the SPECT system must operate inside of a high magnetic field environment the use of the conventional Photomultiplier Tubes (PMTs) as photodetectors is precluded and Silicon Photomultipliers are adopted.

The conversion from high energy photons into carriers is provided by the optical coupling of a monolithic, inorganic scintillator with a 2D array of SiPMs. The two architectures of the module (Preclinical and Clinical) differ only in the dimension of the scintillator and, consequently, in the surface of the photodetection matrix.

A CsI(Tl) (Thallium doped Cesium Iodide) scintillation crystal was selected for the application: it has base dimensions of 50,6 mm x 51,6 mm for the Preclinical configuration and 101,2 mm x 51,6 mm for the Clinical one. Crystal thickness (8 mm) was chosen to optimize the trade-off between detection efficiency at 140 keV, which improves for thicker scintillators, and spatial intrinsic resolution, which behaves in the opposite way. The edges of the scintillator are slanted (as shown in figure 1.15 on

the next page) in order to be able to fix the module in the final SPECT architecture in a ring shape.

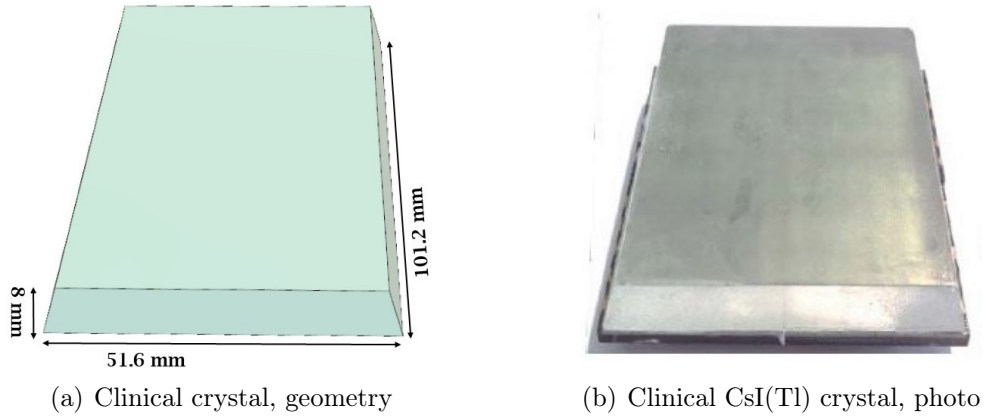


Figure 1.15: *Clinical INSERT crystal. Two edges of the scintillator are slanted of an angle $\alpha = 18^\circ$ in order to fix the detector modules in the final SPECT architecture in a ring shape.*

Characteristic parameters regarding CsI(Tl) crystal are reported in Table 1.2.

Parameter	Value for CsI(Tl)
Density [g/cm ³]	4.52
Light Yield [photons/keV]	65
Refractive Index	1.79
Decay Time [μ s] (RT)	0.68 (64%)
	3.34 (36%)
λ of max. emission [nm]	540

Table 1.2: CsI(Tl) parameters regarding interaction with gamma rays and optical behaviour [1].

In particular, the yield of the scintillator is of primary importance in this application since in low gamma energy detection (i.e. between 100 and 200 keV) a high gamma conversion coefficient is vital. Indeed, the number of collected photons influences the energy resolution and also helps improving spatial resolution, considering that the reconstruction al-

gorithms work better in presence of higher Signal to Noise Ratio (SNR) values.

In order to allow an even higher collection efficiency of light, the surface of the crystal is polished and a four-layer Teflon wrapping is employed. Indeed, above all the material for crystal coatings, Teflon layers exhibit one of the best value in terms of light reflectivity (around 94%) and, therefore help in reducing scintillation photon loss through crystal lateral faces.

For what regards the photodetector array, Clinical INSERT gamma module, is constituted by 8 tiles of SiPMs mounted on supporting PCBs (figure 1.16 reports the illustration of a single SiPM tile).

Each tile is constituted by 6x6 RGB-HD SiPMs (from FBK). The bias is directly carried to all the SiPMs cathodes through bridge bondings between neighbouring photodetectors. The output anodes of four neighbouring SiPMs are connected together to form a merged channel, therefore, each acquisition channel reads the current signal provided by the sum of four SiPMs. The active area of the virtual SiPM (obtained by the merging) is 8 mm x 8 mm. Technical characteristics of RGB-HD SiPMs are reported in table 1.3.

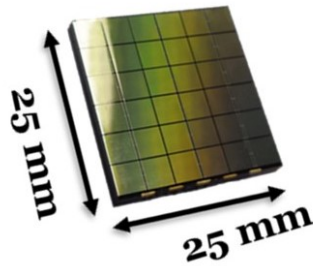


Figure 1.16: *Single SiPM tile, with an active area of 4 mm^2 , composed by 6x6 SiPMs.*

The photodetection matrix is optically coupled to the scintillator crystal through Meltmount, a transparent mounting medium similar to a resin. When heated up, the viscosity of the material decreases and the photodetectors can be glued to the crystal surface. Meltmount can have different refractive indexes corresponding to different mechanical properties. The

RGB-HD characteristics	
Microcell size	25 μm
SiPM active area	4 mm^2
Effective PDE	35%
DCR (0 °C)	$< 50 \frac{\text{kHz}}{\text{mm}^2}$
Breakdown voltage (0°C)	29 V

Table 1.3: Technical parameters of RGB-HD SiPMs.

target refractive index for the coupling material was calculated, in order to optically match the refractive indexes of CsI(Tl) ($n_{crystal} = 1.79$) and of the resin covering SiPMs ($n_{resin} = 1.51$), as the geometric mean of the two: $n_{target} = \sqrt{n_{crystal}n_{resin}}$. It was chosen a final value of $n = 1.539$, that is not the closest to n_{target} (still it is in between $n_{crystal}$ and n_{resin}) but have appropriate mechanical properties [13].

The output current signal of each SiPM is acquired and elaborated by the read-out electronics. When a gamma event is detected, all the SiPMs are read in parallel (simultaneously). The front-end electronics is implemented into a compact CMOS 36-channels ASIC (ANGUS [14]). For the clinical configuration, there are two ASICs mounted on the ASIC board, both used at the same time, that acquire 36 channels each, for a total of 72 channels.

The signals are then carried to a Data Acquisition (DAQ) board to be digitalized and transmitted to a calculator through optical fiber cables.

A thermoplastic, MR compatible, heat sink is placed in between the photodetection array and the ASIC board, in order to provide a stable moderate cooling for the reduction of the thermal noise of the SiPMs. In figure 1.17 the complete single detection module is shown.

Finally, the digitalized data are processed by Planar Event Reconstruction Algorithm (PERA), a standalone program, based on Maximum Likelihood Estimation (MLE), implementing a statistical reconstruction of the 2D position of interaction, developed by Politecnico di Milano [13].



Figure 1.17: (top) $CsI(Tl)$ crystal wrapped in Teflon (white). The SiPMs coupled to the crystal are hidden below. The ASIC board under the heat sink is connected to the DAQ board on the right. (bottom) Top view of the ASIC board (left) and DAQ board (right).

1.2.3 3D tomography

A dedicated custom software able to manage SPECT system calibration procedures involving all the gamma cameras and to perform both planar projection and tomographic reconstructions was developed by *Mediso, Kft., Hungary*, one of the Project partners companies.

The general schematic of the overall reconstruction chain is illustrated in figure 1.18 on the facing page. Each projection is reconstructed using the optical model of the respective camera (LRFs and LUTs) and the X,Y coordinates of the events of all the projections are used for the tomographic reconstruction. The introduction of DOI reconstruction opens the possibility to correct for the parallax error.

1.3 GAMMA project

GAMMA project, supported by Istituto Nazionale di Fisica Nucleare (INFN), focuses on the study of γ -spectra of radioactive nuclei created in particle accelerators as a result of high speed collisions [15]. The project involves Politecnico di Milano for the development of an innovative detec-

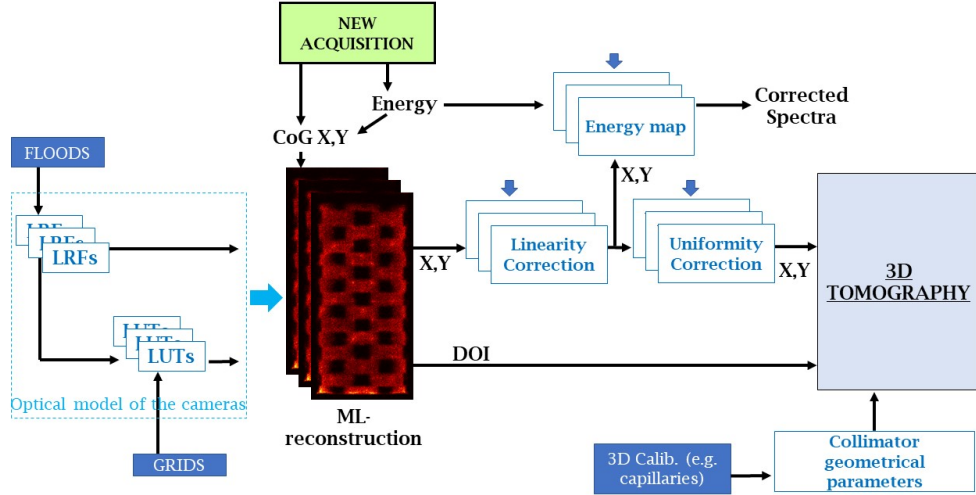


Figure 1.18: General schematic of the system for the 3D tomographic reconstruction.

tion module for nuclear physics and poses the challenge of achieving two objectives: reaching a state-of-the-art *energy resolution* of less than 3% FWHM at the ^{137}Cs emission peak (662 keV) and a *spatial resolution* of less than 1 cm in the reconstruction of the point of interaction. Silicon Photomultipliers (SiPMs) by Fondazione Bruno Kessler (FBK) are used as gamma detectors, coupled with a $\varnothing 3'' \times 3''$ $\text{LaBr}_3(\text{Ce}^{3+})$ scintillator crystal by Saint-Gobain.

The target energy resolution corresponds to the state of the art nowadays reached by Photomultiplier Tubes (PMTs). Nonetheless, due to the big advantages offered by solid state photodetectors as Silicon Photomultipliers, there is a strong interest in replacing PMTs with SiPMs. Besides the energy resolution requirement, GAMMA project also imposes a condition on the target spatial resolution of the detection module. This requirement comes from the necessity of compensating the relativistic Doppler effect which occurs when a radioactive emitter travels at relativistic velocities; as it will be explained later in section 1.3.1 on page 29 this effect, if not compensated, causes a degradation in the energy resolution [16].

The project requires the readout of large 3 inches diameter and 3 inches

height Cerium-doped Lanthanum Bromide ($\text{LaBr}_3(\text{Ce}^{3+})$) scintillator crystals, in order to maximize the absorption efficiency at the high expected energies, ranging from 100 keV to 20 MeV. The crystal is coupled with the Silicon Photomultipliers by means of optical grease, with the purpose of increasing the collection efficiency avoiding reflections between the crystal and photodetector surfaces. The readout electronics is composed by a dedicated ASIC [17, 18], and an FPGA-based Data Acquisition (DAQ) [19] capable of acquisition and data post-processing, both developed by Politecnico di Milano. A highly modular architecture of the system has been developed, in order to allow the readout also of smaller crystals, useful during the design to ensure and test the correct functionality of different block. A picture of the final instrument is proposed in figure 1.19 [20].



Figure 1.19: *Final instrument design, in fig.(a) the complete instrument is covered by the aluminum insulation cap while in fig.(b) the instrument is not closed and the SiPM matrix is visible.*

During this thesis work an architecture based on a 144-SiPM matrix, a single 8-channel ASIC and a simplified microcontroller-based DAQ, namely “LAILA² board”, has been used, but the final version of the in-

²Large dynamic range Acquisition Interface for Lanthanum bromide crystals

strument will be composed by the same matrix divided in 9 independent modules, each composed by 16 SiPMs readout by a dedicated 16-channel ASIC, immediately connected to a dedicated ADC through a printed circuit board including the linear regulators to supply the ASIC necessary voltages and power supply filters. The FPGA-based DAQ will control all the nine ADCs and will program the ASICs.

1.3.1 Doppler Effect Induced Peak Broadening

In everyday life we may experience that when a source of acoustic waves moves with respect to an observer, the wavelength perceived by that observer changes. Likewise, when a radioactive source moves at relativistic speeds, the emitted gamma photons experience an apparent energy shift. This energy shift induced by the Doppler effect leads to a widening in the energy spectrum [21] since different gamma photons which should contribute, with the same energy, to a single peak in the spectrum, end up having different energies, thus the measured resolution worsens, as represented in figure 1.20 on the next page.

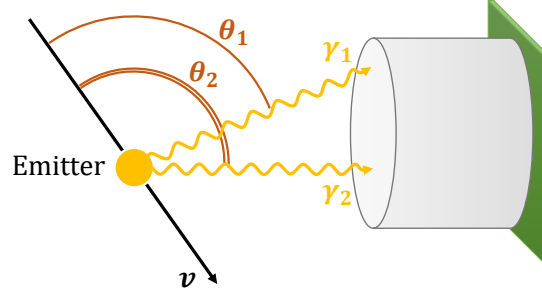
The effect of the Doppler shift can be analytically computed through the equation:

$$E_{\gamma} = E_{\gamma}^0 \cdot \frac{\sqrt{1 - \frac{v^2}{c^2}}}{1 - \frac{v}{c} \cos \theta} \quad (1.6)$$

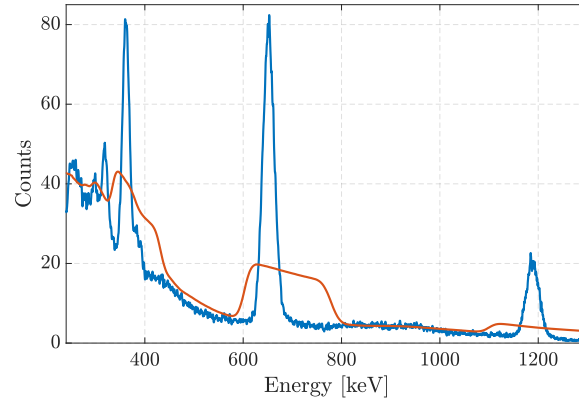
where θ is the angle between the emitter direction and the photon trajectory, v is the emitter velocity, c the speed of light constant and E_{γ}^0 the nominal gamma energy emitted by the source.

For instance, considering a $\varnothing 3'' \times 3''$ LaBr₃(Ce³⁺) scintillator crystal placed at 20 cm from the target, the covered angle θ is almost equal to 11°, and a 1 MeV γ -photon is detected with the resolution reported in table 1.4 on page 31 [21].

Despite that, it is possible to compensate the Doppler broadening if an estimate of the angle θ can be provided by the knowledge of the interaction point of the γ -ray inside the scintillator crystal. To this purpose, a precision of about 1 cm is required along with the emitter velocity (which is



(a) Scheme of a moving gamma emitter: if v is close enough to c , the two γ -photons will have a different apparent energy due to the two different incidence angles.



(b) Broadening of the photopeak

Figure 1.20: Due to Doppler effect, a broadening in the photopeaks is observed, reducing the energy resolution. In the energy spectrum in figure b) a uniform angular distribution of the γ -photons between $\pm 15^\circ$ and $v/c = 0.3$ was assumed for each of the input energies.

usually known) [16, 22]. Objective of this thesis work is the development of a reconstruction algorithm of the interaction position able to satisfy this requirement in terms of spatial resolution.

1.3.2 Lanthanum Bromide Scintillator Crystal

The detector performances targeted by GAMMA project require a high detection efficiency, high resolution and fast timing capabilities. In this framework the choice of the scintillator crystal becomes crucial.

v/c	Energy resolution
0	~ 25 keV
0.3	~ 70 keV
0.7	~ 230 keV

Table 1.4: Summary of the impact of Doppler effect on energy resolution for a 1 MeV photon: as v increases approaching c the energy resolution worsens.

On the market are available different scintillator materials offering a wide range of performances and features to match specific applications. For nuclear physics applications, the best available crystals are the Cerium doped Lanthanum Bromide ($\text{LaBr}_3(\text{Ce}^{3+})$) and its Cerium - Strontium co-doped version ($\text{LaBr}_3(\text{Ce}^{3+} + \text{Sr}^{2+})$), as they offer the best results in terms of energy resolution, timing capability and linearity. The main parameters of interest in a scintillator crystal include:

- Peak emission wavelength λ_p : corresponding to the wavelength of the scintillation photons emitted by the crystal.
- Light yield: is the average number of photon emitted for each keV of impinging radiation. The larger the yield, the larger will be the optical emitted signal.
- Scintillation decay time: determines the scintillator response speed. A fast scintillator is desirable for timing applications, and to avoid pile-up phenomena.
- Scintillator density: a denser scintillator directly translate into an higher detection efficiency, due to a higher radiation stopping power for the same volume.
- Intrinsic resolution: this parameter accounts for the impact of the crystal non-uniformity limiting the maximum achievable resolution, as represented in figure 1.21 on the next page.

In table 1.5 on page 33 are reported the main characteristics of some inorganic scintillators crystals [23, 10], highlighting the superior perfor-

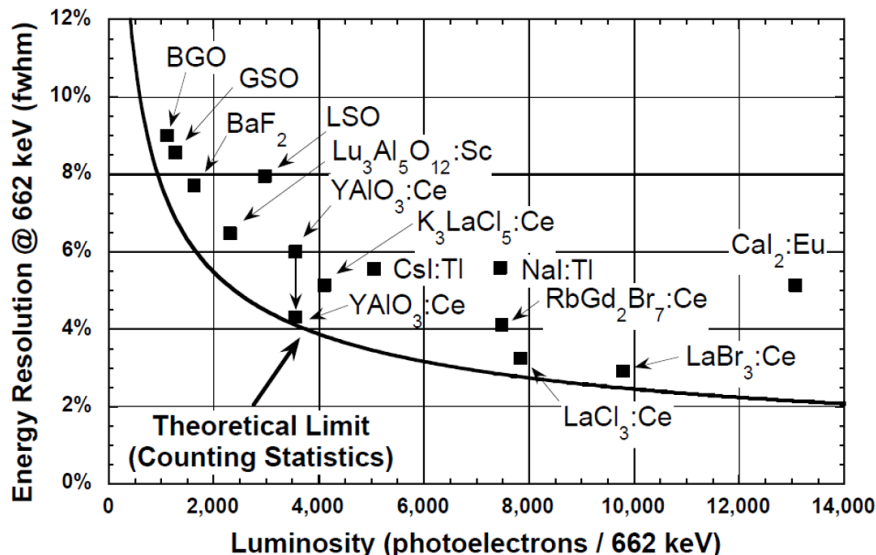


Figure 1.21: Resolution at 662 keV for different scintillators, compared to the theoretical resolution limit imposed by the counting statistics: the distance from the theoretical limit is the intrinsic contribution, assuming negligible the electronics noise. The $\text{LaBr}_3(\text{Ce}^{3+})$ offers a very low intrinsic contribution.

manances of $\text{LaBr}_3(\text{Ce}^{3+})$ and $\text{LaBr}_3(\text{Ce}^{3+}+\text{Sr}^{2+})$. For GAMMA project the scintillator crystals are provided by Saint-Gobain.

In addition to the main characteristics, Lanthanum Bromide also offers excellent output light stability in case of temperature variations, with only a 5% shift between -65°C and 140°C [24, 25], and even better for the co-doped version [26], while NaI(Tl) suffers from a light loss of 40% in the same range [27, Fig. 6]. The LaBr_3 also shows better radiation hardness with respect to NaI(Tl) and CsI(Tl), which is significant for space applications [28]. Moreover the crystal is mechanically robust, since the material is designed to sustain 1000 g shocks, 1000 g_{rms} random vibrations and 200°C temperature, in order to be used in oil well logging applications [27].

The main concern about the crystal is related to its highly hygroscopic behaviour, as humidity can deteriorate the crystal performances and the crystal structure. To prevent the inconvenient, the manufacturer encloses

Scintillator	Y [ph/keV]	τ [ns]	λ_p [nm]	n_{λ_p}	ρ [g/cm ³]	$R\%$
LaBr₃(Ce, Sr)	73	25	385	~ 2.0	5.08	2.2
LaBr₃(Ce)	63	16	380	~ 1.9	5.08	2.7
LaCl ₃ (Ce)	49	28	350	~ 1.9	3.85	3.3
CLLB	43	180,1080	420	~ 1.85	4.2	4.0
NaI(Tl)	38	250	415	1.85	3.67	7.0
CsI(Na)	41	630	420	1.84	4.51	6.1
CsI(Tl)	54	1000	550	1.79	4.51	5.2
LYSO	33	36	420	1.81	7.1	8.0
CdWO ₄	12 - 15	14000	475	~ 2.3	7.9	7.0
BGO	8 - 10	300	480	2.15	7.13	10
BaF ₂	1.8, 10	0.7 , 630	220, 310	~ 1.52	4.88	n/a

Table 1.5: Main characteristics of some inorganic scintillator crystals: light yield (Y), decay time of the light pulse (τ), wavelength of maximum emission (λ_p), refractive index at λ_p (n_{λ_p}), density (ρ) and the best resolution at 662 keV. The **highlighted parameters** indicate the best performances among scintillators.

the scintillator into a 0,5 mm thick aluminum housing, with a quartz window on the bottom for the output scintillation light as represented in fig. 1.22 on the next page. Inside the aluminum housing the crystal is wrapped with Teflon layers to better reflect the emitted light and limit light losses at the interface, improving the performances in terms of energy resolution.

Although providing good temperature stability, the lattice thermal expansion is anisotropic, and thus sensitive to temperature gradients. Saint-Gobain, manufacturer of the crystal, suggests a maximum gradient of 1 °C/inch and a maximum temporal variation of 8 °C/h [29, 30]. This effect has to be taken into account when designing the readout electronics and the cooling system.

The last matter to examine is the LaBr₃ spontaneous radioactivity, caused by the presence of ¹³⁸La and ²²⁷Ac isotopes. In order to address the internal radioactivity of the crystal, a spectrum acquisition can be run without any sources in low background conditions. The obtained spectrum of LaBr₃(Ce³⁺) is represented in 1.23 on page 35.

The spectrum region up to about 1,5 MeV is caused by the Lanthanum

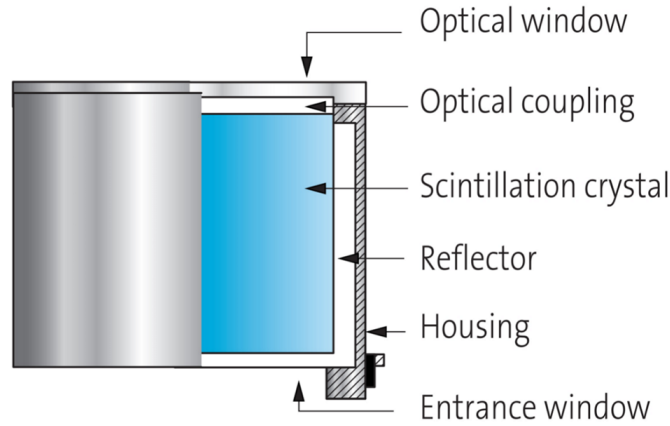


Figure 1.22: *Scintillator crystal cross-section, highlighting the aluminum housing in which the crystal is provided.*

decay into the excited state of ^{138}Ce (34.8% probability) and ^{138}Ba (65.2% probability); the first has an associated β -continuum that extends up to 258 keV and a γ -ray of 788,7 keV from the de-excitation of ^{138}Ce with a shifted β -continuum between 788,7 keV and about 1047 keV, the second instead emits a 1435,8 keV γ -ray, which sums with the ^{138}Ba X-rays giving rise to a peak in the 1470 keV region, [31]. There is also a contribution due to ^{40}K contaminants emitting a 1460 keV γ -ray [32]. The spectral structure above 1,5 MeV is related to the α -decay of Actinium contaminants, but its contribution has been reduced in crystal of recent production, due to improvements in the manufacturing process [33]. Except from spectroscopy investigations on energies corresponding to 1,4 MeV and 2,6 MeV, the internal activity of the crystal does not represent an issue and these peaks can be conveniently used for calibration.

Recently Saint-Gobain started to commercialize and improved version of $\text{LaBr}_3(\text{Ce}^{3+})$, called Enhanced Lanthanum Bromide, consisting in a Sr^{2+} co-doped version of the original crystal. The enhanced scintillator features a superior light yield together with a better linearity and an enhanced light yield temperature stability; the only worsening consists in a longer decay time (all values are reported in table 1.5 on the previous page). The most interesting property is the improved linearity at low en-

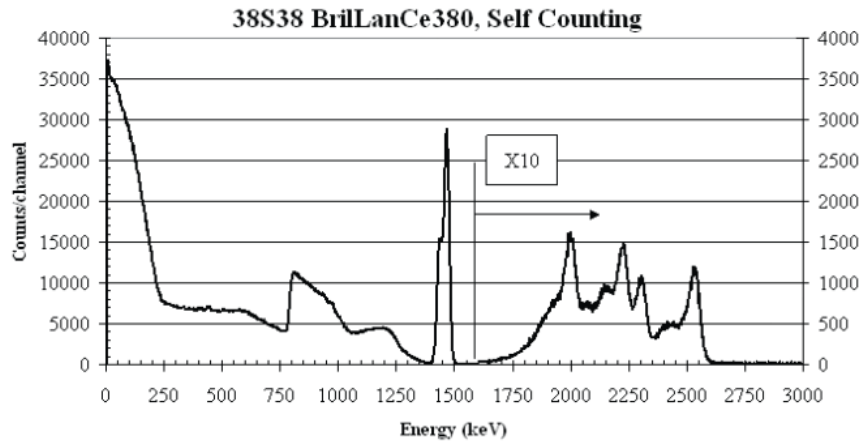


Figure 1.23: *Internal radioactivity spectrum of the $\text{LaBr}_3(\text{Ce}^{3+})$ crystal.*

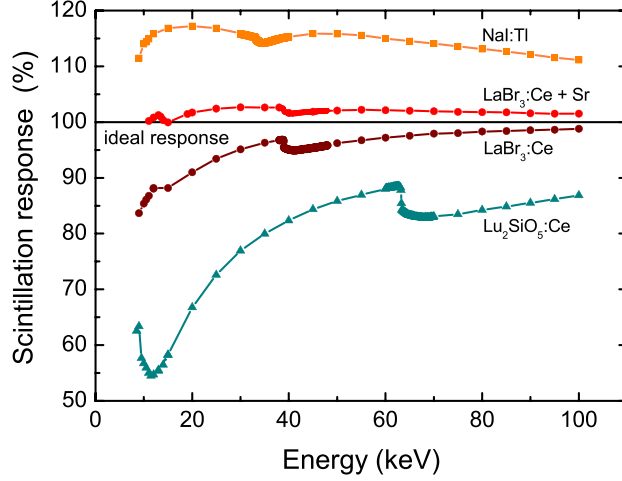
ergies (figure 1.24 on the following page) [34], considering that it allows to achieve better energy resolutions and provides the possibility to precisely calibrate the system. Characterization and measurements has been initially performed with the Cerium-doped version which has then been superseded by the co-doped one in all the applications due to its improved performances.

1.3.3 GAMMA-Project Silicon Photodetectors

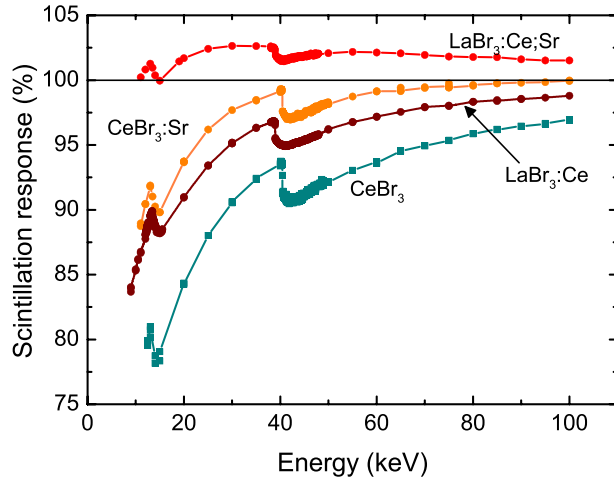
Photomultiplier Tubes allow to achieve good performances in terms of energy resolution in γ -ray spectroscopy, however they need high voltages to be operated and are bulky, fragile and sensitive to magnetic fields. Concerning the GAMMA project, the intense light pulse of LaBr_3 can cause problems in terms of photomultiplier linearity, particularly for high energy γ -rays [35]. Moreover the need of position reconstruction forces the use of Position Sensitive Photomultiplier Tube (PSPMT), whose performance in terms of energy resolution are poorer than spectroscopic grade PMTs.

For these reasons Photomultiplier Tubes should be replaced by solid state photodetectors, which allow to overcome all of these problems and reach both good energy resolution and good position sensitivity.

There are several types of Silicon solid state detectors: PIN Photodi-



(a)



(b)

Figure 1.24: Comparison of light yield linearity of various crystals at low energies: all curves are normalized to 100% at 662 keV energy.

ode, Silicon Drift Detectors (SDDs), Avalanche Photodiodes (APDs) and Single Photon Avalanche Diodes (SPADs). Among these, Silicon Photomultipliers (SiPMs) were selected as photodetectors for Gamma project [36].

The choice of SiPMs over the other solid state detectors was made considering all the advantages that the technology offers with respect to the

other detectors. In particular the reduced area occupation, the low voltage operation, the low temperature sensitivity of SiPM gain, the moderate Photon Detection Efficiency and the high robustness represent important practical advantages, when compared to PMTs, APDs and SDDs [37, 9, 38].

Chapter 2

INSERT: Depth of Interaction Reconstruction

This chapter presents the algorithm implemented for the reconstruction of the third coordinate of interaction, or rather, Depth of Interaction (DOI) in the INSERT project. The first part characterizes the problem of DOI estimation with the aid of ANTS2 simulation software and describes the reconstruction method; the second one illustrates the results obtained on experimental measurements.

2.1 DOI: motivation and reconstruction method

2.1.1 Importance of DOI information

One of the most challenging tasks in monolithic scintillator-based Anger cameras is determining the Depth Of Interaction (DOI) for each detected gamma ray. It is intuitive that DOI estimation is of primary importance in PET detectors, since they rely on electronic collimation based on coincidence. However one could wonder why there is an interest in knowing the Z-coordinate of interaction in SPECT and, more specifically, in INSERT project where each gamma detection module contributes with a reconstruction of the position of interaction in a 2D plane. The answer is that the knowledge of the DOI can be exploited to reconstruct with higher

precision the direction from which the γ -photon has arrived, allowing for a correction of the image and therefore improving the tomographic reconstruction. This results in higher quality of reconstructed images.

Indeed in SPECT scanners adopting collimators different from the standard parallel-hole ones (such as pinhole collimators, which are generally used in clinical systems), not only perpendicular γ -rays are selected, but also tilted ones are allowed to go through.

The distribution of the gamma events absorbed inside a crystal follows the Lambert-Beer law, which can be written as:

$$N_{ev}(DOI) = N_{ev0} e^{-\lambda DOI} \quad (2.1)$$

where N_{ev} is the number of not yet absorbed gamma photons at a given DOI, N_{ev0} is the number of gamma photons entering the scintillator and λ is the attenuation coefficient [m^{-1}] of the crystal, dependent on the density of the scintillator and on its mass attenuation coefficient.

Considering that events can be absorbed, according to the Lambert-Beer law, at various DOIs, we have that, for oblique gamma rays, different DOIs correspond to different X,Y scintillation coordinates. This error in the X,Y plane due to the Z-coordinate of interaction is called parallax error (see figure 2.1(a) on the next page).

From the knowledge of the DOI of each absorbed gamma photon a correction can be applied to compensate the parallax error: even just distinguishing the events absorbed in the lower half of the crystal from the ones absorbed in the upper half, could significantly reduce the uncertainty in the determination of the X,Y coordinates of the scintillation point (figure 2.1(b) on the facing page).

In gamma cameras implementing very thin scintillators, DOI information is generally not required: this type of cameras can provide a high spatial resolution at the expense of the detection efficiency. INSERT CsI(Tl) crystal, instead, has a thickness of 8 mm, which is not small enough to be immune to this problem. Therefore INSERT system is affected by the parallax error since a Multi-mini Slit-Slat (MSS) collimator is used: in the

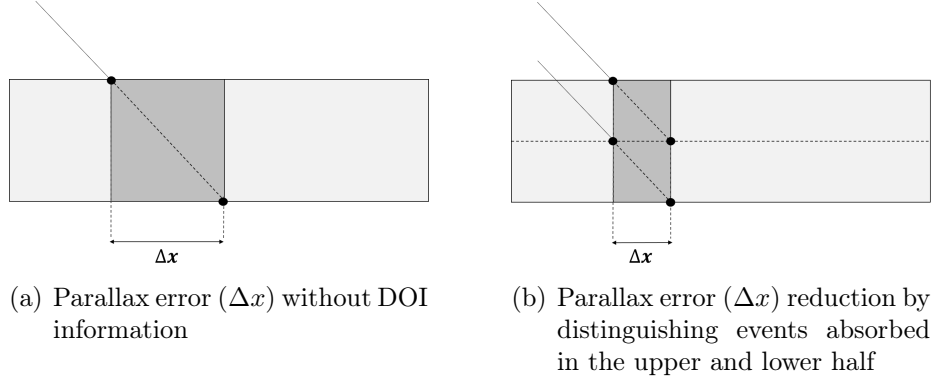


Figure 2.1: Parallax error (Δx) due to the fact that different DOIs correspond to different X scintillation coordinates. The uncertainty in the detection point is represented by the shaded area.

axial direction the slats provide a collimation similar to that of a parallel-hole collimator, but in the transaxial direction the mini-slits collimation resembles the pinhole one, as illustrated in figure 2.2 [39].

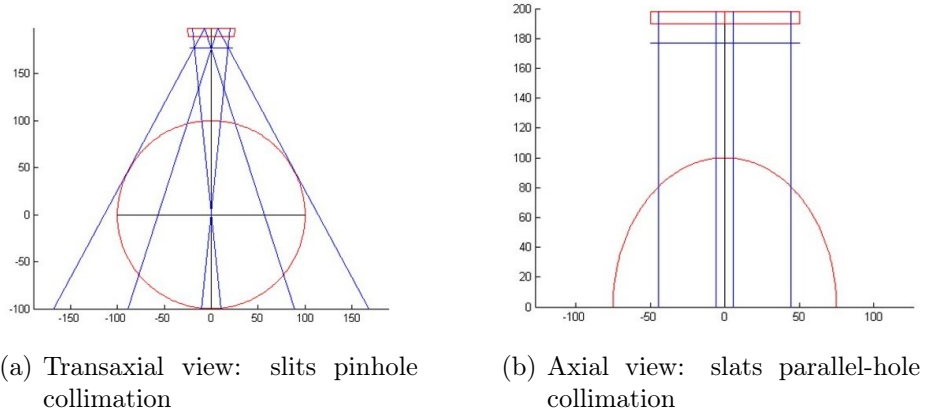


Figure 2.2: Projection of the Multi-mini Slit-Slat (MSS) collimator apertures FOV.

For this reason one of the objectives of this thesis work was to develop, starting from a previous work carried out at Radiation Detectors and Low-Noise Electronics Laboratory [40], a DOI classification algorithm for INSERT system.

2.1.2 DOI reconstruction method

DOI groups setting

The aim of this method is to assign every single absorbed γ -photon to a DOI group. Indeed, prior to the application of the reconstruction method, the crystal thickness is divided into a defined number of slabs (DOI groups). Each group corresponds to a different DOI range and ideally gathers events that share similar Z absorption coordinates.

Considering the thickness of CsI(Tl) INSERT crystal, a two clusters subdivision could be enough. However, a four-group classification still provided good results on simulations; therefore, the method was tested on experimental measurements for a division into four DOI groups. The employed DOI subdivision is schematically illustrated in figure 2.3.

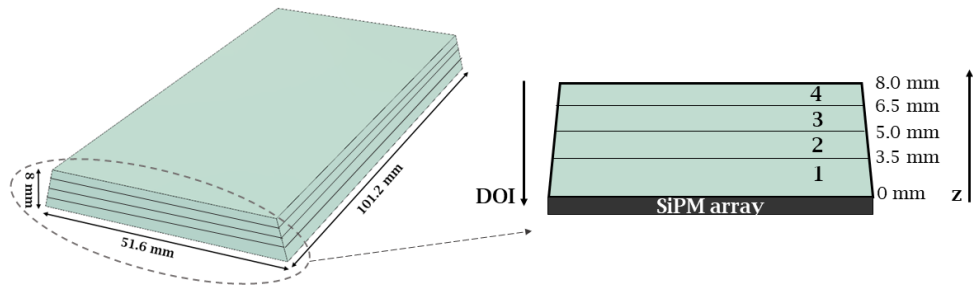


Figure 2.3: Division of clinical INSERT CsI(Tl) crystal into four DOI groups. The Z coordinates that identify the limits of the groups are reported on the right.

In principle, the Z values that separate different clusters should be chosen in order to equalize, as much as possible, the range in millimeters covered by each group; in this way the crystal is subdivided in DOI groups of equal range. However, for events absorbed close to the sensitive 2D photodetector array, a saturation of the SiPMs signal shows up, so it was decided to define the first group (DOI group 1) bigger with respect to the others (3,5 mm instead of 1,5 mm).

This saturation effect can be explained considering that, after the absorption of a γ -photon, the generated scintillation light is seen by the photodetectors through a solid angle, as shown in figure 2.4. The lower is

the Z coordinate of the absorption event the smaller is the area covered by the solid angle and the higher is the amount of photons absorbed by the photodetectors placed immediately below the scintillation event.

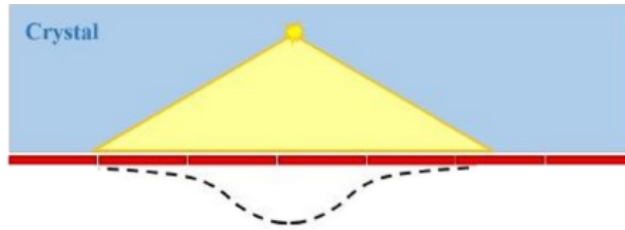


Figure 2.4: *Light distribution for a generic gamma event in a scintillator crystal.*

In INSERT single detection modules, the light distribution for gamma events whose Z coordinate is lower than 3,5 mm of crystal's thickness is so peaked that it almost completely covers only the SiPM directly below. This explains why there is a saturation of the photodetectors signal. Therefore it has no meaning to create multiple DOI groups below 3,5 mm as they could not be distinguished due to the signal saturation. The final selected ranges are reported in the table 2.1:

DOI group	Z range [mm]	DOI range [mm]
Group 1	0 - 3.5	4.5 - 8
Group 2	3.5 - 5	3 - 4.5
Group 3	5 - 6.5	1.5 - 3
Group 4	6.5 - 8	0 - 1.5

Table 2.1: *Range [mm] covered by the DOI groups. The origin of the DOI-axis is at the top of the crystal, while for the Z-axis is at the bottom (fig. 2.3).*

Once the number of groups and relative range covered are set, the actual method can be used: it is constituted by a preliminary calibration phase and by a second phase where each event is assigned to a DOI group.

Calibration phase

The calibration phase is needed to generate the Lookup Tables (LUTs) that will be used, in the second phase, for the DOI assignment. Each LUT stores, for every X,Y position, the response of the camera, on the basis of the signals acquired by the photodetectors, for all the DOI groups.

The sampled X,Y positions should cover the entire Useful Field Of View (UFOV) of the camera, defined as the portion where events are reconstructed without showing particular non-linear effects.

This kind of calibration is often performed through a scan of the crystal with a collimated beam source orthogonal to the crystal surface [41]. The problem of this kind of characterization of the detector response is that it can be very time consuming, as the beam must be moved to cover a great number of spots. Moreover, the control of the beam position requires a complex mechanical set-up, that is not feasible for a clinical SPECT.

If, instead, the calibration is performed by using a grid collimator with holes corresponding to determined X,Y positions, it is enough to execute a one-time measurement for every gamma camera. A dilution of ^{99m}Tc with high activity, filling a container that covers the whole FOV of the camera, can provide a high number of scintillation events for each hole in a short time. Then, the extension to spatial positions not covered by the holes of the collimator can be performed by fitting the DOI LUTs values with a smooth 2D function.

The calibration procedure can be performed only one time before the other measurements, if the operating conditions remain stable throughout the whole acquisition session. Every spot is calibrated independently from the others.

A possible disposition of the acquisition spots with respect to the detection plane is shown in figure 2.5 on the next page.

DOI assignment phase

After the generation of the LUTs, to classify the DOIs of a new measurement, two operations must be executed:

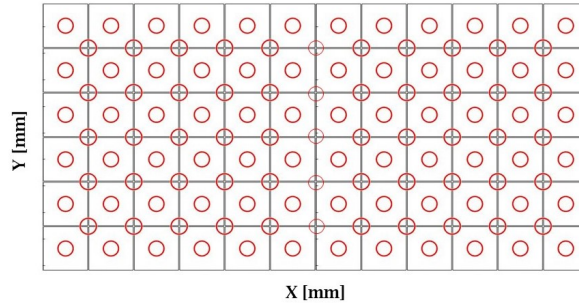


Figure 2.5: *The black grid represents the configuration of the clinical INSERT array of SiPMs. The spots (red) are centered on two different types of positions, SiPMs centers and SiPMs corners: they present the highest difference in the distribution of the acquired signals.*

- the X and Y coordinates of all the events are reconstructed by means of the 2D reconstruction method: Planar Event Reconstruction Algorithm (PERA) [13];
- for each event, the LUTs corresponding to the reconstructed (X,Y) position are used to assign the event to a specific DOI group, on the basis of a maximum likelihood estimation.

The classification method, and in particular the calibration procedure for the single spots, were firstly optimized through ANTS2 simulation software. Then, they were tested on experimental data.

2.2 Simulation results

2.2.1 ANTS2 Toolkit

For the optimization of the calibration procedure, it was employed ANTS2 toolkit (Anger camera type Neutron detector: Toolkit for Simulations) [42]. ANTS2 is an open source and multiplatform package, based on ROOT (CERN) and implemented in C++ programming language by Coimbra LIP (Laboratório de Instrumentação e Física Experimental de Partículas).

ANTS2 offers the possibility to model scintillator-based detectors and to simulate the processes of particle interaction, the subsequent production

and propagation of the scintillation light and, finally, the generation of the photodetectors signals.

All the program functionalities can be controlled either by an interactive GUI or by a JavaScript scripting tool.

The model of the clinical INSERT detection module, developed in a previous thesis work [40], was optimized for the current experimental set-up. In order to model the detector, ANTS2 requires the definition of both the geometrical and the physical properties of its composing materials. In particular, properties related to gamma particle interaction and optical ones have to be specified as accurately as possible to make simulations more realistic. The principal elements implemented in the clinical single gamma camera model are reported below, starting from the bottom of the structure to the top (and lateral sides):

- **SiPM 2D array:** 72 SiPMs (6x12), each one with an active area of 8.2 mm x 8.2 mm, an effective photon detection efficiency (PDE) of 0.35 (resulting from the coupling between the scintillator emission spectrum and the PDE vs wavelength response of the photodetectors) and Dark Count Rate (DCR) of $200 \frac{\text{kHz}}{\text{mm}^2}$ (pessimistic value). The SiPMs are covered by an optical interface with a refractive index equal to 1.515.
- **Meltmount:** coupling material between the SiPMs and the crystal, with a refractive index equal to 1.539 and a bulk absorption of $0,08 \text{ mm}^{-1}$.
- **CsI(Tl) Scintillator crystal:** the dimension of the lower base is 101.2 x 51.6 mm, while the upper base is 101.2 x 48.9 mm and the thickness 8 mm. The crystal has a density of $4,52 \frac{\text{g}}{\text{cm}^3}$, a photon yield of $65 \frac{\text{photons}}{\text{keV}}$ and an intrinsic energy resolution of 6 %. The refractive index is equal to 1.79. The scintillator was set as the only material able to interact with gamma rays (mass attenuation coefficient of $1,425 \frac{\text{cm}^2}{\text{g}}$, mean free path of 1,556 mm). The interaction properties of photoelectric and Compton effects for CsI(Tl) were directly loaded in ANTS2 from NIST XCOM web database [43].

- **Teflon wrapping:** the optical properties at the interface with Teflon were characterized by 6 % of photons absorption and 94 % of Lambertian scattering (diffusive reflection). For Teflon, the refractive index is set to 1.35 and the density to $2,2 \frac{\text{g}}{\text{cm}^3}$.

In figure 2.6 is reported the structure of the implemented model.

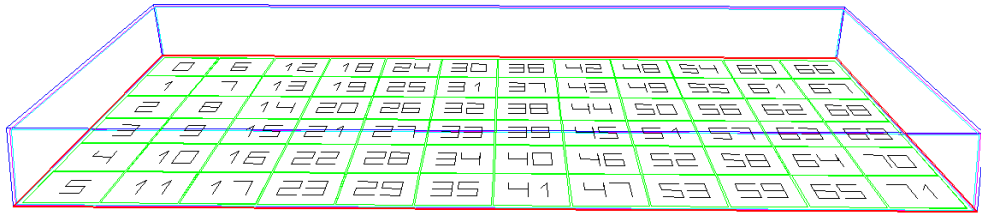


Figure 2.6: Model of clinical INSERT single detection module, developed through ANTS2 toolkit. The SiPM 2D array (green) lies at the bottom, the Melmount (red) is used to couple the SiPMs to the CsI(Tl) crystal (light blue). Teflon-wrapping (blue) is the most external layer.

For what regards the simulations, ANTS2 package allows to perform two types of modalities:

- **Photon source modality:** the process of gamma-ray interaction with materials is skipped and events are just emissions of optical photons at user-defined positions in the scintillator. The distribution of the number of photons emitted at each scintillation point can be selected among constant, normal, Poisson or custom distribution.
- **Particle source modality:** allows the simulation of gamma photons from a radioactive source and their interaction with the detection medium, followed by emission of scintillation photons. The shape and the position of the source, as well as the energy, can be configured. For this modality the distribution of events is in accordance with the real physics of gamma interaction: Lambert-Beer law is respected and the real Poisson's photon statistics stands.

For both modalities, the simulation output for each event is represented by the set of photodetector signals and by the true scintillation coordinates.

Simulated datasets can be exported in the form of text files to be processed by means of other software.

Indeed, not all the physical parameters and the dimensions of the different layers were accessible or directly measurable, therefore some of them were set according to reasonable realistic values. Moreover, the simulator expresses its output in terms of photoelectrons, while the real system in ADC bins. Nevertheless, simulations represented a useful tool for investigating the dependence of light distribution on the DOI.

2.2.2 Calibration phase

As explained in section 2.1.2 the number of DOI groups and the Z coordinates that separate different DOI groups must be defined in advance. Afterwards, the calibration procedure is performed, which requires the acquisition of gamma events at controlled positions. To implement this, a single-hole lead collimator was used. In figure 2.7 is represented the model of the collimator developed in ANTS2, using the same geometry of the one employed in the experimental measurements.

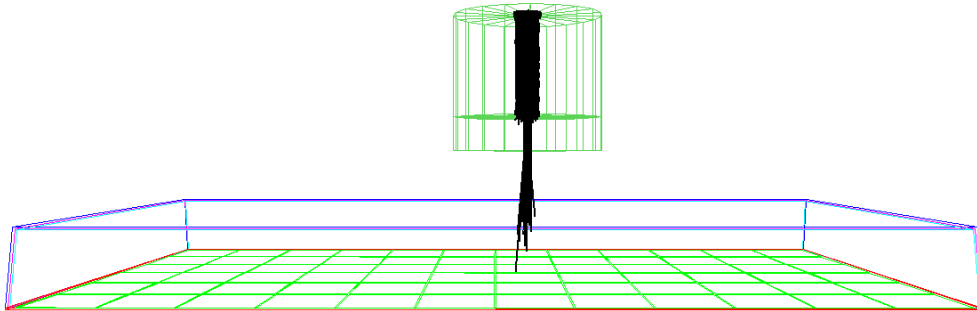


Figure 2.7: *The geometry of the collimator was build in accordance to the collimator used for experimental measurements. The upper hole diameter is equal to 3 mm, while the lower one is 1 mm. The collimator material is lead. In the experimental set-up the collimator is placed above the box containing the single clinical detection module. The distance between the collimator and the crystal represents the width of this box. The black lines represent the trajectories of few simulated gamma events.*

For every dataset, containing only events absorbed in a particular

(X,Y) position, the output of the calibration procedure corresponds to the respective LUT for each DOI group.

Since in ANST2 simulations the number of photoelectrons generated by each channel in correspondence of a scintillation event is considered a Poisson random variable, the obtained LUTs are expressed as:

$$DOI\ LUTs(X, Y) = \left\{ \mu_1^{(k)}(X, Y), \mu_2^{(k)}(X, Y), \dots, \mu_{72}^{(k)}(X, Y) \right\}_{k=1,2,\dots,N_{groups}} \quad (2.2)$$

where $\mu_j^{(k)}(X, Y)$ is the mean value of the signals (expressed in number of photoelectrons) acquired by the j-th channel for the k-th DOI group and depends on the scintillation point planar coordinates (X,Y). N_{groups} is the number of DOI groups.

Instead, the signals acquired by the electronic channels in the experimental setup are expressed in ADC bins and are considered normal random variables, therefore the DOI LUTs become:

$$DOI\ LUTs(X, Y) = \left\{ \left\{ \mu_j^{(k)}(X, Y), \sigma_j^{(k)}(X, Y) \right\}_{j=1,\dots,72} \right\}_{k=1,2,\dots,N_{groups}} \quad (2.3)$$

where $\mu_j^{(k)}(X, Y)$ and $\sigma_j^{(k)}(X, Y)$ are, respectively, the mean value and the standard deviation of the signals (expressed in ADC bins) acquired by the j-th channel for the k-th DOI group and they depend on the scintillation point planar coordinates (X,Y).

Data Preparation

For each absorbed gamma event the raw dataset contains the 72 SiPMs signals. Since the dataset is generated from a simulation, also the true coordinates of every scintillation point are provided. Before starting the calibration phase, raw data need to be elaborated through a couple of filtering actions.

To begin with, an energy filtering operation is performed: events whose energy is outside an energy window (e.g. 15 % width) centered around the photopeak position of the source are filtered out. The energy of the gamma events can be easily estimated by summing all the channels values (events per events).

Subsequently, since the acquisition necessary for LUTs generation is performed for different spots at the same time, by means of the grid collimator, events must be spatially divided into different datasets, each one corresponding to a hole position. To do this operation, the X and Y coordinates of every event are reconstructed, in the first place, through the PERA reconstruction method. Then, the division can be performed by means of a circular spatial filter centered around the X,Y coordinates of each hole.

Single Spot Calibration

Starting from the filtered dataset, corresponding to a single hole position (X,Y), the calibration procedure generates the LUTs(X,Y) necessary for the reconstruction of the depth of interaction in that position. This method requires as input the signals acquired by the SiPMs in response to the localized gamma irradiation, the desired number of DOI groups and their width. The calibration phase of each single spot can be divided in two steps:

- **step 1:** first subdivision of the events into DOI groups, based on Lambert-Beer law, to generate the starting LUTs⁰(X,Y).
- **step 2:** generation of the final LUTs(X,Y) through Maximum Likelihood classification of the events into DOI groups, based on the initial LUTs⁰(X,Y).

The first step of the calibration procedure performs, for each (X,Y) spot, an initial division of the events into N_{groups} subdatasets, each one corresponding to a DOI group. In order to obtain this starting division a parameter that has a high correlation with the DOI must be found.

By looking at the histogram of this signal, $N_{groups} - 1$ values should be found that are able to split the observations in the N_{groups} DOI groups, each one with an amount of events determined by Lambert-Beer law. The signal used for initializing this procedure will be referred to as initialization signal.

Initialization signal

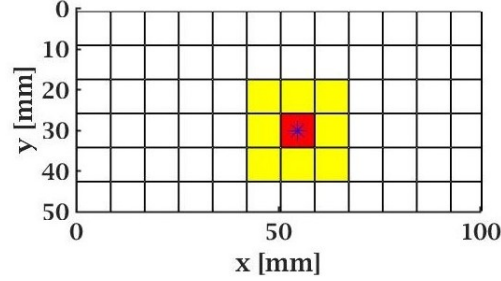
In order to identify the parameter having a strong dependence on the depth of interaction (for a given X,Y position), the optical behaviour of the gamma detector was analyzed through ANTS2 simulation software. The simulations were performed using the particle source modality: the radioactive source (emitting at 122 keV, corresponding to the energy of the gamma rays emitted by ^{57}Co) was collimated by a single-hole collimator (fig. 2.7) in order to fix the X,Y coordinates of the events. For each gamma event, the photodetectors signals and the true scintillation coordinates were recorded.

The simulations pointed out that the response to different depth of interactions, for the photodetectors close to the X,Y location of irradiation, depends strongly on the position of the collimator hole. As shown in figure 2.8 on the following page, two extreme cases can be distinguished:

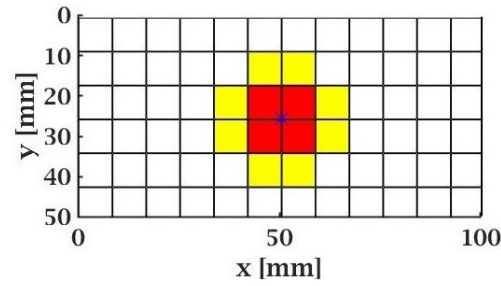
- case 1: scintillation position over the center of a SiPM (best case).
- case 2: scintillation position over the corner of four adjacent SiPMs (worst case).

Three different parameters was found to have good DOI dependence. For the i -th generic event these signals are:

- I_i : signal recorded by the SiPM which most frequently provides the maximum signal among all the SiPMs (in figure 2.8 is colored in red) [41].
- $\frac{N_i}{I_i}$: ratio between the sum of all SiPMs signals (called N) and I [44].



(a) Collimator hole placed above the center of a SiPM



(b) Collimator hole placed above the corner of four adjacent SiPMs

Figure 2.8: *SiPM detection matrix representation: in red are shown the SiPMs acquiring the highest signal I while in yellow are highlighted the SiPMs considered in the ring configuration. The collimator hole position is shown in blue.*

- μ_{ring_i} : mean value (or, equivalently, the sum) of the signals acquired by the ring of SiPMs (represented in yellow in figure 2.8) surrounding the one/ones under the hole of the collimator.

In the first case of collimator hole placed above the center of a SiPM, all of the three signals can be used as initialization signal, since they all show a high correlation with the DOI. In particular, a high DOI (which coincides with a gamma event absorbed close to the SiPM) corresponds to a high value of the I signal, since most of the produced scintillation photons are detected by the SiPM. Instead, as events are absorbed closer to the surface of the crystal, so for increasing Z ($Z = 8[mm] - DOI$), they generate less peaked light distributions that activate not only the central SiPM, but also the surrounding ones. Therefore, as Z increases, the central SiPM detect less and less scintillation photons and the signal I shows an

exponential decreasing trend, while $\frac{N}{I}$ a linear increasing behaviour [44]; μ_{ring} , as well as $\frac{N}{I}$, is higher for gamma events absorbed far from the SiPMs plane.

In the second case of collimator hole over the corners, instead, only μ_{ring} is able to provide a significant correlation with the depth of interaction. In this case, indeed, the highest signal (I) can happen with almost equal probabilities on one of the four SiPMs under the hole position, since the peak of the light distribution is in between them. Therefore I must be calculated considering the signals acquired by the four SiPMs, for example by taking the mean of the four signals; however, considering that the thickness of the crystal is 8 mm and every SiPM covers a planar area of 8 mm x 8 mm, the cluster made by the four SiPMs sees almost always the same amount of light photons, regardless of the depth of interaction of the event. Therefore, for the second case, only a combination of the signals acquired by the surrounding SiPMs (e.g. μ_{ring}) can be used as initialization signal.

In figure 2.9 on the next page are represented the scatterplots, obtained from ANTS2 simulation, showing the dependence of each of the three described parameters on the Z coordinate of absorption, both in the case of collimator hole position in the center of a SiPM and on the corner between SiPMs.

2.2.3 Results

In simulations, since it is provided the true Z coordinate of gamma absorption, it is possible to obtain, for a simulated spot irradiation, the histogram of the not yet absorbed gamma photons as a function of the true Z, as shown in figure 2.10 on page 55. The different colors represent the ideal DOI groups.

However the true Z information is not available in the experimental case, therefore, the initial classification must be performed through the initialization signal. For this reason, to follow the same method used for the experimental case, also in the simulation study the first subdivision of

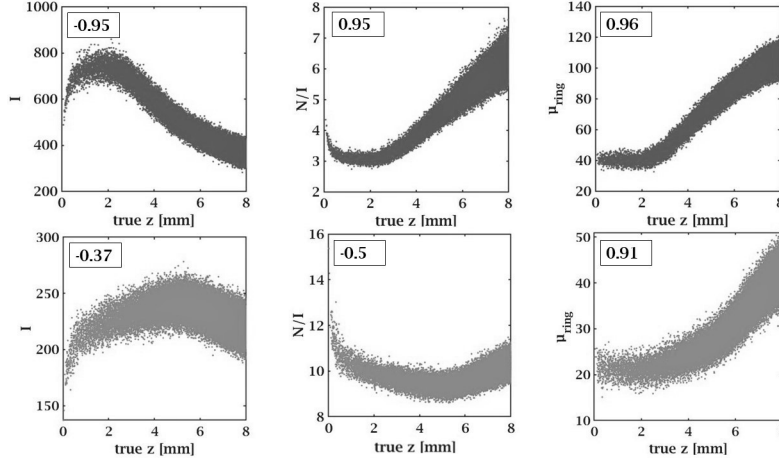


Figure 2.9: Scatterplots of the three analyzed signals (from left to right: I , $\frac{N}{I}$, μ_{ring}). The x-axis represents the true Z coordinate ($Z = 8[\text{mm}] - \text{DOI}$) recorded for each simulated gamma event. The top row shows the case of collimator hole position over the center of a SiPM. The second row, instead, represents the case of irradiation over the SiPMs corner. The correlation coefficient is shown in the upper-left corner of each plot.

the events has been performed exploiting the initialization signal.

In figure 2.11 on the next page the same histogram is plotted next to the crystal representation, in order to highlight the fraction of events that should fall inside each DOI range.

Initial Classification

Lambert-Beer law (see equation 2.1 on page 40) is used to calculate the cumulative probability that describes how likely a gamma event is absorbed within a given Z range. This information is used to extract the quantiles of the distribution of the initialization signal (e.g. $\frac{N}{I}$) that correspond to every DOI groups delimiter. These quantiles are the values of the initialization signal able to split the population of events in a way that the number of events falling inside each group is in accordance to Lambert-Beer law. Therefore, the groups delimiters expressed in [mm] are mapped into delimiters expressed in the unit of measure of the initialization signal, on the basis of the probability distribution described by this law. Then, the generic i-th event is classified into the group whose delim-

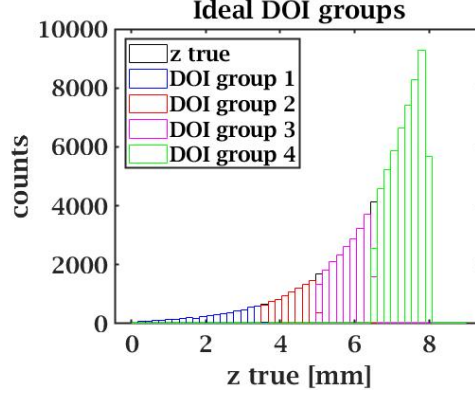


Figure 2.10: Histogram of the true Z coordinate of scintillation. The classification of events into DOI groups is based on the true Z coordinates themselves, therefore, the figure represents an ideal subdivision of events, possible only for simulations.

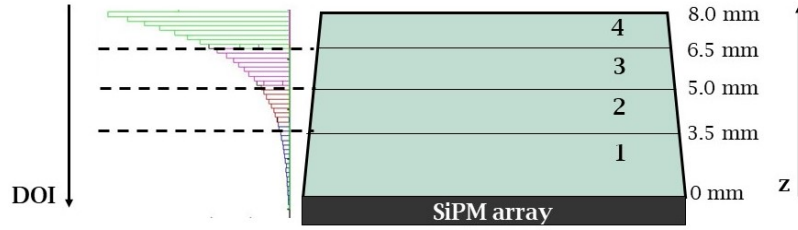


Figure 2.11: The exponential curve, obtained by simulated data, shows graphically the percentage of events that should fall inside of each DOI range, in accordance to the Lambert-Beer law.

iters contains $initialization_signal_i$. Figure 2.12 on the next page shows the histogram of the initialization signal $\frac{N}{T}$ and highlights the quantiles of the distribution.

From this first subdivision of events into the DOI groups, it is possible to calculate the starting LUTs⁰(X,Y).

As mentioned in section 2.2.2, in ANTS2 simulations, the photodetectors signal is expressed in number of photoelectrons and the k -th DOI group is statistically described by the set of mean values $\{\mu_1^{(k)}, \mu_2^{(k)}, \dots, \mu_{72}^{(k)}\}$. Therefore the initial Look-Up Tables can be expressed as:

$$LUTs^0(X, Y) = \left\{ \left\{ \mu_j^{(k)} \right\}_{j=1, \dots, 72} \right\}_{k=1, 2, \dots, 4} \quad (2.4)$$

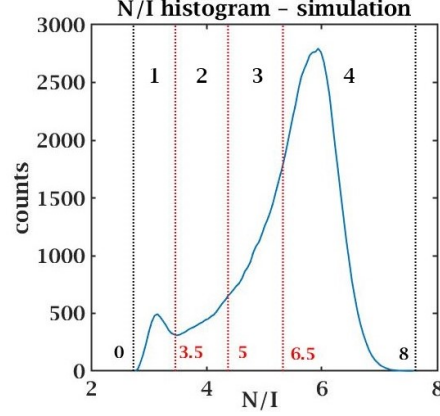


Figure 2.12: Histogram of $\frac{N}{I}$ initialization signal ($\frac{N}{I}$ is taken as reference). The vertical lines identifies the quantiles of the distribution that correspond to the Z values [mm] reported at the base of the vertical lines. $\frac{N}{I}$ is expressed in arbitrary units. An equivalent histogram can be obtained from experimental data.

where $\mu_j^{(k)}$ is the mean signal acquired by the j -th channel computed considering only the events classified into the k -th group.

Instead, in the experimental case, electronic channels output signals are considered independent, normally distributed variables, so the k -th group is described by a set of both mean values and standard deviations. Therefore the LUTs⁰ become:

$$LUTs^0(X, Y) = \left\{ \left\{ \mu_j^{(k)}, \sigma_j^{(k)} \right\}_{j=1, \dots, 72} \right\}_{k=1, 2, \dots, 4} \quad (2.5)$$

Maximum Likelihood Estimation Method

After computing the LUTs⁰, the events are classified again, this time into the final DOI groups, using the Maximum Likelihood Estimation (MLE) method: each event is assigned to the group for which the likelihood function is maximized.

Maximum Likelihood Estimation (MLE) is a technique to estimate the values of the unknown parameters of a model. The estimated values are the ones for which the process described by the model has the maximum probability to generate the observed data. In the case of the reconstruction

of a gamma event, the unknown parameters vector to be estimated is $\boldsymbol{\theta} = [X, Y, Z, N_{ph}]^T$, where X,Y,Z are the coordinates of absorption and N_{ph} is the total number of light photons (equivalent to the energy of the event). $\boldsymbol{v} = [v_1, v_2, \dots, v_N]$, instead, is the vector used to denote the observed sample, i.e. the response of the gamma camera to that scintillation event.

The observation vector $\boldsymbol{v} = [v_1, v_2, \dots, v_N]$ can be expressed both as the number of detected photons for each channel $\boldsymbol{v} = [n_1, n_2, \dots, n_N]$, or as the electronic signal acquired by each channel $\boldsymbol{v} = [s_1, s_2, \dots, s_N]$, where N is the number of channels (in the clinical configuration: $N=72$).

The process $\{V_1, V_2, \dots, V_N\}$ that has generated the observation \boldsymbol{v} is constituted by a set of N independent identically distributed discrete random variables V_j , where each one of these variables can be described by a known probability model M , which is a function of $\boldsymbol{\theta}$ ($V_j \sim M(\boldsymbol{\theta})$). The probability to observe the specific sample \boldsymbol{v} is given by the joint probability:

$$P(v_1, v_2, \dots, v_N | \boldsymbol{\theta}) = P((V_1 = v_1) \cap (V_2 = v_2) \cap \dots \cap (V_N = v_N)) \quad (2.6)$$

Since the variables V_j are independent, the joint probability becomes the product of the marginal probabilities:

$$P(v_1, v_2, \dots, v_N | \boldsymbol{\theta}) = \prod_{j=1}^N P(V_j = v_j) \quad (2.7)$$

and the likelihood (L) of the sample $\boldsymbol{v} = [v_1, v_2, \dots, v_N]$ is then given by the equation:

$$L(\boldsymbol{\theta} | v_1, v_2, \dots, v_N) = P(v_1, v_2, \dots, v_N | \boldsymbol{\theta}) \quad (2.8)$$

The estimator rule (or simply estimator) is a function that maps the data vector \boldsymbol{v} to the unknown parameter estimate $\hat{\boldsymbol{\theta}}(\boldsymbol{v})$. For ML-based reconstruction, the estimation rule consists in maximizing the likelihood function:

$$\hat{\boldsymbol{\theta}} = \arg \max_{\boldsymbol{\theta}} \{L(\boldsymbol{\theta} | \boldsymbol{v})\} \quad (2.9)$$

Thus, the ML estimate is the value of the unknown parameter for which

the observation is the most likely result to have occurred. Note that an equivalent frequently applied rule consists in maximizing the logarithm of the likelihood:

$$\hat{\boldsymbol{\theta}} = \arg \max_{\boldsymbol{\theta}} \{ \ln[L(\boldsymbol{\theta}|\mathbf{v})] \} \quad (2.10)$$

The ML estimation can be performed both in the case of signal expressed in photoelectrons or in electronic signals.

- In the first case, considering as assumption that the number N_{ph} of optical photons produced by local energy deposition processes (and consequently also the number of photoelectrons produced in each photodetector) is a Poisson random variable, it can be derived that the log-likelihood function to be maximized is:

$$\hat{\boldsymbol{\theta}} = \arg \max_{\boldsymbol{\theta}} \left\{ \sum_{j=1}^N (n_j \cdot \ln(\mu_j) - \mu_j) \right\} \quad (2.11)$$

- In the second case, considering that electronic noise affects signals in real systems, the signal acquired by the j -th channel (s_j) for a certain scintillation event is the realization of a random variable whose expected value is proportional to n_j by means of q_j , that is the average single photoelectron response of the j -th photodetector. If n_j is large enough (> 25 or more) and the single photoelectron distribution of the photodetector is reasonably symmetric, then, following the central limit theorem, the electronic signal of the generic j -th channel is approximately characterized by a Normal probability distribution, with mean $\lambda_j(\mathbf{r}, N_{ph})$ and standard deviation $\sigma_j(\mathbf{r}, N_{ph})$, being $\mathbf{r} = [X, Y, Z]^T$ [45]. Therefore it can be demonstrated that the maximization of the log-likelihood function in this case results in the following estimator [41][46]:

$$\hat{\boldsymbol{\theta}} = \arg \min_{\boldsymbol{\theta}} \left\{ \sum_{j=1}^N \left[\frac{(s_j - \lambda_j)^2}{2\sigma_j^2} + \ln \sigma_j \right] \right\} \quad (2.12)$$

Final Classification

For a single gamma event, the log-likelihood of belonging to the k-th DOI group is computed as:

$$\ln(L(DOI\ group_k | s_1, s_2, \dots, s_{72})) = \sum_{j=1}^{72} \left\{ n_j \ln(\mu_j^{(k)}) - \mu_j^{(k)} \right\} \quad (2.13)$$

in case of signal expressed in photoelectrons. Instead for electronic signals:

$$\ln(L(DOI\ group_k | s_1, s_2, \dots, s_{72})) = - \sum_{j=1}^{72} \left\{ \frac{(s_j - \mu_j^{(k)})^2}{2 \cdot (\sigma_j^{(k)})^2} + \ln(\sqrt{2\pi} \cdot \sigma_j^{(k)}) \right\} \quad (2.14)$$

where s_j is the signal acquired by the j-th channel for i-th generic event. Therefore, for each event, all the four log-likelihood are computed, then the DOI group which provides the maximum one is chosen.

After all the events have been sorted again, the LUTs(X,Y) are updated with the final $\{\mu_j^{(k)}\}_{j=1,\dots,72}$ and, additionally, $\{\sigma_j^{(k)}\}_{j=1,\dots,72}$ values.

In principle, it is possible to implement an iterative clustering procedure, performing several iterations of this last step of the calibration process and updating the LUTs with new values for every new iteration [41]. This should improve the classification of the events and further decrease the degree of overlapping between the groups. However, from simulations, it was proven that, after few iterations, the DOI range covered by each DOI group, changes significantly and in a way that depends on the X,Y position of the acquired spot. Indeed, it must be taken into account that the distribution of the events follows the Lambert-Beer law also inside each group. Therefore, even with an ideal classification, all the groups contain more events absorbed at lower DOIs than at higher ones. Consequently, the computation of the mean values for subsequent iterations can shift the DOI ranges towards the higher surface of the crystal, enlarging the first group and narrowing the last one. This phenomenon is particularly detrimental in the case of calibration spot position over the corner of four adjacent SiPMs. So, in summary, there is not the possibility to perform

several iterations with this specific method.

Therefore, the goodness of the calibration phase relies mainly on the initial subdivision of events into the DOI groups, based on Lambert-Beer law. Then, the single iteration slightly improves the subdivision of events, still preserving the initial ranges of the DOI groups.

The results of the calibration procedure applied to the data obtained from the simulation of the two extreme cases, irradiation spot over the center of a SiPM and over the middle point between four SiPMs, are shown in figures 2.13 and 2.14, respectively.

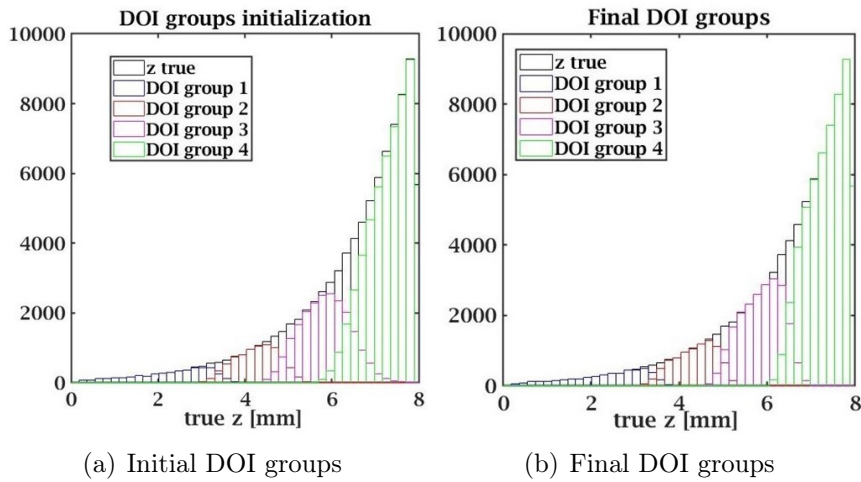


Figure 2.13: Histograms of true Z scintillation coordinates. Different DOI groups are shown in different colours. Simulated gamma events belong to a collimated spot laying over the center of a SiPM.

In tables 2.2 and 2.3, instead, the percentages of the correct classifications for each DOI group are reported. The information regarding the true Z coordinate of scintillation is used only to evaluate the calibration procedure.

It should be emphasized that events that were not classified in the correct way, were always attributed to the adjacent DOI group and never to more distant groups. For example, an event actually belonging to the DOI range identified by the Group 1, may have been classified in Group 2, but not in Group 3.

DOI group	1	2	3	4
Initialization	97%	87%	80,1%	93%
Final Classification	96,2%	89,8%	89%	96,7%

Table 2.2: Percentages of correct classification for each DOI group. The table reports the results corresponding to figure 2.13. The total percentage of correct classification is 94,2%.

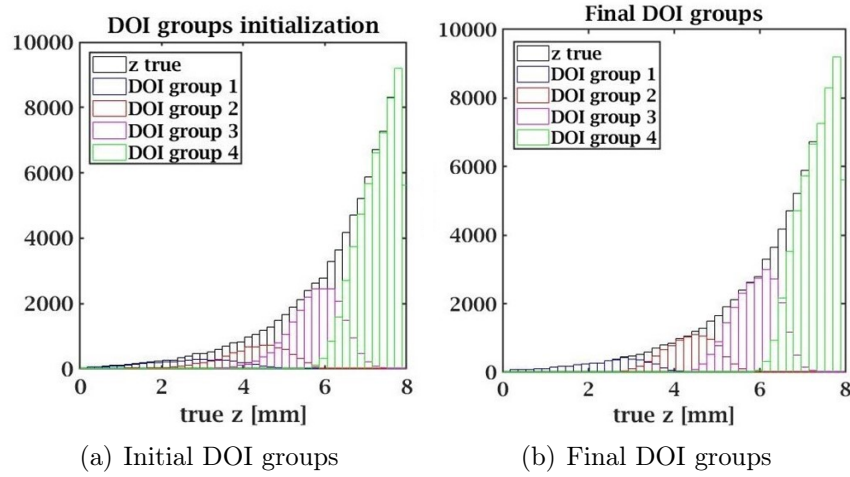


Figure 2.14: Histograms of true Z scintillation coordinates. Different DOI groups are shown in different colours. Simulated gamma events belong to a collimated spot laying over the crossing point among four SiPMs.

DOI group	1	2	3	4
Initialization	97%	87%	80,1%	93%
Final Classification	96,2%	89,8%	89%	96,7%

Table 2.3: Percentages of correct classification for each DOI group. The table reports the results corresponding to figure 2.14. The total percentage of correct classification is 90,6%.

Comparable results were obtained for different X,Y spot positions, leaving out the borders of the crystal, which will be analyzed separately.

2.3 Experimental results

2.3.1 Tilted beam and experimental set-up

To validate the algorithm on experimental measurements it is required the possibility to identify the depth of interaction in a independent way with respect to the classification method. Since in experimental measurements the true Z coordinate of interaction is not available, the chosen approach was to irradiate the crystal with a collimated tilted gamma beam. The beam was aligned along the x-axis of the sensitive matrix, with an angle of 45° with respect to the surface of the crystal: in this way, it is possible to directly associate the X position to a determined DOI, as schematically shown in figure 2.15. For example, a correct classification is obtained when the reconstructed X position lies within the range from 1,5 mm to 3 mm and the assigned DOI group is the number 3.

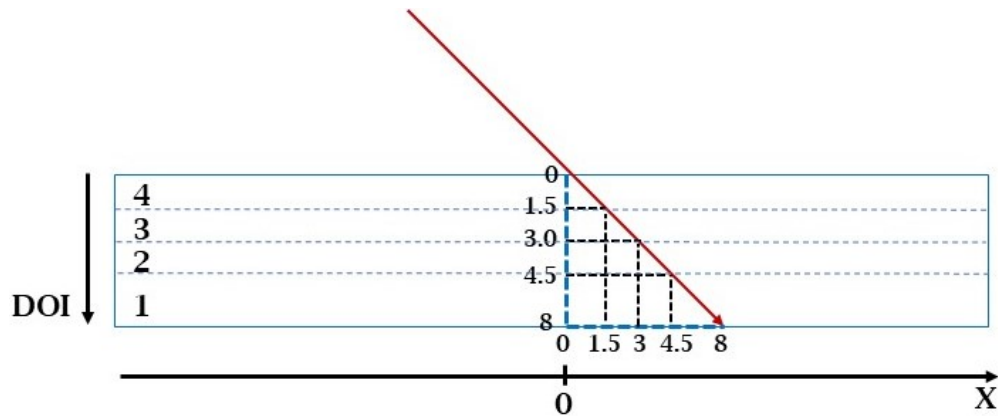


Figure 2.15: Schematic draw of the crystal (blue) and of the tilted irradiation (red). Since the gamma beam is tilted by 45° , the DOI ranges of the four groups are directly mapped into the respective X ranges.

Experimental Set-Up

To obtain the 45° tilted beam a ^{57}Co source was collimated by means of a set of collimators inserted inside a 3D-printed support. The tilted beam was aligned along the x-axis of the crystal.

For the calibration phase, instead, it is needed the set of LUTs(X,Y) for all the X coordinates scanned by the oblique beam. In order to get it, a vertical collimation of the source was performed for a total of four irradiation spots along the x-axis. In figure 2.16 are shown the lead collimators and the 3D-printed supports used.



Figure 2.16: (left) four collimators used for DOI experimental measurements. Three of them have a diameter of 3 mm. The other one has 1 mm-diameter. (centre) Collimators stacked to collimate the gamma irradiation vertically. This configuration is used for the irradiation of single spots, in order to build the DOI LUTs. (right) 3D-printed support to align the collimators at 45°.

In figure 2.17 on the following page, instead, is shown the experimental set-up used for this type of measurement. The set-up is composed by a single clinical INSERT gamma detection module.

2.3.2 Measurements and results

As anticipated in section 2.1.2, to reconstruct the DOI of a specific event, first the X,Y coordinates of absorption must be reconstructed, then, using MLE on the basis of the corresponding LUTs(X,Y), the event is assigned to a specific DOI group.

For the reconstruction in the X,Y plane, the PERA algorithm was used. This method working principle is based on the use of the Light Response Functions (LRFs) of the camera, which correspond to the average response of each individual photodetector as a function of the event position. The most straightforward way to obtain the LRFs of every SiPMs is based on experimental characterization of the crystal: an iterative procedure is applied on measured scintillation events produced by a flood field

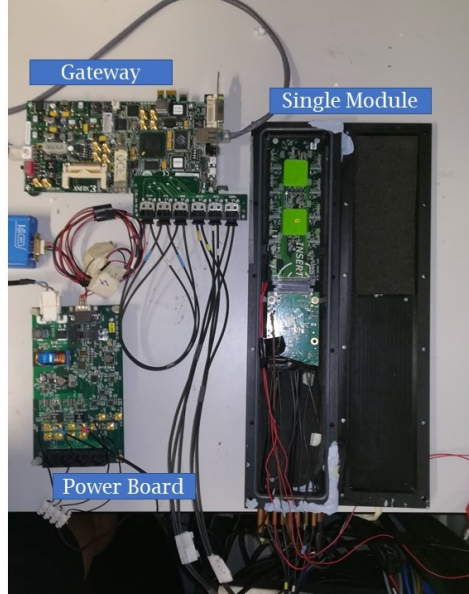


Figure 2.17: *Single module set-up used for DOI-related measurements. The crystal is below the ASIC board. The black box is used to isolate the inner environment, that must be filled with nitrogen for -10°C operations.*

irradiation (that is an irradiation from an uncollimated gamma source that uniformly irradiates the camera) [45][47][48].

After the LRFs training, the tilted irradiation was reconstructed by means of the statistical method based on the maximum likelihood. The planar reconstruction is shown in figure 2.18 on the next page. From the figure, it can be noticed that the elongated right part of the spot, corresponding to the γ events absorbed at high DOIs, has a lower density of events. This is explained by the Lambert-Beer law, according to which the number of absorbed γ -photons decreases exponentially with the DOI.

The image shows how, in the case of a tilted beam, the parallax error can affect the quality of the image reconstruction. An ideal system, indeed, would detect a normal single spot for gamma rays coming from the same direction, even in the case of tilted irradiation. However, with the addition of the DOI information, this error can be reduced.

To be able to assign each event of the oblique gamma ray to a DOI group, the discrete LUTs(X,Y) were calculated from a set of spots acquired

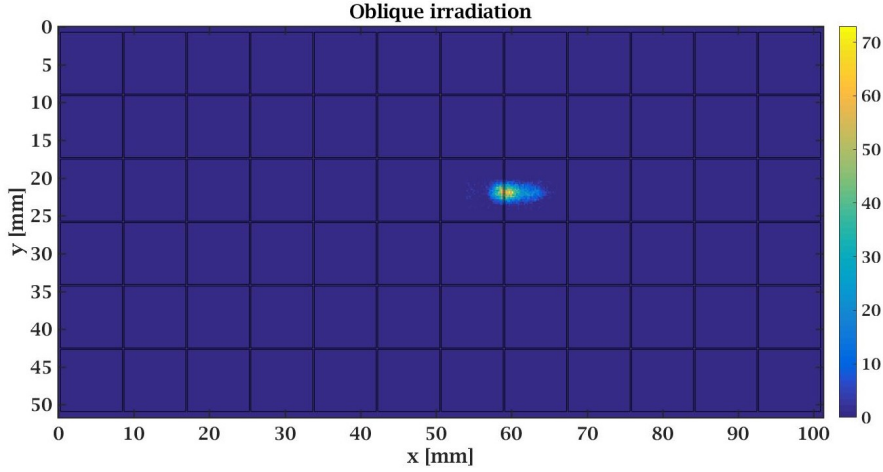


Figure 2.18: Planar ML-reconstruction of the tilted irradiation. The SiPMs borders are shown in black. The gamma beam enters the crystal directed at 45° towards the right. Most of the gamma events are absorbed in the first part of the crystal, while the spread on the right is related to events absorbed at a higher DOI.

through a vertical collimation of the source along the X,Y positions covered by the oblique irradiation. The planar reconstruction of the spots is shown in figure 2.19 on the following page.

To obtain the dataset for each single spot, first of all, the X,Y coordinates of all the events of the collimated irradiation, were reconstructed with the statistical method employing the LRFs previously trained; then a spatial filter was applied to select only the events within a given radius from the center of the spot. The filter was used to build a 'good' dataset for LUTs generation by discarding background events.

Afterwards, the DOI LUTs(X,Y) were fitted by means of a 1D smooth function ($f \sim f(X)$), since all the spots share the same Y coordinate. The fitted LUTs were used to reconstruct the depth of interaction of the gamma events of the oblique irradiation, using the method based on the maximum likelihood. The procedure is exactly the same as the one implemented in the last step of the single spot calibration, with only two differences. Firstly, the log-likelihood for every group is directly calculated from the final LUTs generated in the calibration phase. Secondly, the set of LUTs

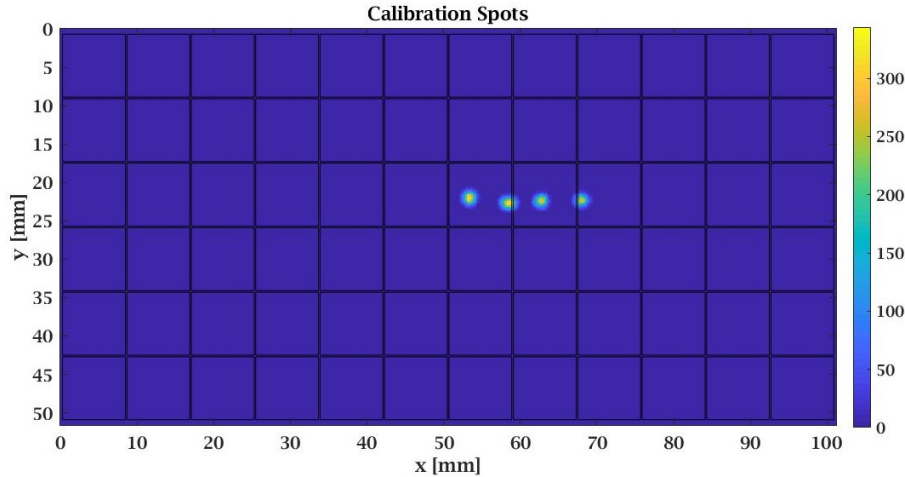


Figure 2.19: *Planar ML-reconstruction of the calibration spots. The spots were acquired and processed separately. They were put together only in the image. Since the collimator was moved by-hand from one spot to the other, the alignment is not perfect. Nevertheless, the displacement is compatible with the y-width of the reconstructed tilted irradiation.*

used, can differ from one event to the following one, since they can have different X,Y positions.

As can be seen in the planar images of both the oblique irradiation and the vertical calibration spots, the highest density of events is reached in the center of the spot, then the density decreases radially. Therefore, in order to map the DOI ranges to the X ranges and validate the DOI classification method for the events of the oblique irradiation, the origin of the x-axis was placed in the point of highest events density: all the events that in the figure 2.18 are on the left of this position were discarded, and only the ones on the right were used.

Figure 2.20 on the next page shows the four separate histograms, each one for a different DOI group, of the reconstructed X coordinate. Referring to figure 2.15 on page 62, the peak of each distribution is within the expected range, with the exception of the DOI group 1 (histogram on the right), whose peak was expected to be at a higher X value.

This is explained by the fact that, according to the Lambert-Beer law, the percentage of events absorbed within 8 mm of CsI(Tl) crystal for the

^{57}Co source (122 keV) is equal to 99.4%. When the beam is tilted by 45° , 8 mm along the diagonal direction corresponds to approximately 5.7 mm along the x-axis. Therefore, an almost negligible amount of gamma events is absorbed beyond this limit and the peak of the last histogram is shifted towards the left. Moreover this group is affected by the highest error of collimation, considering that it is relative to events being absorbed near the SiPMs array and that the degree of collimation of the source decreases as the distance from the collimator increases.

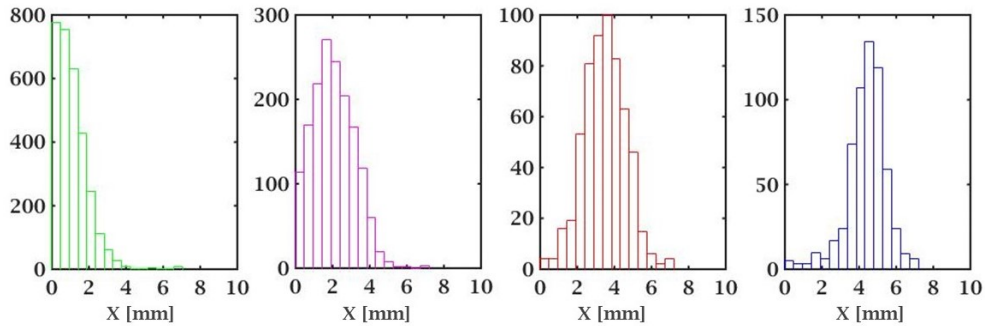


Figure 2.20: Histograms of the reconstructed X coordinate for every reconstructed DOI group. The one on the left is relative to DOI Group 4, the last one on the right to the Group 1. The different amount of events inside each groups is explained by Lambert-Beer law.

Instead, figure 2.21 on the next page shows the reconstructed tilted beam combining both the information on the X coordinate and on the DOI of the events. The same considerations of figure 2.20 still apply here: events classified in the Group 1 are affected by the highest error of geometrical collimation of the gamma beam. The number of counts is in accordance with the Lambert-Beer law: most of the events are absorbed near the crystal surface, then their amount decreases exponentially with the DOI.

The oblique irradiation was also simulated using ANTS2 package. Figure 2.22 on the following page shows the employed model of the scintillator crystal and of the collimators. It should be emphasized that the collimator is placed at a given distance from the crystal, since, in the experimental set-up, the crystal is kept inside a box (whose function is to dry the inner

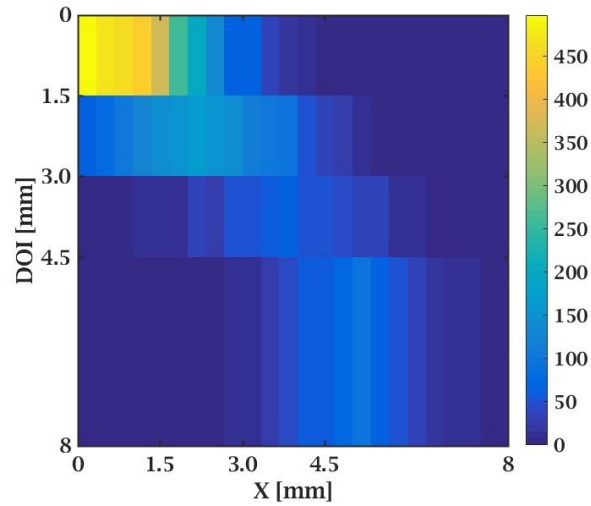


Figure 2.21: *2D histogram of the DOI reconstruction. The image represents the reconstruction on the plane identified by x and DOI axes of the tilted beam events.*

environment to set -10°C of temperature), making it impossible to position the collimator in contact with the scintillator. Moreover, the true coordinates of interactions are represented in figure, highlighting how a higher degree of collimation could provide a better estimation of the goodness of the classification method.

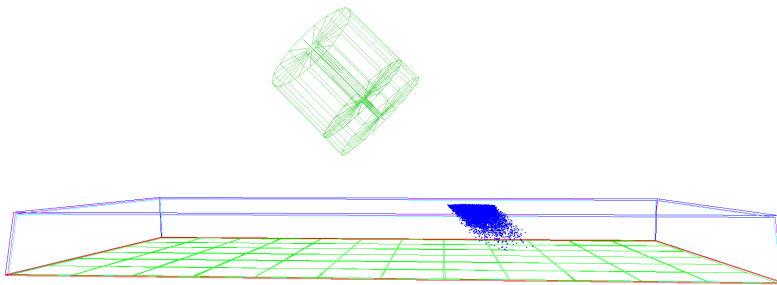


Figure 2.22: *ANTs2 model used for the oblique irradiation simulation. The true positions of interaction of the absorbed events are shown in blue.*

Backward shift correction

With the aim to further prove the DOI classification method, the information provided by the DOI reconstruction was exploited to improve the planar reconstruction of the oblique irradiation, already shown in figure 2.18.

Since the geometry of the collimator is known (i.e the direction of the oblique ray is known), to correct the image, it is possible to apply to each event a backward shift proportional to the classified DOI. In this way, supposing that the gamma events have been correctly classified inside the proper DOI groups, the elongated spot should be able to recover the original symmetric spot shape.

The backward shift to apply is peculiar to each DOI group. Since the events have been classified into discrete groups covering a given DOI range, the real continuous distribution along the DOI-axis is not provided by the classification. However, the theoretical distribution is supposed to follow Lambert-Beer law. Therefore, the mean DOI value for events assigned to the k -th group, is calculated considering the theoretical distribution, and not by the simple mean of the group delimiters. As a consequence, the mean of every group is closer to the upper delimiter of the group (the one closer to the surface of the crystal).

Therefore, events classified inside the k -th group are shifted back along the x -axis by an amount equal to the above-mentioned mean DOI value of the group (since the collimation is tilted by 45° degrees). The image resulting from this simple correction is shown in figure 2.23 on the next page.

As it can be seen from the figure, the shape of the spot is almost recovered, showing promising results for the classification method.

It should be pointed out that the aim of this correction was not to correct the parallax error, but only to further prove the reconstruction method in a visual way. Indeed, the real correction for the parallax error involves different geometric parameters and is not performed by a simple backward shift: the 3D reconstruction algorithm that, starting from the

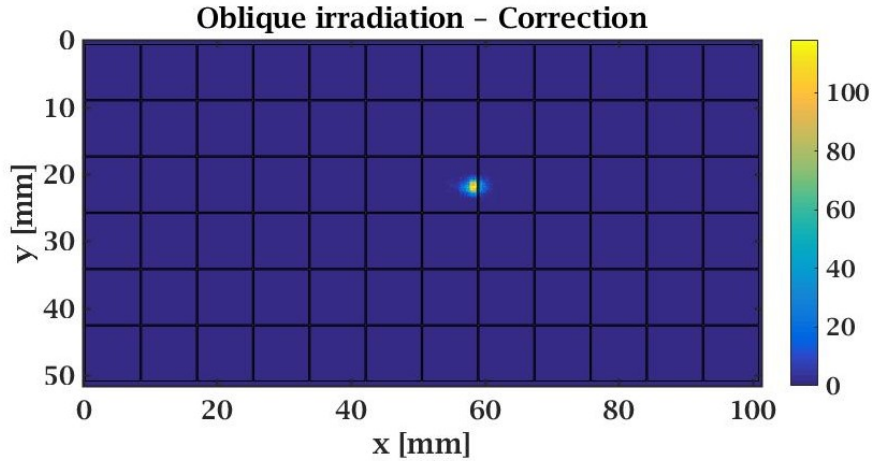


Figure 2.23: *Corrected planar reconstruction of the tilted irradiation, obtained using a simple correction method based on the knowledge of the DOI group of each event.*

X,Y coordinates of the gamma events of all the single projections, performs the tomographic image reconstruction, is fed with the information of the DOI of the events to correct for the parallax error.

Figure 2.24 on the facing page shows the comparison of the planar X,Y reconstruction of the tilted beam before and after the correction with the DOI information.

2.3.3 Crystal borders

Finally, it was addressed the ability of the DOI classification method in the reconstruction of events absorbed at the border of the crystal, outside the central region of the camera.

The analysis was carried out only through simulations, therefore further investigations will be necessary to check if the model of the detector, built with the simulation software, is able to represent the behaviour of the real camera for lateral scintillation positions. As mentioned before, the crystal is wrapped in Teflon, which has the optical properties of a diffuse reflector. Thus, at the borders, not only the distribution of light is particularly asymmetric, but also imperfections in the wrapping can

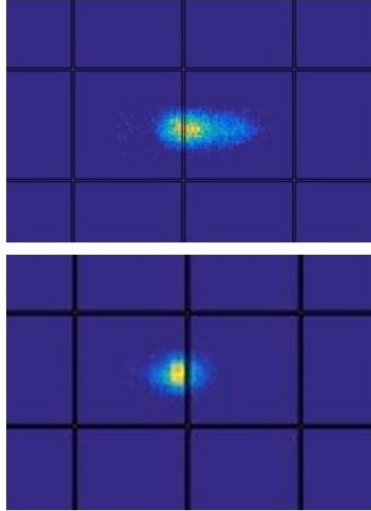


Figure 2.24: Zoom of the oblique irradiation spot before (top) and after (bottom) backward shift.

cause local differences. Therefore, the real behaviour is hard to predict by simulations. Nevertheless, simulations can still provide a first test to verify the feasibility of the method.

In figure 2.25 are highlighted the three irradiation spot positions that were analysed through simulations.

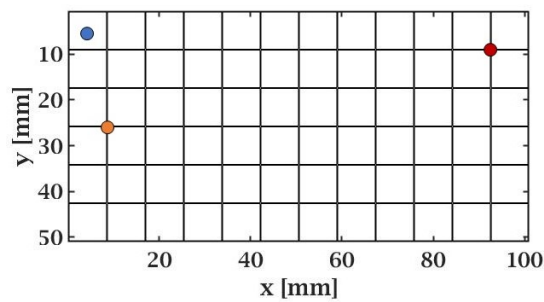


Figure 2.25: Lateral spot positions analysed with simulations in ANTS2.

- The first case corresponds to the irradiation spot placed above the center of a SiPM, on the corner or on the border of the crystal (shown in blue). In this case the reconstruction method is still able to distinguish between four different DOI regions, even if with per-

centages of correct classification lower than the ones relative to more central positions (figure 2.26(a) on the facing page).

- The second analysed case was that of the irradiation spot placed on the crossing point between four different SiPMs (shown in yellow). In this circumstance only two groups can be distinguished with satisfying results (figure 2.26(b) on the next page). In principle, a 2-group-based classification is enough for the requirements of the clinical INSERT module. However, dedicated adjustments could provide, if necessary, the possibility to perform a calibration with an adaptive number of groups, dependent on the X,Y coordinates.
- Finally, the most critical position corresponds to the irradiation spot located on the crossing point between the four SiPMs at the corner of the crystal (shown in red). This case shows the highest degree of overlapping (figure 2.27 on the facing page). Since this position is still inside the UFOV of the camera, in order to provide a complete calibration of the crystal, a different and specific strategy may be required.

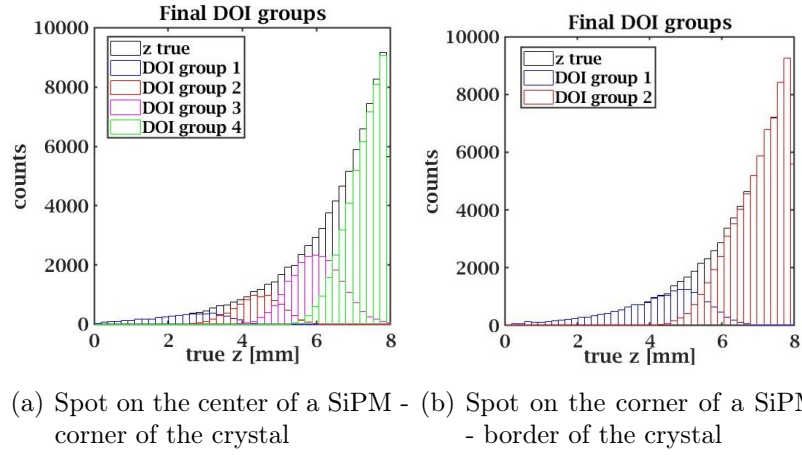


Figure 2.26: Histograms of true Z scintillation coordinates. The final DOI groups are shown in different colours.

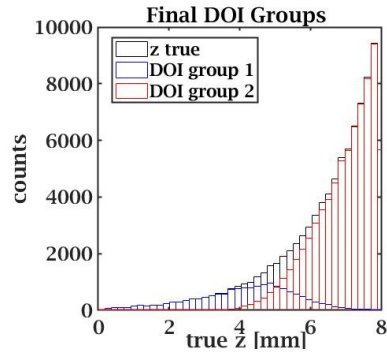


Figure 2.27: Histograms of true Z scintillation coordinates. Simulated gamma events belong to a collimated spot laying over the position in red in figure 2.25.

Chapter 3

GAMMA: position reconstruction

This chapter presents different algorithms for the position of interaction reconstruction of γ -rays inside the scintillator crystal of the GAMMA system. The first part illustrates the motivations behind this project, and proposes a reconstruction method based on cross-correlation. The final part presents an in-depth analysis of the data distribution and shows the experimental results achieved with different ML techniques.

3.1 GAMMA imaging: motivation and experimental setup description

3.1.1 Position reconstruction in GAMMA system

One of the requirements that GAMMA project has to fulfill, consists in the ability to provide the position of interaction of every single absorbed γ event, with a precision of about 1 cm. The need of this information comes from the necessity to compensate the Doppler broadening effect which, in the nuclear physics experiments where the GAMMA instrument is used, where radioactive sources moving at relativistic speeds are created as a result of high speed collisions in particle accelerators, causes a broadening

of the energy spectrum (figure 1.20 on page 30). If this Doppler effect induced peak broadening is not prevented, it could become impossible to distinguish emission peaks of different radionuclides one another, making the good energy resolution achieved by the instrument useless.

However, from the knowledge of the interaction point of the γ -ray inside the scintillator crystal, an estimate of the angle θ between the emitter and the γ -photon velocity directions can be provided, which makes possible to compensate the Doppler broadening.

Nonetheless position reconstruction in GAMMA project represents a complex problem. Indeed, to improve the performances in terms of energy resolution, the employed $\text{LaBr}_3(\text{Ce}^{3+})$ crystal is entirely embedded in a highly reflective Teflon layer, except for the base in contact with the SiPM array, which is covered by a transparent output window. Therefore scintillation photons reaching the borders of the crystal are reflected by the paint layer and undergo diffuse scattering, losing information on their original direction (figure 3.1 on the facing page). These photons are of little use for position reconstruction.

It should be emphasized that this phenomenon happens also in the scintillator used in INSERT project, however, in that case, a very thin crystal (just 8 mm thickness compared to the 3 inches $\approx 76,2$ mm of GAMMA project) is employed, therefore there is less space for photons to diffuse away from their original scintillation position and so the effect is less pronounced.

Nevertheless, part of the scintillation light is reflected specularly by total internal or Fresnel reflection from the crystal-paint interface, creating spatial patterns (caustics) on the output window [49].

The fraction of specularly reflected light increases with the ratio between the refractive indices of the material and of the paint base.

As shown in figure 3.2 on page 78, varying the position of absorption of the γ -ray, the shape of the light patterns changes: this suggests that, even if complicated by the large dimensions of the crystal and by the presence of the external reflective layer, the signal detected by the SiPMs depends on the scintillation position, therefore the reconstruction of the position

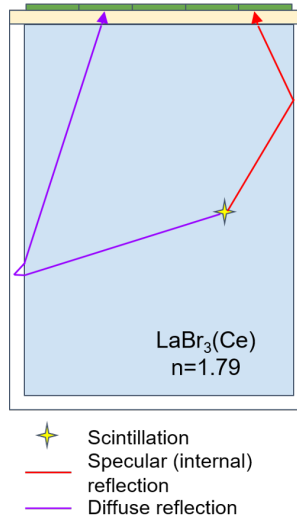


Figure 3.1: *Optical model of the scintillator crystal. In magenta is shown the path of a scintillation photon entering the paint layer, which diffuses by scattering and therefore loses information on its original direction. In red is shown the path of a scintillation photon subject to Fresnel reflection from the crystal-paint interface.*

of interaction is possible.

Summarizing, due to the geometry of the crystal and to photon reflections at the borders, the position reconstruction task is much more complex in this case with respect to INSERT one. However, it should be reminded that the requirements in terms of spatial resolution are different: less than 1 mm for INSERT, compared to just 1 cm for GAMMA, justified by the fact that the only objective of the position reconstruction is the correction of the Doppler effect.

Objective of this thesis work is the development of a reconstruction algorithm of the position of interaction able to satisfy this requirement for the 8-channel version of the system: the original 144 SiPMs are not connected individually to a dedicated ASIC (as it will be in the final version of the system) but the SiPMs signals are summed among them to get just 8 output signals to be delivered to a single 8-channel ASIC.

A previous work carried out in collaboration with the University of Coimbra, Portugal, [49] showed the possibility to perform 3D reconstruc-

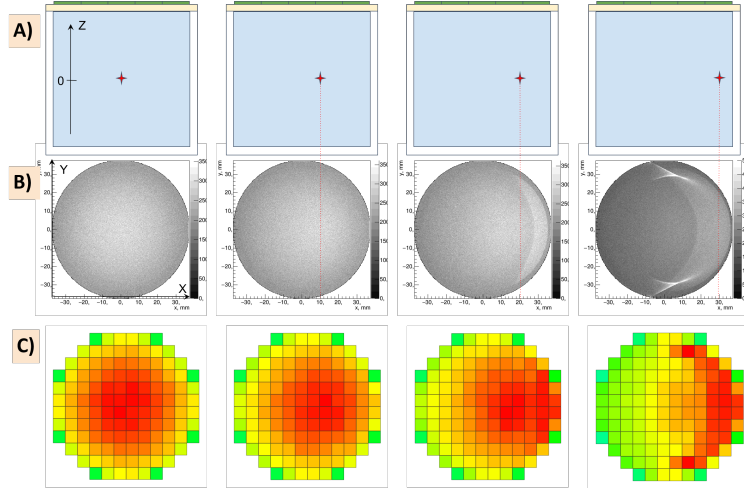


Figure 3.2: *Dependence of the light patterns at the output window on the position of interaction of the γ -ray. Results from ANTS2 package simulations of a LaBr_3 crystal coupled with the 144-SiPM matrix: a) scintillation position, fixed in the middle of the crystal ($Z = 0$), moving along the X axis; b) scintillation light distribution across the output window; c) average signal detected by the elements of the SiPM array [49].*

tion of the position of interaction, with a spatial resolution no worse than 10 mm in the SiPM plane and of 15 mm for the depth of interaction, exploiting the dependence of the light patterns with the absorption position of the γ -ray. However this result was validated just from simulations and moreover it used the signal detected by each one of the 144 SiPMs. So, if validated experimentally, it could be a solution of the reconstruction problem for the final 144-channel system, however for the 8-channel system adopted in this thesis work a new approach had to be conceived.

3.1.2 Experimental setup

In principle, if the incoming γ -ray can reach the scintillator crystal from whichever direction, a 3D reconstruction of the absorption position is needed in order to be able to correct for the Doppler effect. However, as a first step, the direction of the γ -rays to be detected was assumed to be fixed, so that the position reconstruction task consists just in the definition of a 1D coordinate. With these premises, the merging of the

SiPMs signals to get just 8 output channels was devised in order to maximize the linear position sensitivity along one axis: the equivalent pixels are arranged as parallel stripes perpendicular to the input direction of the γ -ray, as shown in figure 3.3(a) on the following page. This merging solution will be referred to as "Imaging Configuration". As evident from the figure, central pixels are constituted by half of the number of SiPMs with respect to lateral pixels. This is due to the fact that pixels on the sides collect less light since they are under the periphery of the crystal and so are only partially covered by it. Therefore, in order to have all the pixels collecting approximately the same amount of light, lateral pixels were devised to be constituted by a larger amount of SiPMs.

Another possible merging arrangement, referred to as "Spectroscopy Configuration", is shown in figure 3.3(b) on the next page and was devised specifically for the spectroscopy task: in order not to limit the Dynamic Range (DR) of the system, the merging approach was aimed to level out the signals coming from the merged detectors so that saturating events are evenly shared between all the channels. In this way the system is not limited in DR by a channel collecting more light than the others. To this aim, each readout channel is connected to the same number of SiPMs but arranged in such a way that the light is uniformly distributed between the different channels: SiPMs from the matrix center, which collect more light, are connected to the ones from the sides, that detect a lower amount of light, due to the fact that they are only partially covered by the crystal surface. As shown in the figure, the eight pixels contain 16 SiPMs each, for a total of 128 detectors, while the remaining 16 on the corners are discarded and are not connected to any of the ASIC input since they are not covered by the scintillator crystal and thus they would only add dark counts without contributing to the useful signal.

The reconstruction methods, that will be illustrated in the following sections, have been developed in MATLAB environment and tested on experimental data taken from measurements which have been performed in the laboratories of Istituto Nazionale di Fisica Nucleare (INFN), located inside Università degli Studi di Milano in via Celoria, that have at their

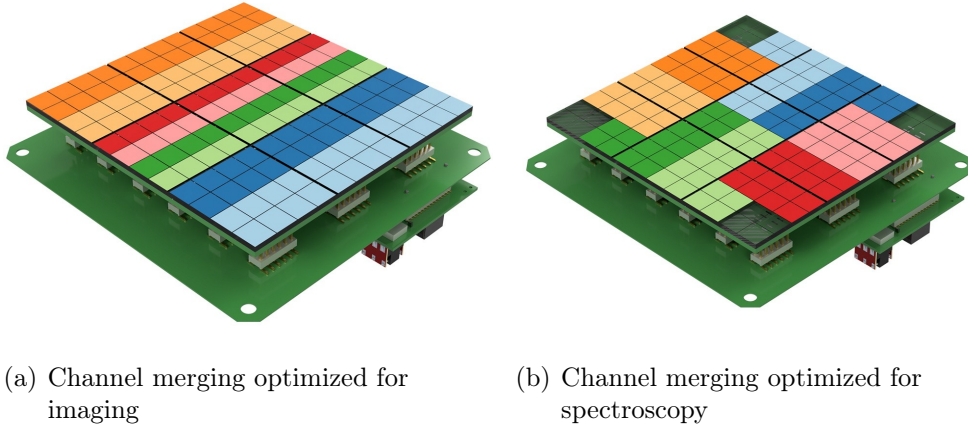


Figure 3.3: *The two different SiPMs merging strategies: each colored group corresponds to a pixel and is connected to one of the eight inputs of the GAMMA ASIC. For spectroscopy, the distribution of the analog channels is made in such a way that the impinging light across the matrix is equally spread among the different ASIC channels. For imaging, instead, the distribution is such that the linear position sensitivity along one axis is maximized.*

disposal a collimated source of radioactive ^{137}Cs , which can be used to irradiate the scintillator crystal in precise spots. The activity of the ^{137}Cs source is 480 MBq and it is encapsulated in a Tungsten-composite collimator, which collimates the source in a small beam with a spot size of 1 mm diameter, while shielding the radiation on all the other directions, thanks to the high density of the material used (up to $18,5\text{ g/cm}^3$), which is almost a factor 2 higher than Lead. The scintillator crystal was placed at a distance of about 10 cm from the collimator, facing it from the base side in order to have the collimated beam perpendicular to the SiPM matrix, which represent the $x - y$ plane. The described experimental setup is shown in figure 3.4 on the facing page.

The idea behind these measurements is that of performing acquisitions with fixed X coordinate, so where the absorbed events are all characterized by the same coordinate of interaction. By moving the collimator in the vertical direction, several acquisition can be obtained, each one constituted by events with a different specific X coordinate.

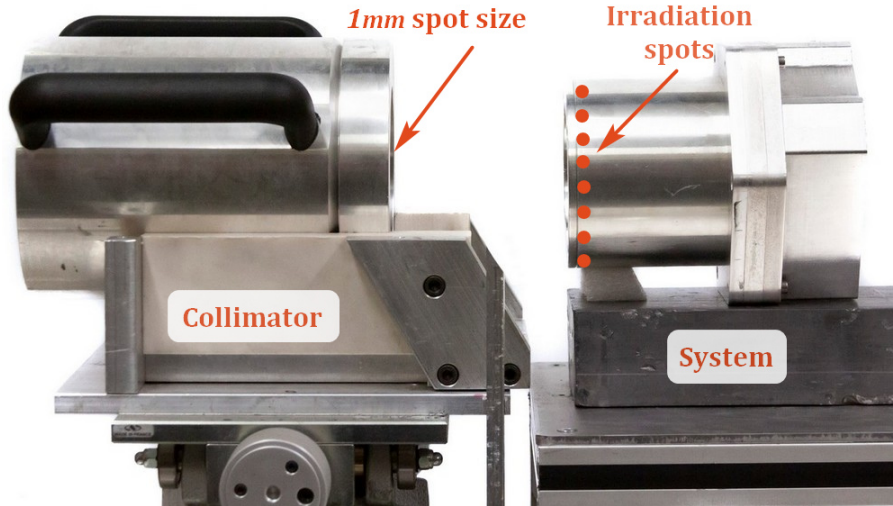


Figure 3.4: *On the left there is the collimator, whose position can be changed with high precision on the vertical direction, while on the right is visible the designed detector housing containing the crystal, the SiPMs and the readout electronics.*

3.2 Cross-correlation reconstruction algorithm

Employing the SiPMs merging configuration for imaging and assuming an incoming γ -ray entering the crystal along the direction perpendicular to the parallel pixels, the goal is to reconstruct the 1D coordinate of interaction of each γ -photon absorption event.

The first reconstruction algorithm that was tried can be subdivided in two phases: in the first step, which acts as a calibration phase, a series of 8 consecutive irradiations along the X axis was performed and the average signal detected by every pixel for each irradiation position was computed; in the second phase, instead, the real acquisition, whose events have to be reconstructed, is performed and the signal distribution of each event is stored. In figure 3.5(a) on the next page are schematically shown the spots irradiated during calibration.

The method then computes the cross-correlation, between the average light distribution for each irradiation position and the light distribution of each event that has to be reconstructed, and exploits this information

to assign the X coordinate of each event to one of the eight irradiation positions.

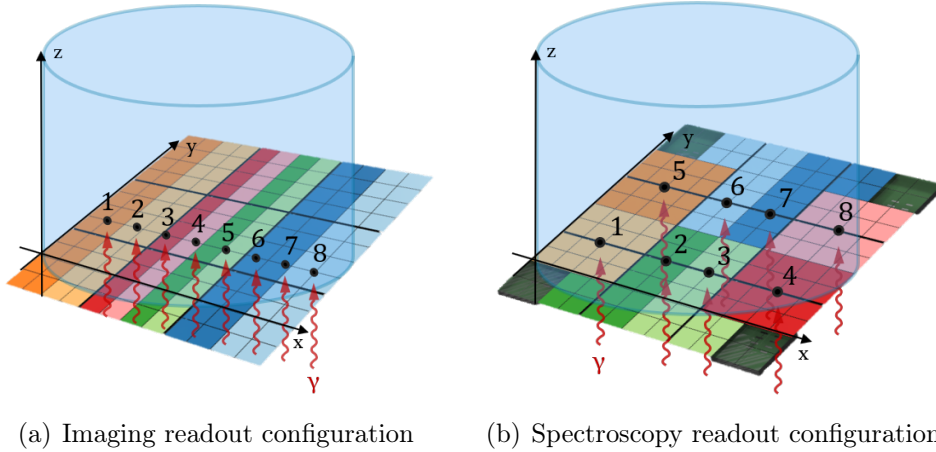


Figure 3.5: Schematic representation of the SiPMs merging configuration coupled with the scintillator crystal. The red arrows illustrate the spots irradiated during the calibration phase.

3.2.1 Algorithm working principle

The experimentally acquired data of the calibration phase are transmitted to the MATLAB environment where the script implementing the algorithm is defined. The data are expressed in the form of 8 $N \times M$ matrices, each one for a given irradiation position, where N is the number of detected events and M is the number of channels of the system (in this case equal to 8).

As a first step, the data corresponding to saturated channels are discarded. Then the histogram of the overall signal for all the events is generated, so that an energy filtering operation can be performed by selecting only the events whose energy is inside a window centered around the Cesium photopeak position, employing a Gaussian fitting. Subsequently, for each one of the 8 matrices, the mean value along the columns is computed, so that the vector containing the average signal of every pixel for a given position of irradiation is obtained. Since the relevant

information, in terms of the position reconstruction, is given just by the difference between the signal of the pixels, the baseline value, determined as the minimum value between the signals of the vector, is subtracted to all the vector components. Eventually, a final matrix, which will be referred to as $R_{average}$, is generated by piling-up the vectors corresponding to each irradiation position.

In figure 3.6 is represented the set of the average signal distributions obtained during the calibration phase: each curve corresponds to an irradiation, using the collimated ^{137}Cs source, above one of the 8 stripes of merged SiPMs.

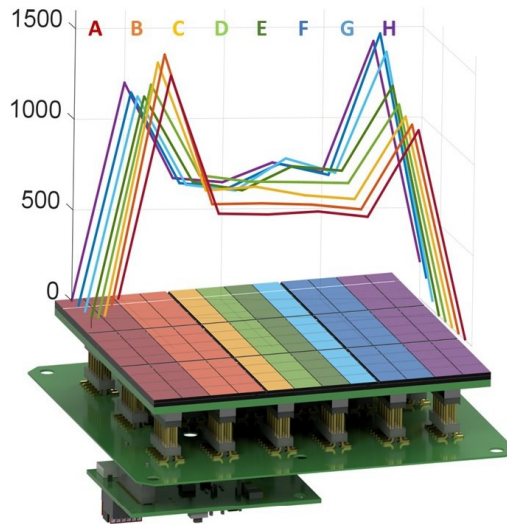


Figure 3.6: Average signal distribution for the 8 different positions of irradiation corresponding to the centers of the pixels.

Also in the acquisition phase the measured data are made available in MATLAB in the form of $N \times M$ matrices and are then processed by discarding the events characterized by saturated channels and having energy outside the window centered around the ^{137}Cs photopeak. Afterwards, the baseline value is subtracted to all the events and the final matrix, which will be called $R_{acquisition}$, is obtained.

Once the data have been processed, the cross-correlation coefficient between the signal distribution of the acquired event and the average

signal distribution, stored in the calibration phase, for each position of irradiation is computed. The computation is performed for all the events that have to be reconstructed (so for each row of the acquisition matrix) so that, eventually, a $N \times P$ matrix is obtained, where N is the total number of events and P is the number of irradiation positions scanned during the calibration phase. Each element of this matrix thus corresponds to a cross-correlation coefficient computed with the formula:

$$C(i, j) = \frac{R_{acquisition} \cdot R'_{average}}{R_{acquisition} \cdot R'_{acquisition} + R_{average} \cdot R'_{average}}$$

The higher is the coefficient value $C(i, j)$ the higher is the correlation between the light distribution of the i event and of the j irradiation position. From this consideration, the X coordinate of the i event can be assigned to the position of irradiation, among the 8 scanned during the calibration, that presents the highest cross-correlation coefficient.

In figure 3.7 on the next page the histograms of the reconstructed positions of interaction are reported: they show the distribution of probability of reconstructing an event in a specific calibration spot position along the X axis. Each histogram is relative to events belonging to a collimated irradiation on a particular position along the X axis: position "A" corresponds to an irradiation above the most on the left pixel, while position "H" to an irradiation above the most on the right pixel. Therefore, for the algorithm to work correctly, the peak of the histograms should move from the mostleft position on the X axis to the most on the right one, meaning that, as the collimated irradiation position moves to the right, the method assigns the majority of the events to the correct irradiation position. As evident from the figure this behaviour is respected, validating the goodness of the algorithm.

The standard deviation of the reconstructed position is also reported above each histogram: it is lower than 1 cm for the events near the center of the SiPM matrix, where the pixel size is smaller, while it gets larger (but always below 1,5 cm) when the interaction is closer to the lateral, highly-reflective surfaces of the crystal.

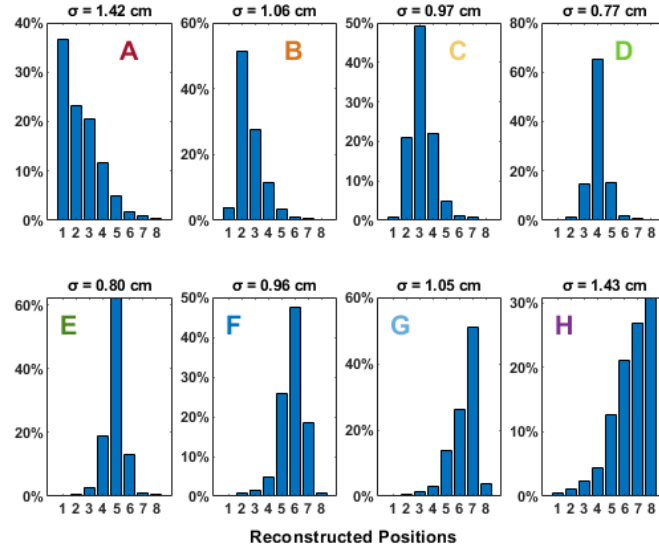


Figure 3.7: Histograms of the reconstructed positions of interaction using the cross-correlation-based algorithm. On the X axis are reported the 8 irradiation positions, disposed along a 1D axis, scanned during the calibration phase. On the Y axis is presented the percentage of events reconstructed in each calibration position. Each histogram is relative to reconstructed events belonging to a specific position of irradiation along the 1D axis. Above every histogram is reported the value of the corresponding standard deviation σ of the reconstructed position.

3.2.2 Border light contribution

From ANTS2 simulations, the contribution given by the light coming from the borders of the crystal appears to be constant independently of the position of absorption of the γ -ray, so it is not useful for the task of distinguishing events absorbed in different positions. Therefore, it was decided to investigate the effect played by this light contribution on the position reconstruction, by positioning a ring mask, of 0,5 cm width, able to stop the scintillation light, between the base of the crystal and the SiPM matrix.

In figure 3.8 on the following page are shown the resulting histograms of the reconstructed positions when the ring mask is employed.

By comparing the results obtained with and without the use of the mask ring, it can be noticed that, due to its employment, the reconstruc-

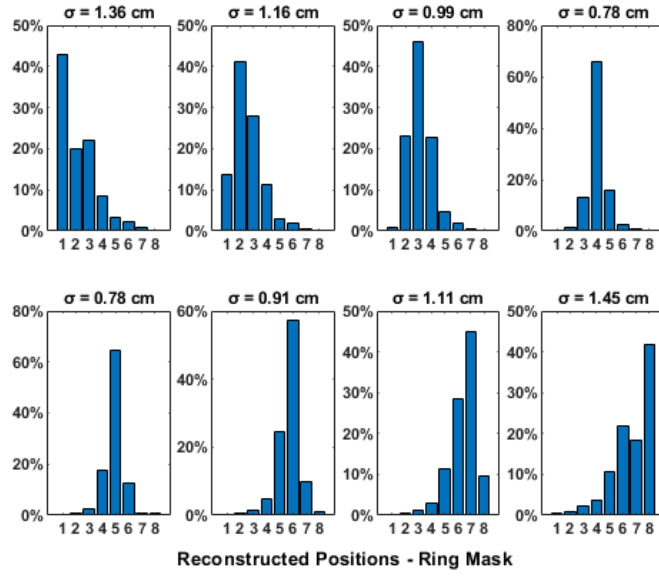


Figure 3.8: Histograms of the reconstructed X coordinates of interaction using the cross-correlation-based algorithm and employing a 0,5 cm width ring mask to discard the light contribution coming from the borders of the crystal.

tion slightly improves only in some irradiation positions, while in others there is a worsening. This could be explained considering that, discarding the border light contribution, two effects come into play: given that a useless and not dependent on the interaction position contribution is being neglected, an improvement is expected since more importance is given to the meaningful contributions; however, at the same time, less data are available to characterize more in depth the average signal distribution of each specific irradiation position, therefore the different average signal vectors could become more similar one to another and the assignment of an event to one their position is an harder task. For these reasons the adoption of the ring mask does not bring to a clear improvement.

3.2.3 Reconstruction of intermediate positions

To further validate the method, it was decided to verify whether the algorithm is able to reconstruct the coordinate also of events belonging to collimated irradiations in positions different from the ones scanned during

the calibration phase. Therefore, following the calibration phase, where a collimated irradiation is performed in 8 different positions equally spaced along the X axis, a second series of collimated irradiations, whose events have to be reconstructed, is executed in the 7 positions among the calibration ones. In figure 3.9 are represented the histograms of the reconstructed positions: in this case, as expected, the histograms don't show a single peak but, since the γ -photons are absorbed in the middle of two calibration spots, they are characterized by a double peak which moves to the right as the collimated γ irradiation is shifted. This means that the algorithm correctly tends to assign the events to the two adjacent calibration spot positions: half of the times to the calibration spot on the right and the other half of the times to the the one on the left.

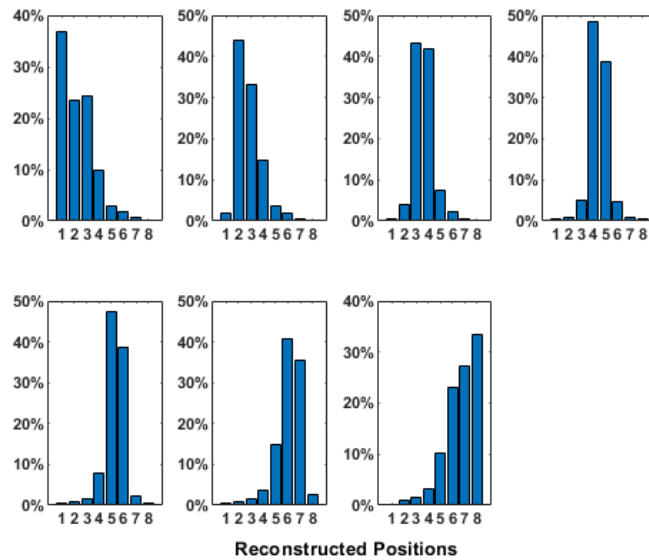


Figure 3.9: Histograms of the reconstructed X coordinates of events belonging to collimated irradiations in positions different from the ones scanned during the calibration phase. A 0,5 cm width ring mask is employed and the reconstruction is performed through the cross-correlation-based algorithm.

3.2.4 Reconstruction of XY coordinates

Up to now it was explored the system ability to reconstruct just one coordinate of interaction along the X axis. The usage of the SiPMs merging configuration for imaging (figure 3.3(b) on page 80) intrinsically preclude the possibility to test also the capability to contemporary reconstruct both the X and Y coordinates of interaction, due to the fact the pixels discriminate the crystal only along the X direction, providing no information about the Y coordinate. Therefore, to examine also this feature, a different pixel arrangement must be employed.

The spectroscopy SiPMs merging configuration (figure 3.3(a) on page 80), even if it was not conceived for imaging purposes, allows the contemporary X and Y coordinates reconstruction, since the pixels subdivide the crystal both in the X and Y directions. Therefore the cross-correlation reconstruction method was applied adopting this readout configuration. This time, in the calibration phase, the collimated irradiations were not scanned along a single direction, but were distributed as two rows of 4 spots each, as shown in figure 3.5(b) on page 82. In this way it can be tested the ability of the system not only to distinguish events among 4 position on the X axis, but, at the same time, also to discern among two possible points in the Y direction. In figure 3.10 on the next page are reported the histograms showing the distribution of probability of reconstructing an event in a specific calibration spot position on the XY plane. Each plot is relative to events belonging to a collimated irradiation on a particular position.

It can be noticed that if compared to the results obtained for the reconstruction of just the X coordinate (figure 3.7) the algorithm seems to perform better in this case. This is due to the fact that, in the spectroscopy readout configuration, the spots irradiated during the calibration phase are further apart from each other, therefore their signal distribution have less similarities between them and the computed cross-correlation coefficients have more disparate values, making easier the classification.

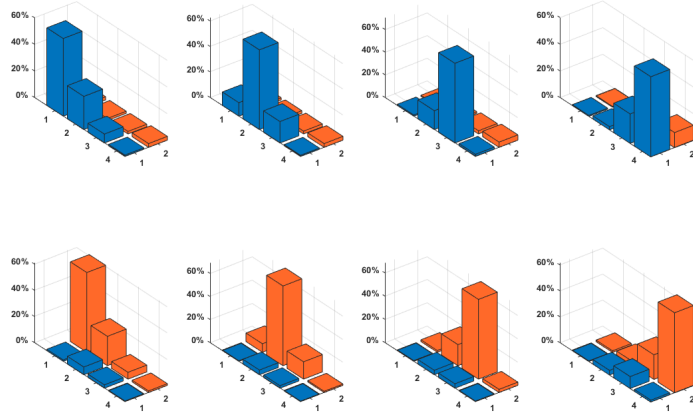


Figure 3.10: *Histograms of the reconstructed XY coordinates of interaction using the cross-correlation-based algorithm. On the X and Y axis are reported, respectively, the X and Y coordinate of the 8 irradiation positions scanned during the calibration phase. On the Z axis is presented the percentage of events reconstructed in each calibration position. Each histogram is relative to reconstructed events belonging to a specific position of irradiation in the XY plane.*

3.3 Machine Learning reconstruction algorithms

With the aim of further improving the spatial resolution of the reconstructed position of interaction of the γ -ray, other approaches were explored besides the cross-correlation method already discussed. In particular different Machine Learning (ML) based reconstruction algorithms were tested.

A possible definition of machine learning algorithm is: a method that, starting from the analysis of a large number of observations, is able to look for patterns in data and make better decisions in the future or predict characteristics of new samples, without human intervention but based only on the analysis of the examples that were provided.

The adopted approaches and the obtained results will be illustrated in the following sections.

3.3.1 Data distribution analysis

In order to grasp a deeper understanding of the problem, before covering the actual reconstruction algorithms, a preliminary discussion on the distribution and on the characteristics of the data to be analysed, should be carried out.

To begin, we introduce in the following some vocabulary that will be adopted throughout this chapter.

We assume to have an object that has to be classified choosing among a set of specifications, named *classes*. An example could be a flower that can be classified as a rose, a sunflower or a daisy. Machine learning classification algorithms are able, on the basis of the informations given by the *features* or *predictors* of the object, in this case represented by the colour and shape of the petals, to assign the correct class to the flower.

According to the same principle, the problem of reconstructing the original position of absorption of a γ -ray can be addressed using machine learning classification algorithms. Indeed the objects to be classified are constituted by the γ absorption events, the object features, based on which the classification is carried out, are the detected pixel signals for each scintillation event and the possible classes that can be assigned are represented by the positions of the calibration spots.

The concept on which is based the ML algorithm is that, providing many labeled data as a training dataset, the algorithm is able to find a pattern between the features and the classes of the data, therefore, if a new sample with an unknown class is given, the method is able to predict its correct class.

When reconstructing the position of γ events, the training dataset is constituted by the pixels signals of the calibration events combined with the information on the position of the collimated irradiation to whom the event belongs. Thus if a new γ absorption event, not belonging to the calibration phase, is detected, its position can be found on the basis of the training dataset.

This particular type of machine learning approach, where the algo-

rithm learns from labeled training data is called supervised learning.

The overall dataset available for the reconstruction task is constituted by 35k events for each position of irradiation (so for each *class*), thus, since 8 collimated spots were irradiated, on the whole, it consists of 280k events. In figure 3.11 is reported the structure of the overall dataset matrix containing the pixel signals for all the absorption events.

	1 Pix_1	2 Pix_2	3 Pix_3	4 Pix_4	5 Pix_5	6 Pix_6	7 Pix_7	8 Pix_8	9 Classi
1	1092	2395	1805	1706	1868	1791	2242	1049	6
2	1092	2281	1689	1673	1753	1753	2731	1554	8
3	1134	2398	1791	1830	1772	1819	2287	1042	3
4	1041	2294	1724	1749	1831	1770	2366	1078	6
5	1085	2277	1733	1669	1877	1774	2417	1106	7
6	1086	2886	1746	1944	1687	1658	2088	973	3
7	1064	2238	1692	1657	1845	1759	2316	1003	2

Figure 3.11: Matrix of the pixel signals dataset. Each row corresponds to a specific scintillation event. The first 8 columns represent the 8 different pixels, while the last column reports the position of the collimated irradiation to whom the event belongs (a number from 1 to 8). Notice that the matrix is truncated at the seventh event but it actually continues up to the event number 280k.

A problem that is related to the structure of the machine learning task has now to be highlighted. The conflict arises from the fact that a learning algorithm is trained on a set of training data, but then it is applied to make predictions on new data points. Thus, the goal is to maximize its predictive accuracy on the new data points, not on the training data. From this consideration it derives that if the method becomes too accurate in the prediction for training data, there is the risk that it will fit the noise in the data by memorizing various peculiarities of the training dataset rather than finding a general predictive rule [51]. This phenomenon is usually called overfitting.

To avoid the overfitting phenomenon a subdivision of the overall dataset in *training*, *validation* and *test* subdatasets is performed: in this way the model is fit on the training dataset but then it is used to predict the classes of the events of the validation dataset. The test dataset is kept separated for a final evaluation of the model.

In particular the training dataset is constituted by 23k events for each

class, so overall 184k events; the validation and the test dataset, instead, are composed by 6k events for each class, which means a total of 48k events each.

A useful operation, that can bring to an improvement in the classification task, which can be done before addressing the actual ML reconstruction methods, is to analyse the distribution of the training data in the features space, in order to identify the predictors that well separate events of different classes and then exclude the less meaningful ones which don't.

It should be emphasized that, in the case of the 8-channels system, the features space is constituted by an 8-dimensional space. Therefore the correct way to detect the predictors that best discern events of different classes would be to look for them in an 8-dimensional space, which is not an intuitive and easy task. However, single pairs of features can be separately analysed, so the distribution of data can be easily examined on a 2-dimensional scatter plot. In figure 3.12 are shown various scatter plots obtained by changing, as X and Y axis, different pairs of predictors.

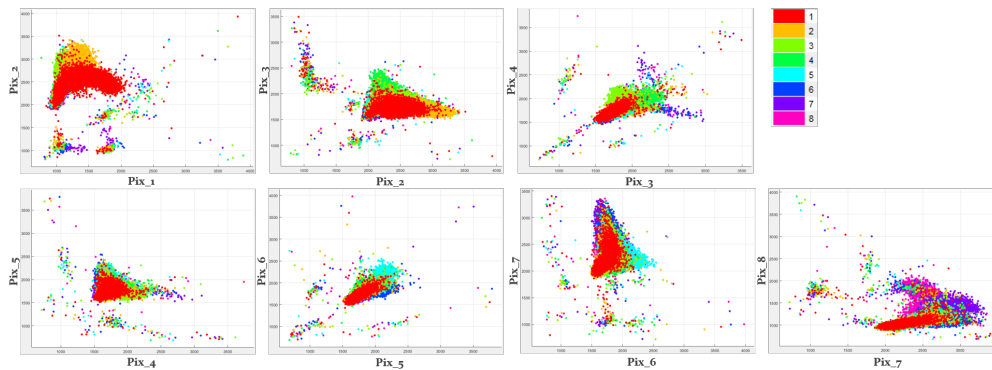


Figure 3.12: Training data scatter plots. Each plot presents, as X and Y axis, a different pair of features. Considering a specific plot, every dot represents an event, while the different colors represent the 8 different classes, according to the key at the top right.

As can be seen from the figure, regardless of the pair of predictors chosen, events belonging to different classes seem to never be well separated, thus features more useful than others for the classification task cannot be

identified. Moreover, this means that datapoints of different classes are characterized by similar features: this implies that events belonging to different irradiation points generate similar pixel signals.

These considerations confirm that the position reconstruction is not an easy task in the 8-channel GAMMA system, as events absorbed in different position produce similar pixel signals.

3.3.2 K-NN reconstruction method

In the following sections it will be described how different machine learning classification algorithms, working on the training dataset, are able to classify the position of absorption of the γ -ray to one of the 8 positions of the calibration spots.

The first algorithm that will be illustrated is the K-Nearest Neighbours (K-NN) method. The basic working principle is: considering that the event that has to be classified is represented as a point in the n-dimensional (8 dimensions in this case, since there are 8 features) space of the training dataset, the distances between this event and all the events of the training dataset are computed and eventually the event is assigned to the class that appears most frequently among the K-nearest training datapoints.

As an example, in figure 3.13 on the following page is shown the features space for a fictitious 3-dimensional case, where the detector matrix is constituted by just 3 pixels. The figure is divided in three parts, each of which corresponds to the case of a collimated γ irradiation right above the center of a specific pixel: for example, in the first case a γ -ray is directed above the pixel P_1 , therefore this pixel will detect a much larger amount of scintillation photons with respect to P_2 and P_3 ; consequently, in the feature space, the points corresponding to the absorbed events will be concentrated in a confined region along the P_1 axis.

According to this reasoning, events absorbed in a specific region of the crystal are characterized by similar pixels signals values, thus are concentrated in a definite region in the predictors space. Therefore, if a new event has to be reconstructed, its class can be deduced by looking at the

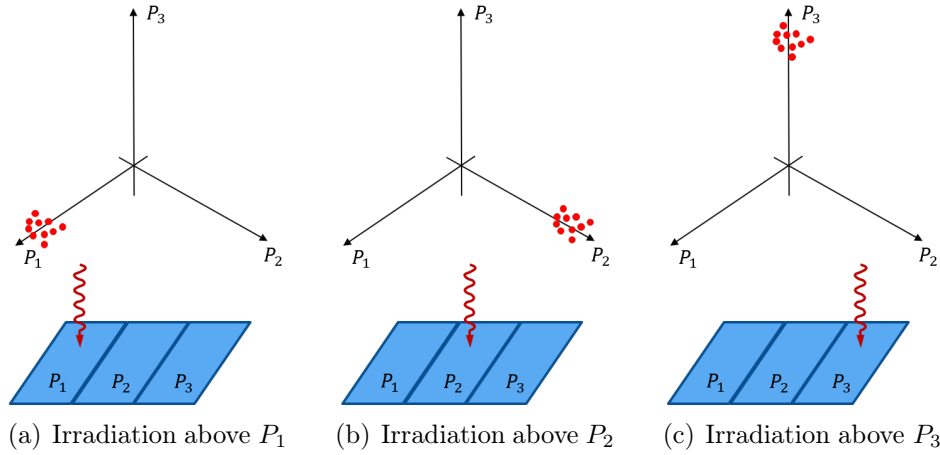


Figure 3.13: *Example of a 3-pixel system. The three cases of collimated γ irradiation right above each pixel are reported: for each of them are represented the interaction events (red dots) in the 3-dimensional features space and, below, a schematic illustration, of the γ irradiation with respect to the detection matrix.*

classes of the K events closest to it.

In figure 3.14 on the next page is illustrated an example where K is chosen equal to 7, so the class of the new event is derived by looking at the 7 closest training datapoints.

K-NN application for X coordinate reconstruction in GAMMA system

For the implementation of the K-NN-based reconstruction algorithm with the dataset of the GAMMA system, a MATLAB application called Classification Learner has been used.

For the evaluation of the goodness of the reconstruction, adopting a specific ML method, the application uses the validation accuracy, which is defined as the opposite of the validation error, that corresponds to the percentage of times in which an event is not classified in the correct class.

For the computation of the validation error, to avoid the overfitting phenomenon, the k-fold cross-validation technique is adopted.

According to this technique, the training dataset is divided into k sub-

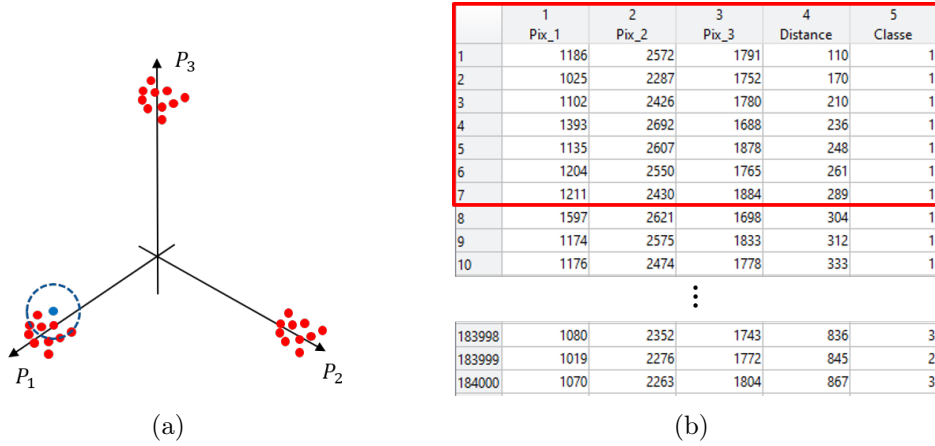


Figure 3.14: Example of K -NN classification, using $K=7$, in a 3-dimensional system. a) The red dots represent the training datapoints; the blue dot is the event that has to be classified. The dashed circle is a visual representation of the area inside which are contained the 7 closest training points. b) Each row of the matrix corresponds to a specific event of the training dataset; the columns, instead, report: the signals of the 3 pixels, the distance with respect to the new unclassified event, the class. Notice that the rows of the matrix are ordered with the increasing of the distance parameter, therefore the red box highlights the 7 closest training datapoints whose class has to be considered.

sets of approximately the same size, then the first subset is treated as a validation dataset to be fitted on the remaining $k-1$ folds. This procedure is repeated k times, each time using a different subset as validation dataset, and results in k estimates of the test error which are then averaged out. It should be emphasized that the k value corresponds just to the number of subsets in which the training dataset is divided for the cross-validation operation, it has nothing to do with the K value, which represents the number of nearest neighbours to be considered for the classification task in the K -NN algorithm.

For the computation of the validation error, using the cross-validation technique, a value of $k = 8$ was chosen.

To examine the performance of a ML classifier, a commonly adopted instrument is the confusion matrix. In figure 3.15 on the following page is shown the confusion matrix resulting from the application of the K -NN algorithm to the GAMMA collimated irradiations training dataset,

arbitrarily imposing $K = 100$ and the Euclidean distance as the metric used for the calculation of the nearest neighbours.

1	51%	22%	13%	7%	3%	2%	1%	1%	
2	12%	56%	20%	7%	2%	1%	1%	1%	
3	3%	15%	59%	16%	4%	2%	1%	1%	
4	1%	3%	15%	61%	14%	3%	1%	1%	
5	1%	1%	3%	15%	61%	14%	3%	2%	
6	1%	1%	2%	4%	16%	58%	14%	4%	
7	<1%	1%	1%	2%	6%	18%	58%	13%	
8	1%	1%	2%	3%	7%	11%	23%	52%	
		1	2	3	4	5	6	7	8
		Predicted class							

Figure 3.15: Confusion matrix for the X coordinate reconstruction using K -NN algorithm with $K = 100$ and Euclidean metric.

The rows of the matrix show the true class of the events to be classified, while the columns represent the class predicted by the algorithm. The predictions are obtained through 8-fold cross-validation on the training dataset. The percentage value reported in each cell represents the fraction of events that are classified in that class. It should be noticed that the diagonal cells show where the true class and the predicted class match: if these cells are green, it means that the classifier has performed well and has correctly classified the events of the given true class.

In this case, the overall validation accuracy obtained is of 57%. However, it is evident from the figure, that the prediction accuracy of the algorithm is not the same for every class. Indeed, the method appears to be more effective in the reconstruction of events absorbed in the central area of the crystal, while its accuracy decreases for classes at the borders.

To further validate the algorithm, the classifier has to be used on new data, different from the ones used for the training phase, so the validation

subset, which was previously created, is employed. In figure 3.16 the histograms showing the distribution of probability of reconstructing an event in one of the 8 positions along the X direction are reported.

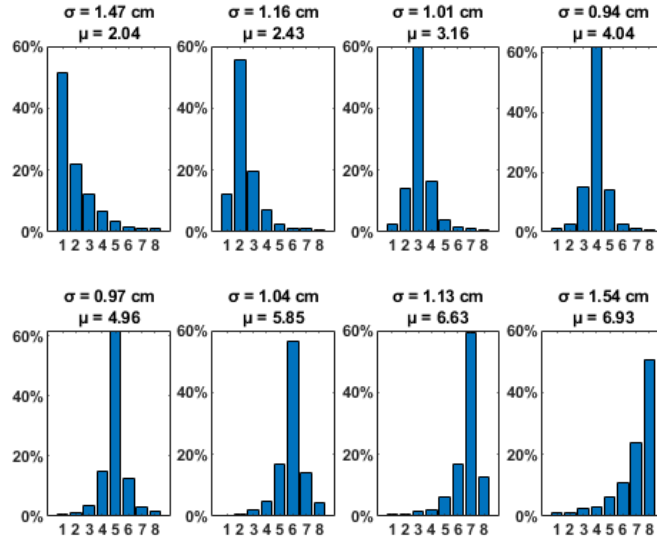


Figure 3.16: Histograms of the reconstructed X coordinates using the K-NN method with $K = 100$ and Euclidean metric. Above every histogram are reported both the mean value and the standard deviation of each distribution.

From the figure, it can be noticed that the accuracy of the predicted classes is consistent with the validation accuracy found with the cross-validation approach on the training dataset. Moreover, if compared to the results obtained in figure 3.7, where the cross-correlation method was adopted, it is evident that the K-NN method guarantees much higher performances: the accuracy is better for every absorption position inside the crystal, and there is a clear improvement especially for the classes at the borders.

Hyperparameters Optimization

Machine learning algorithms are characterized by parameters which are external to the model and whose value cannot be estimated from data, but

must be set before the learning process. These parameters are referred to as *hyperparameters*.

In the case of the K-NN algorithm, the hyperparameters are the number of nearest neighbours K and the metric used to compute the distance. The reconstruction previously performed has been obtained by arbitrarily imposing $K = 100$ and the Euclidean metric. However, to try to improve the performance of the classifier, the hyperparameters of the model can be optimized.

The optimization procedure attempts to minimize the cross-validation error (or, equivalently, maximize the classifier accuracy) by varying the hyperparameters values: for example, to find the optimum value of K , means to identify the K value for which the misclassification error is the lowest.

However, it is important to underline that the search for the optimum K cannot be done by carrying out repeated measurements of the misclassification error for different values of K , because in this way the model will be incapable of generalizing to newer observations, so the overfitting phenomenon will occur. To avoid this, the hyperparameters optimization is carried out by means of a 5-fold cross-validation, the results of which are reported in figure 3.17(a) on the facing page.

Considering that the optimum values for the hyperparameters are the ones giving the lowest value of the cross-validation loss, expressed by the Z axis, a general trend can be derived from the plot: regardless of the metric used, a minimum of the cross-validation error is found around $K \approx 300$. Both decreasing or increasing K , an increase of the misclassification error is observed.

This could be explained taking into consideration the bias-variance trade-off. Indeed if K is too small the model is oversimplified and is affected by a high bias, which means that the algorithm is set to miss the relevant relations between features and classes, not fully exploiting the informations provided by the training dataset. Basically, since just a few closest neighbours are considered, it is more likely that noisy training data points, that are close enough to each other, outvotes the correct ones in

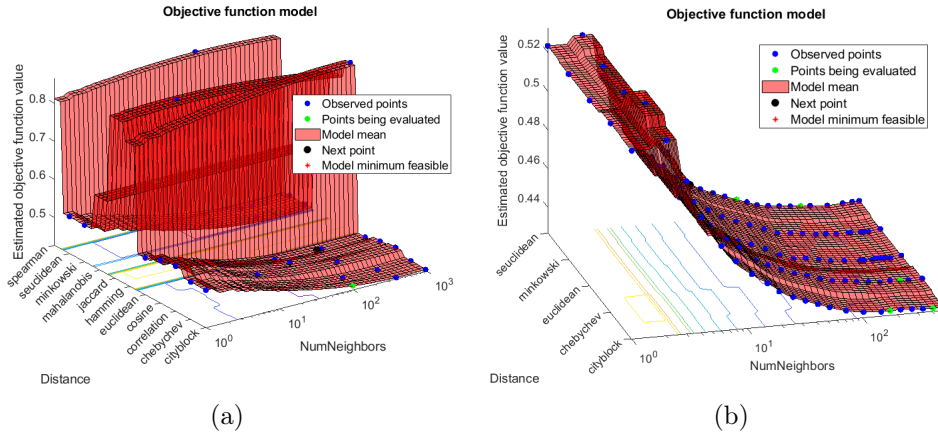


Figure 3.17: *K-NN hyperparameters optimization results. The Z axis shows the cross-validation loss, which is the parameter that has to be minimized. On the X and Y axis are reported the metric and the number of neighbours K. a) K is varied between 1 and 1000 and 11 different metrics are tried. b) K is varied between 1 and 500 and just the 5 best metrics are tried.*

some region.

If, instead, K is too large, the algorithm is affected by a high variance, which means that it presents a high sensitivity to small fluctuations in the training set. In other words, overfitting occurs and the model becomes too complex, so it predicts the training data too well and tends to model its random noise, losing the ability to generalize on data which have not been seen before.

Since from the optimization it appears that the best metric to employ is the Euclidean one (even if it is only slightly better than the other five best metrics), a second optimization process was performed, fixing the metric as Euclidean, to precisely identify the best K value. The result of this second optimization is illustrated in figure 3.18(a) on the next page.

Notice how from this plot the minimum of the error, around a value of $K \approx 300$, is more evident.

Besides the Euclidean metric, also the Minkowski distance shows good

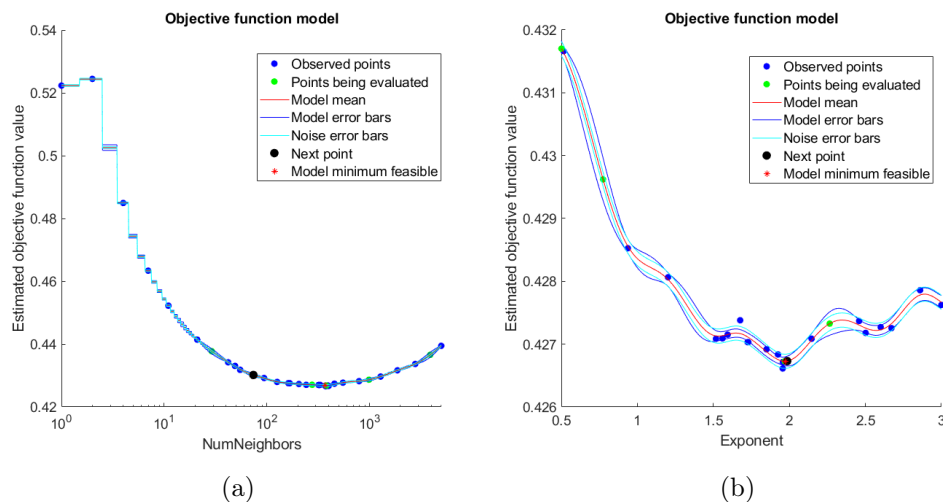


Figure 3.18: a) plot of the cross-validation error as a function of K , which is swept from 1 to 5000; the metric is fixed to Euclidean. b) plot of the cross-validation error as a function of p , which is varied from 0.5 to 3; the metric is fixed to Minkowski and the K value to 371.

results. It is defined as:

$$\left(\sum_{i=1}^n |x_i - y_i|^p \right)^{\frac{1}{p}}$$

and for $p = 1$ corresponds to the Manhattan distance, while for $p = 2$ to the Euclidean one.

The exponent p cannot be trained, but can only be defined prior to the learning process, therefore it acts as an hyperparameter and thus can be optimized. The plot resulting from the optimization process, by keeping fixed $K = 371$, is shown in figure 3.18(b).

From this plot, it can be derived that the value of p that leads to the lowest cross-validation error is $p=1.971$. Recalling that the case $p = 2$ corresponds to the Euclidean metric, this result confirms that the best metric to use, for this training set in the GAMMA system, is the Euclidean one.

Therefore, in the end, it was find out that the best classifier is char-

acterized by Euclidean distance as metric and $K = 371$. Adopting this classifier for the reconstruction of the X coordinate of events belonging to the GAMMA collimated irradiations training dataset, employing as before an 8-fold cross-validation technique, an overall validation accuracy of 57.1% is obtained. The corresponding confusion matrix is shown in figure 3.19(a), while in 3.19(b) are reported the histograms of the reconstructed position for events belonging to the validation subset.

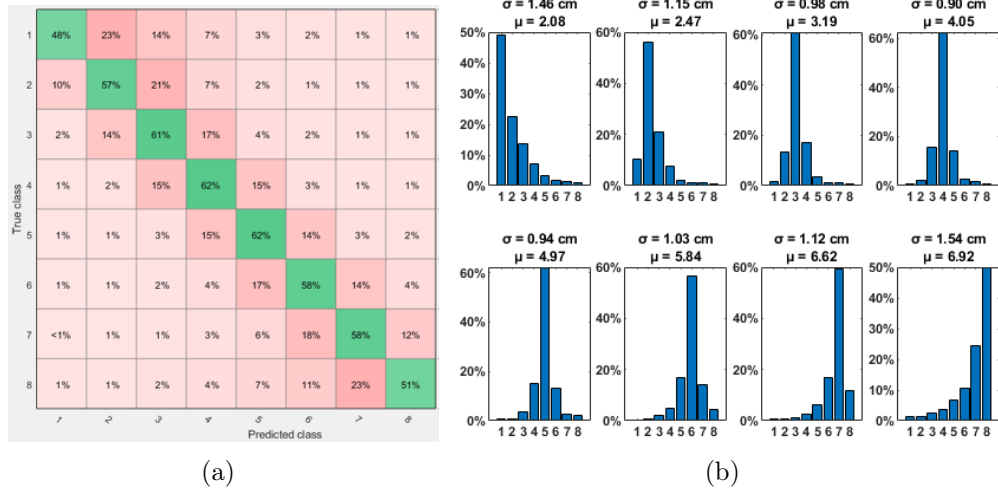


Figure 3.19: Results of the X coordinate reconstruction adopting the K-NN method with optimized hyperparameters: Euclidean metric and $K = 371$. a) confusion matrix of the cross-validated training data. b) histograms of the reconstructed position of events from the validation dataset.

From the analysis and the comparison of the confusion matrices of the classifier in the two cases $K=100$ and $K=371$, an important consideration can be made: to have identified the hyperparameters setting leading to a minimum of the cross-validation error, does not mean that all the classes perform better. Indeed, it can be noticed that the optimized classifier is characterized by a slight improvement of the reconstruction for all the central positions, however the two most external classes show an opposite behaviour, so a worsening in terms of accuracy.

K-NN application for XY coordinates reconstruction in GAMMA system

The K-NN reconstruction approach has been used also on the spectroscopy readout configuration, to test the system ability to contemporary reconstruct the X and Y coordinates of interaction of a γ -photon.

Recalling that, as illustrated in figure 3.5(b), with this pixel configuration, the collimated irradiations of the calibration phase are distributed as two rows of 4 spots each, the same considerations of the X coordinate reconstruction case can be done also in this circumstance.

As seen in the previous section, to improve the classifier performance, an optimization of the hyperparameters values can be carried out. The results of the optimization are shown in figure 3.20.

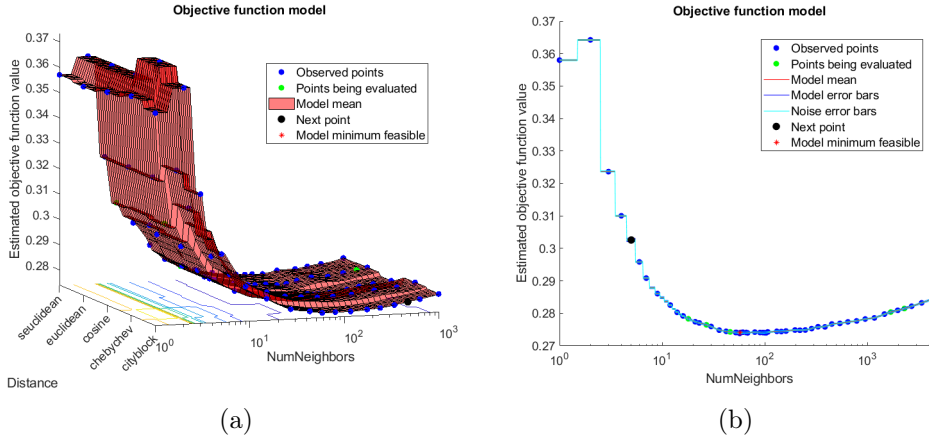


Figure 3.20: *K-NN hyperparameters optimization results for the XY coordinates reconstruction: a) cross-validated error as a function of five different metrics and of K , which is swept from 1 to 1000. b) cross-validated error, employing the Cosine metric, as a function of K , which is swept from 1 to 5000.*

From 3.20(a), it can be observed that, as in the X coordinate reconstruction case, a minimum of the error value is found around a specific range of K , in this case $K \approx 100$. The metric giving the lowest misclassification error is the Cosine distance, defined as $1 - \cos \theta$, where θ is the angle between observations. Therefore, fixing the metric as Cosine, the optimum value of K is found to be $K = 104$, as shown in figure 3.20(b).

Adopting the classifier with the optimized hyperparameters (Cosine distance as metric and $K = 104$) to reconstruct the XY coordinate of events belonging to the GAMMA collimated irradiations training dataset, employing the 8-fold cross-validation technique, an overall validation accuracy of 72.6% is obtained. The corresponding confusion matrix is shown in figure 3.21(a) on the next page, while in 3.21(b) are reported the histograms of the reconstructed position from predictions on the validation dataset.

Two observations can be made from the analysis of the plots. The first one is that, while in the imaging readout configuration, the minimization of the cross-validation error comes with a worsening of the classification performance of the external classes, adopting the spectroscopy readout configuration, by comparing the confusion matrices of an optimized classifier and of a non-optimized one, an improvement of the performances for all the classes is observed.

Moreover, it can be noticed that, with respect to the X coordinate reconstruction case, in the XY reconstruction system the overall validation accuracy is much higher. As already discussed in section 3.2.4, this is due to the fact that, in the spectroscopy readout configuration, the spots irradiated during the calibration phase are placed further apart one from another, therefore their signal distribution have less similarities between them, and the different classes are easier to distinguish.

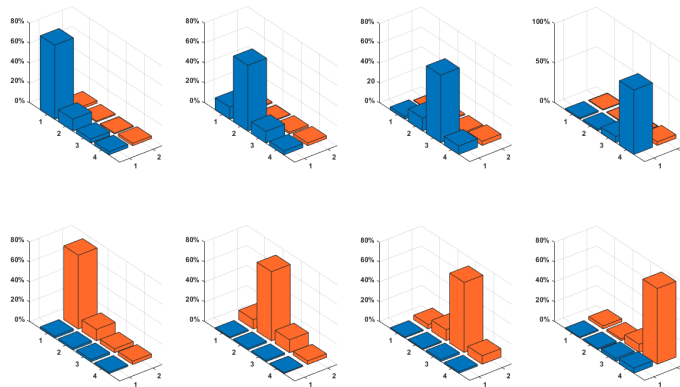
K-NN application for side irradiation reconstruction in GAMMA system

The reconstruction ability of the analysed algorithms can be further validated by trying to reconstruct the X position of the events belonging to an irradiation from the side of the crystal, at a height of ≈ 1 cm, as shown in figure 3.22 on page 105. In this way the classification capabilities of the algorithms are tested for γ -rays coming from a different direction with respect to the irradiations performed during the calibration phase.

It must be highlighted that the real X coordinate of the events is not



(a)



(b)

Figure 3.21: Results of the XY coordinates reconstruction adopting the K -NN method with optimized hyperparameters: Cosine metric and $K = 104$. a) confusion matrix of the cross-validated training data. b) histograms of the reconstructed position of events from the validation dataset.

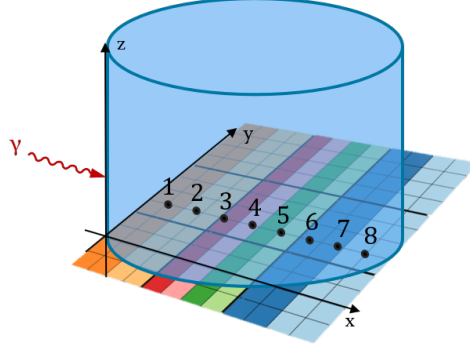


Figure 3.22: Schematic representation of the SiPMs merging configuration coupled with the scintillator crystal. In red is shown the γ -ray irradiation from the side of the crystal.

known, however the goodness of the reconstruction can still be proved by verifying that the reconstructed events are distributed according to the Lambert-Beer law: $N = N_0 e^{-\mu x}$. In order to use this law, the value of the linear attenuation coefficient μ is needed and can be calculated from:

$$\mu = \mu' \cdot \rho = 7.583 \cdot 10^{-2} \text{cm/g} \cdot 5.08 \text{g/cm}^3 = 0.3852 \text{cm}^{-1}$$

where μ' is the mass attenuation coefficient of the $\text{LaBr}_3(\text{Ce}^{3+})$ at 662 keV and ρ is the density of the material.

Thus, the number N_i of the events that have not being absorbed yet up to the i class, can be calculated. For example, for the first and the fourth classes the computation leads to:

$$N_1 = N_0 e^{-\mu x_1} = 10093 \cdot e^{-0.3852 \cdot 1} = 6866$$

and

$$N_4 = N_0 e^{-\mu x_4} = 10093 \cdot e^{-0.3852 \cdot 4} = 2162$$

From these results, the percentage of events absorbed before the i class can be derived. For instance, up to the first class, 32% of events are absorbed, while up to the fourth one, their percentage increases to 78.6%. These results are in line with the values provided by Saint-Gobain, which can be inferred from the plot in figure 3.23 on the next page [52]. Eventually the

percentage of events absorbed in the i class can be computed: 32% in the first class and 10.1% in the fourth one.

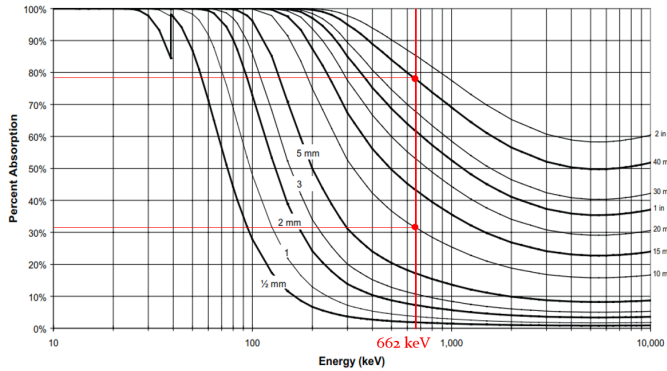


Figure 3.23: Absorption efficiency of BrillanCe TM380 ($\text{LaBr}_3(\text{Ce})$). The intercept of the red vertical line with one of the curves determine the percentage of events absorbed up to a specific crystal depth.

Once the theoretical absorption percentages are calculated for all the classes, the classification results, employing the K-NN algorithm can be analysed. In figure 3.24 are reported the histograms of the reconstructed X coordinates, for the events belonging to the side irradiation, adopting classifiers with different K value.

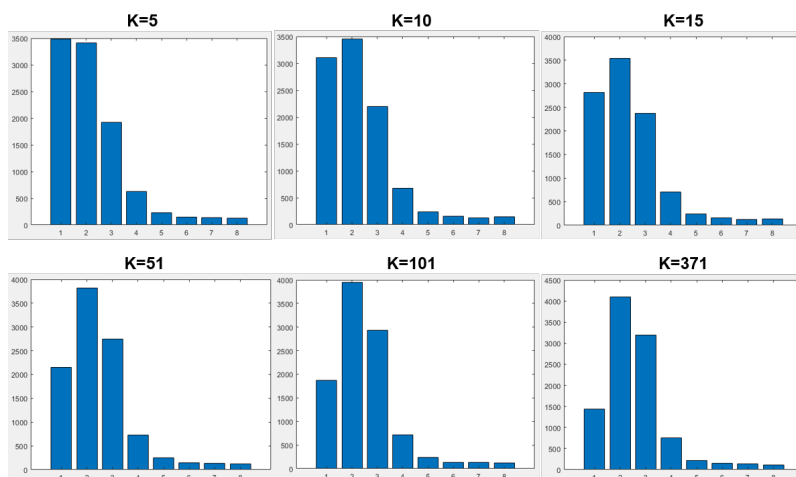


Figure 3.24: Histograms of the reconstructed X coordinates using the K-NN method with Euclidean metric. Each histogram corresponds to the use of a different value of K.

According to the Lambert-Beer law, the distribution of the number of events absorbed along the X axis has an exponential decay behaviour; therefore it is expected that the majority of the events are reconstructed in the first class, a smaller amount in the second class and so on.

From figure 3.24, it is evident that, as the value of K increases, the number of events reconstructed in the first class decreases incorrectly: this behaviour can be explained recalling that, increasing K , up to the optimum value of 371, the overall system accuracy improves, however the accuracy of the first class worsens. Therefore, considering that this class is the one containing the highest number of events, if its classification performance worsens the quality of the reconstruction is heavily degraded.

The best reconstruction results for the side irradiation events was obtained by choosing the Euclidean metric, $K = 5$ and employing the Principal Component Analysis (PCA) technique, which will be illustrated in the next section.

In figure 3.25 the comparison between the distribution of the reconstructed and the theoretical X coordinates of the side irradiation events, is reported. This proves the ability of the system to reconstruct also events belonging to γ -ray irradiations with direction different with respect to the calibration irradiations one.

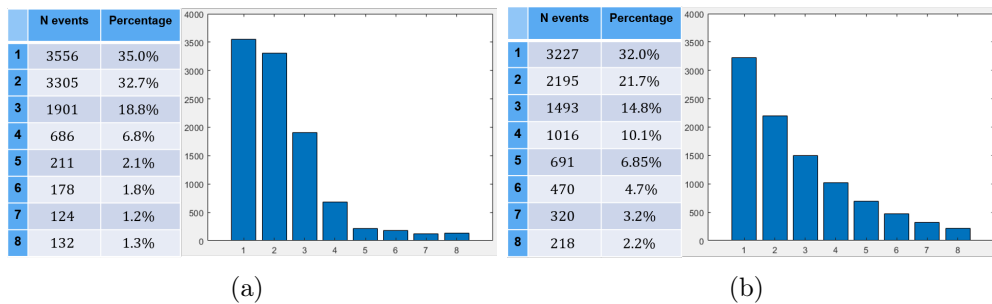


Figure 3.25: Histograms of the distribution of the events, belonging to an irradiation from the side of the crystal, along the X axis. The tables show the number and the percentage of the events in each class. a) Events reconstructed using the K -NN method with Euclidean metric, $k = 5$ and PCA explaining 90% of the variance (only the first five components of the problem are considered). b) Theoretical distribution, according to the Lambert-Beer law.

3.3.3 Principal Component Analysis

In section 3.3.1 it was illustrated that events belonging to different classes seem to never be easily distinguishable in the features space. In order to try to find a way to separate more clearly these events, the Principal Component Analysis (PCA) can be exploited.

The basic idea of the PCA is to find a new reference system starting from the *principal component*, that is a new axis, oriented in a specific direction, along which the variance of the data is maximized.

The principal component identifies the axis where the data are best separated: since in the classification task the interest is in the ability to distinguish different data from each other, this axis has a higher information content with respect to the axis of the original reference system (figure 3.26).

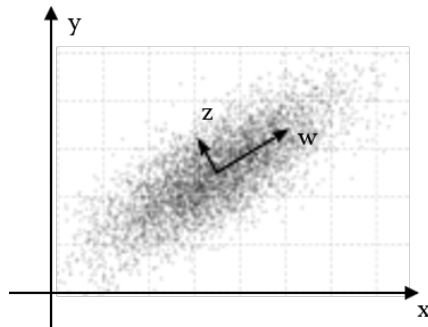


Figure 3.26: Example of a 2-dimensional data distribution characterized by a higher variance along the new axis W , with respect to the original reference axis Z .

All the axes of the new reference system can be mathematically computed as the eigenvectors of the matrix of covariances of the normalized dataset. The number of eigenvectors is equal to the number of dimensions of the original dataset and each eigenvector is orthogonal to the others.

More specifically, the original dataset is mapped in the new reference system by performing the following steps:

1. Subtract the mean from each of the data dimensions
2. Calculate the covariance matrix

3. Calculate the eigenvectors and eigenvalues of the covariance matrix
4. Order the eigenvectors according to their eigenvalue, from the highest to the lowest, to get the components in order of significance and possibly select only the most significant ones
5. Derive the new dataset as:

$$NewDataset = EigenvectorsMatrix \times DataMeanAdjusted$$

Another interesting characteristic of the PCA is that, other than allowing to watch the data from a richer of informations perspective, it can also be exploited to reduce the number of dimensions of the problem: indeed, even considering only some of the components and discarding the others, a good part of the original variance (information) of the data can be maintained. Usually only the first n components are taken into account so that 90% of the original variance is reached. This allows to discard the redundant dimensions with little informations and to remarkably simplify the problem.

It is important to emphasize that the axis characterized by the maximum variance of the data does not necessarily correspond to the best axis to classify the events.

To illustrate this concept, in figure 3.27 on the next page an example of a 2-dimensional data distribution is shown. It is evident that the principal component W , along which the data are more distributed, is not the best axis to distinguish the events of the two classes. On the contrary, the Z axis, even if bringing less informations in terms of variance, is more useful to separate the two classes.

By applying the PCA to the training data of the GAMMA system adopting the imaging readout configuration, and stopping at the description of 90% of the original variance, only 5 components are employed, with variance respectively of: 54.8%, 17.3%, 10.3%, 6.4%, 5.4%. Therefore, out of the original 8 components, 3 can be discarded and the problem is simplified to a 5-dimensional one.

In figure 3.28 on the following page are shown various scatter plots,

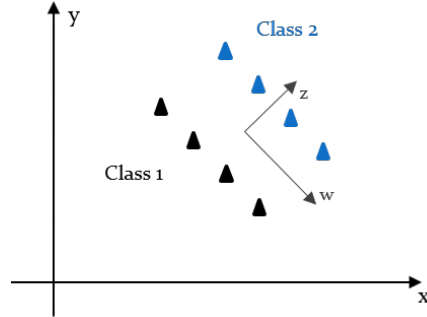


Figure 3.27: Example of a 2-dimensional data distribution where the direction of maximum variance of the data does not correspond to the best direction to distinguish the class of the events.

of the GAMMA training data, obtained by changing, as X and Y axis, different pairs among the 5 components.

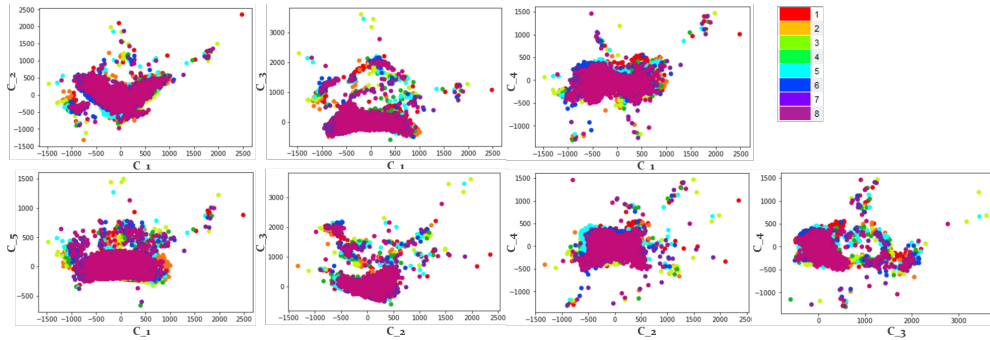


Figure 3.28: Training data scatter plots. Each plot presents, as X and Y axis, a different pair of components. Considering a specific plot, every dot represents an event, while the different colors represent the 8 different classes, according to the key at the top right.

From the figure it is noticeable that, even adopting the PCA, components that clearly allow to distinguish classes one from another cannot be identified.

3.3.4 Decision tree reconstruction method

For the position reconstruction of γ -rays absorption events, the decision tree ML method was tested. In order to understand the basic working

principle of the decision tree algorithm, it is easier to assume, at first, that the tree is already built, so that the procedure according to which new events are classified can be investigated. The process on the basis of which the tree is grown will be illustrated afterwards.

In figure 3.29 is represented an example of a fictitious decision tree. The tree is drawn upside down so the first element to be considered is the root node at the top, which is characterized by a condition on one feature and a binary split: depending on which condition is satisfied by the current event, one of the two branches is chosen and the corresponding subsequent node is reached. At this node another split condition, leading to two further possible paths, is present. According to this principle, the tree is climbed down until, eventually, the final node, called leaf, which is labeled with a class name, is reached. In the end the event is assigned to the class of the found leaf.

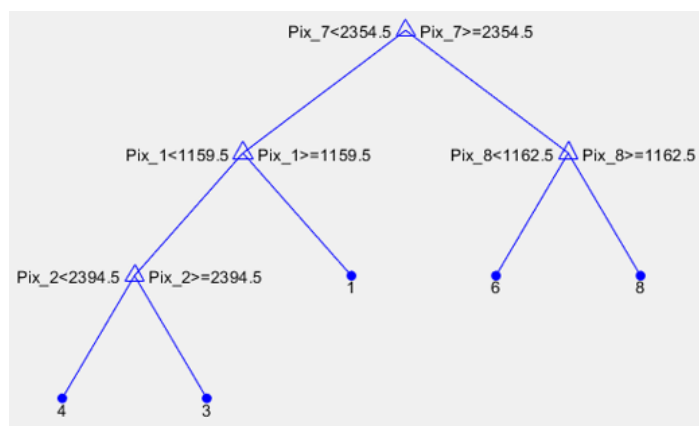


Figure 3.29: *Example of a decision tree.*

To grow the tree, two properties have to be selected: the depth of the tree, determined by the maximum number of splits or by the minimum number of samples per leaf node, and the splitting criterion, according to which the conditions on the splitting nodes are decided.

To obtain the splitting condition of a node, one way to proceed is by looking at the entropy function. Indeed, as the tree is climbed down, from the top towards the bottom, the objective is to reduce the uncertainty, or entropy, on the possible class to which the datapoint belongs.

The entropy function is defined as:

$$H(X) = -p_1 \log_2 p_1 - p_2 \log_2 p_2 - \dots - p_m \log_2 p_m = \sum_{j=1}^m p_j \log_2 p_j$$

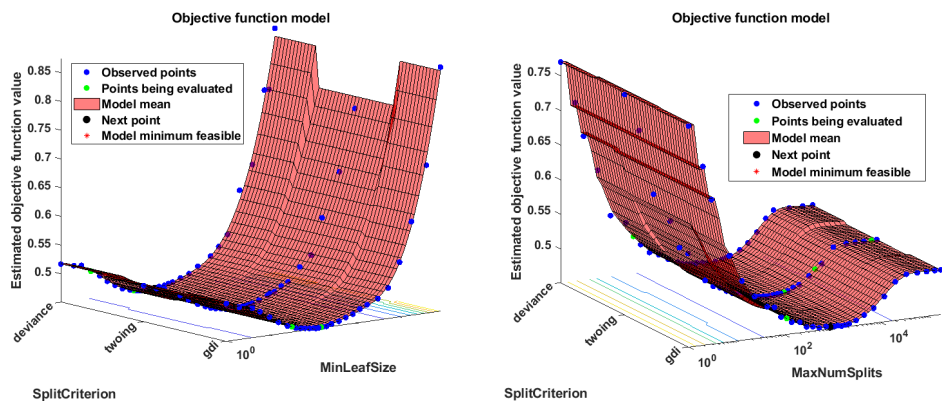
Every time there is a condition, the dataset is split in two parts and the uncertainty is reduced. The difference between the entropy before and after the condition, also called information gain, can be computed for all features, for many values of each feature. Eventually the feature and its relative value giving the higher information gain are picked.

As in the case of the K-NN, also for classification trees there are hyperparameters that can be optimized. These are:

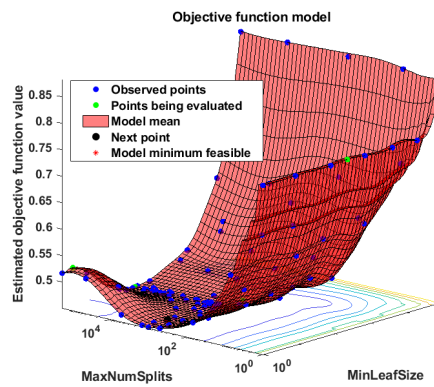
- Split Criterion: which can be chosen among the Gini Diversity Index, the Twoing Rule and the Maximum Deviance Reduction; each criterion uses a different cost function to decide the feature condition for each node;
- Minimum Leaf Size: which corresponds to the minimum number of samples per leaf node;
- Maximum Number of Splits: that has to be accurately chosen considering that a leafy tree tends to overtrain and to have a validation accuracy much lower than its training accuracy.

In figure 3.30 on the facing page are reported the results of the optimization of the three hyperparameters: since the only way to obtain a graphical representation is to optimize two parameters at a time, three different plots are obtained.

As in the K-NN case, also in these plots a minimum of the cross-validation error as a function of the hyperparameters is present. This is explained considering that: if the tree is too simple, the trained model is not able to apprehend the relevant relations between features and classes, so the classification performance is not satisfactory. By increasing the number of nodes and leaves of the tree, the model becomes more complex, therefore the informations contained in the training dataset are well exploited and the misclassification error decreases. However, if the tree



(a) Split criterion - Minimum leaf size (b) Split criterion - Maximum number of splits



(c) Maximum number of splits - Minimum leaf size

Figure 3.30: Decision tree hyperparameters optimization results. The Z axis shows the cross-validation loss, which is the parameter that has to be minimized. For each plot on the X and Y axis is reported a different pair of hyperparameters.

becomes too elaborated, overfitting occurs, so the model loses the ability to generalize on new data and the classification error on validation data starts to rise.

Overall it is inferred that the optimum classifier, for the GAMMA system employing the imaging readout configuration, is characterized by Maximum Deviance Reduction as split criterion, minimum leaf size equal to 100 and maximum number of splits equal to 1156.

Adopting this optimized classifier for the X coordinate reconstruction of γ -rays absorption events, an overall validation accuracy of 54.9% is obtained. In figure 3.31(a), the confusion matrix, derived by 8-fold cross-validated predictions on the training dataset, is reported.

Furthermore, in figure 3.31(b) the histograms showing the distribution of probability of the reconstructed events along the X axis, obtained employing the optimized classifier on the validation data, are illustrated.

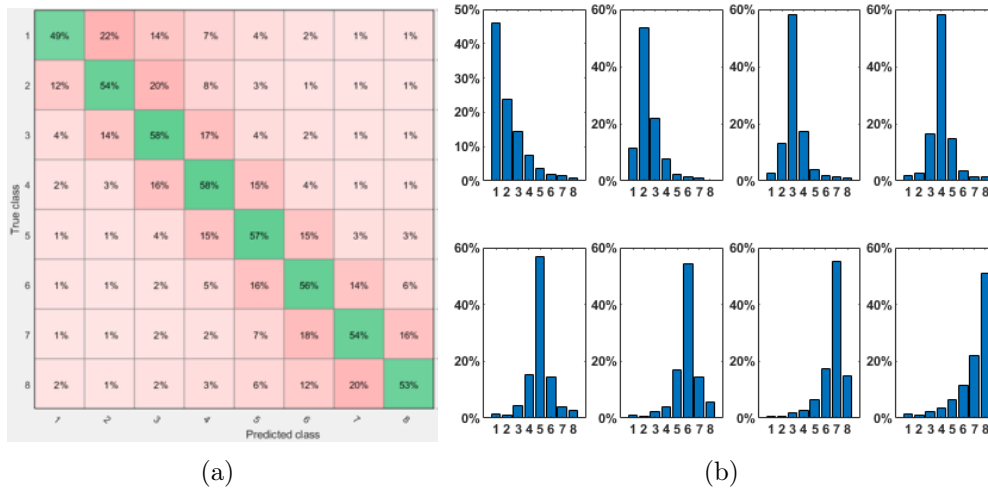


Figure 3.31: Results of the X coordinate reconstruction adopting the decision tree method with optimized hyperparameters: Maximum Deviance Reduction as split criterion, minimum leaf size equal to 100 and maximum number of splits equal to 1156. a) confusion matrix of the cross-validated training data. b) histograms of the reconstructed position of events from the validation dataset.

As regards the spectroscopy readout configuration, it is found that the optimized hyperparameters are: Twoing Rule as split criterion, minimum

leaf size equal to 47 and maximum number of splits equal to 1157.

The optimized classifier is characterized by an overall validation accuracy of 69.8%. The corresponding confusion matrix of the cross-validated training data and the histograms of the reconstructed position of events from the validation dataset are shown in figure 3.32 on the next page.

In summary, from the comparison of the results obtained by using the K-NN and the decision tree classification methods, it is derived that the two reconstruction algorithms have similar performances in terms of validation accuracy and they both show a worsening of the first class accuracy while the other classes improve.

The decision tree method is characterized by a slightly lower overall accuracy, however it is faster and much more simple: indeed, once the tree is built, the method has just to solve simple inequalities to perform the classification of new events.

Thanks to its ease of implementation, low memory occupation and high operation velocity, considering that also the PCA can be exploited to further simplify the problem, the decision tree algorithm can be employed in innovative contexts as the embedded machine learning, which will be addressed in chapter 4.

3.3.5 Final considerations

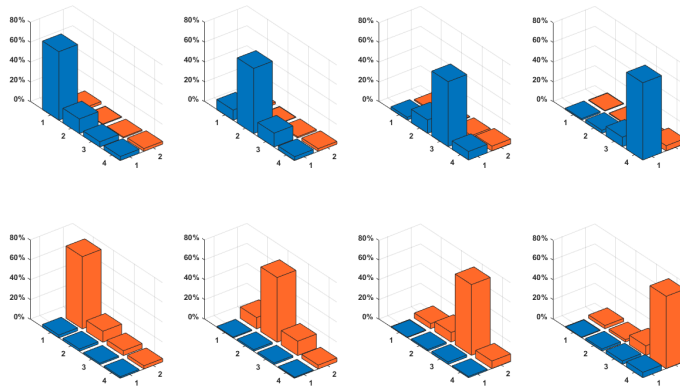
For the reconstruction task another ML algorithm, called Support Vector Machine (SVM), was tested. This method works by finding the hyperplanes, in the n-dimensional features space, that best separates the elements of one class from those of the other classes.

After the optimization of the hyperparameters, the classifier provided a validation accuracy of 57.9%, slightly higher with respect to the one obtained with the K-NN and the decision tree methods. However, this algorithm is much slower compared to the other ML methods, so, since the improvement it brings, in terms of classification accuracy, is very limited, it is not worth to employ it.

Another alternative approach, that was not implemented in this the-

1	71%	13%	5%	4%	2%	1%	1%	3%	
2	12%	62%	15%	4%	2%	1%	2%	3%	
3	4%	12%	66%	10%	1%	1%	2%	4%	
4	2%	3%	11%	77%	1%	<1%	1%	5%	
5	2%	2%	1%	1%	73%	11%	5%	4%	
6	1%	2%	2%	1%	12%	66%	13%	4%	
7	1%	2%	2%	1%	4%	12%	68%	9%	
8	1%	2%	4%	6%	3%	2%	9%	74%	
		1	2	3	4	5	6	7	8
		Predicted class							

(a)



(b)

Figure 3.32: Results of the XY coordinates reconstruction adopting the decision tree method with optimized hyperparameters: Twoing Rule as split criterion, minimum leaf size equal to 47 and maximum number of splits equal to 1157. a) confusion matrix of the cross-validated training data. b) histograms of the reconstructed position of events from the validation dataset.

sis work, but that could be used for the position reconstruction task, is the ensemble classification algorithm. The idea is to train many simple learners, such as decision trees and K-NN classifiers, to then combine their results and obtain a single output. In this way a better classification accuracy than the one characterizing any of the single constituent algorithms is achieved.

The combination of the outputs of the base classifiers can be done in two different ways:

- The learners can be trained in parallel and then the overall output is found through a majority vote system: this approach allows to decrease the variance of the system (error from sensitivity to small fluctuations in the training set);
- The learners can be trained in series, using the output of a classifier as the input of the subsequent one: this approach allows to decrease the bias of the system (error from erroneous assumptions in the learning algorithm).

As a final consideration it should be emphasized that all the tested reconstruction ML algorithms gave similar results in terms of classification accuracy. This could be due to the fact that a physical limit, for what regards the ability to distinguish scintillation events in different positions, is reached for the proposed SiPMs merging configurations.

Probably, by adopting different readout configurations characterized by more than just 8 pixels, as in the final GAMMA system, where 144 output channels will be available, the reconstruction capabilities of the system will be much higher.

Chapter 4

Embedded Machine Learning

In this chapter is presented an innovative system constituted by a microcontroller-based gamma spectrometer that is capable to reconstruct the direction of the interacting gamma photons and at the same time to move the position reconstruction algorithm computations from the central node to the peripheral ones, adopting embedded machine learning reconstruction directly in the external nodes of the system. In the first part of the chapter the architecture of the system is explained, then a description of the embedded reconstruction algorithm is carried out and eventually the experimental results obtained with a prototype are illustrated.

4.1 Introduction

The availability of computationally efficient Machine Learning (ML) algorithms, combined with constantly-evolving and easily-configurable digital platforms, such as FPGAs and micro-controllers (μC), can push the state-of-the-art performances of modern embedded systems towards better results using novel architectures with multiple nodes and distributed computational centers.

In chapter 3, the use of Machine Learning techniques was presented with the objective of reconstructing the position of interaction of a γ -ray inside the scintillator crystal of the gamma detector. In this chapter, a

different application of the ML classifications methods will be illustrated: the idea is to implement a portable unit which enables the angular localization of gamma sources as a function of the reconstructed interaction point distribution, by employing a solid state detectors based unit for γ -ray detection able to perform embedded ML reconstruction.

The novelty of the introduced system is that the reconstruction task is not performed in a post-processing phase, but is directly executed in the micro-controller of the acquisition node in real time: this allows for relaxation of constraints in data transmission and, in case of cooperative networks, distribution of computational complexity, posing interesting challenges and the need for new architecture paradigms.

In figure 4.1 on the facing page a schematic representation of the system working principle is shown: the spectrometer is illustrated in the middle of the figure, together with the radioactive source moving around it. The detector absorbs the emitted γ -photons and, thanks to the embedded ML reconstruction, is able to infer the direction of the incoming γ -rays.

In particular, the reconstruction is made possible thanks to a preliminary training of the system node using a dataset where the incoming radiation is distributed along the 2π angle around the crystal on the detectors plane. Therefore the gamma source is localized and the system transmits to the MATLAB environment the data corresponding to the reconstructed source position.

In this way it is possible to build a large dynamic range gamma spectrometer that is capable of recognizing the direction of the incoming gamma radiation, for isotropic sources, if the absorption length of gamma photons in the crystal at the energy range of interest is sufficiently short.

For the gamma detection task, the system shown in figure 4.2 on page 122 has been employed. It is the same detection system that has been used for the experimental measurements of chapter 3 and is constituted by: the $\text{LaBr}_3(\text{Ce}^{3+})$ scintillator crystal coupled with the SiPMs array matrix, the ASIC for the conversion of the current signal, produced by the scintillation light due to the γ -photons absorption, and the LAILA DAQ board, which digitizes the analog signal to build the energy spectrum

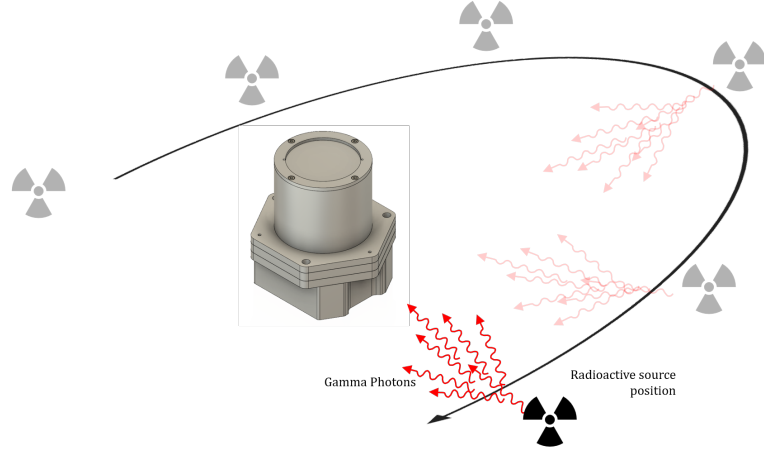


Figure 4.1: *Schematic illustration of the system application: the radioactive source, emitting γ -rays, moves around the spectrometer, which detects the γ -photons and performs ML reconstruction of the source position directly in the micro-controller.*

and perform the embedded ML reconstruction.

However, while in chapter 3 the system was employed for imaging and spectroscopic applications in nuclear physics experiments, aiming at the correction of the relativistic Doppler broadening effect, this project could find an application in other types of nuclear physics experiments, and in the fields of environmental monitoring and nuclear safety. Moreover, a set of directional gamma detectors could be embedded in cooperative mobile land or aerial units and exploited for radiation levels monitoring and mapping.

4.2 System Architecture

The prototype used as a test bench of the distributed ML architecture is a gamma spectrometer based on a thick, $\varnothing 3'' \times 3''$ lanthanum bromide ($\text{LaBr}_3(\text{Ce}^{3+})$) crystal coupled to a 144 NUV- HD SiPM array [53]. The scintillation crystal ensures high conversion efficiency (63 ph/keV), fast crystal response (16 ns decay time) [26] and a state-of-the-art energy resolution of 2.6% at the ^{137}Cs photopeak emission energy of 662 keV [54].

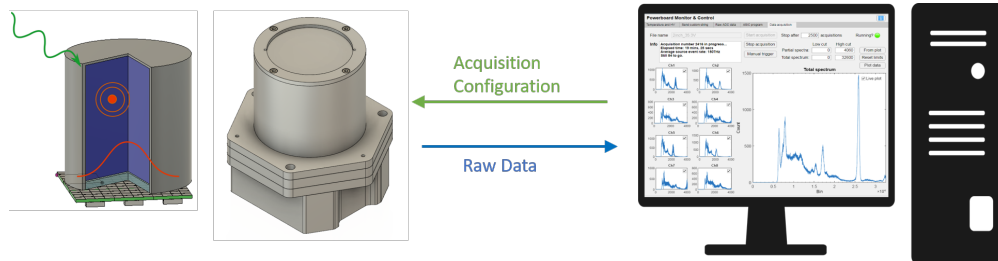


Figure 4.2: When a gamma photon interacts with the indirect conversion spectroscopy module, a number of optical photons proportional to the boson energy are generated into the crystal. The light pulse generates a current signal that is converted by the ASIC and digitalized in LAILA module to build a spectrum. The custom GUI allows to change the acquisition settings for calibration procedure and best performance.

Being the absorption length smaller than 20mm up to about 500 keV, the gamma photon sources most probable direction at these energies can be computed as a function of the reconstructed interaction point occurrence.

Each SiPM detector has a cell pitch of $30\mu\text{m}$ and an overall dimension of $6.4\text{mm}\times 6.4\text{mm}$. The reduced delayed-correlated noise in NUV-HD SiPMs, obtained thanks to short lifetime of the carriers in the substrate, allows to operate the system at ambient temperature without compromising the energy resolution.

The photograph of the prototype front-end is reported in figure 4.3 on the facing page. Scaling down costs and sizes of each node of the network is a crucial task when the number of nodes increases, therefore the front-end is composed of a compact, cost-effective LAILA board [55]. This board is made up of a GAMMA ASIC [17] whose output voltage is sampled by an ARM-Cortex M4 based STM32 μC via its embedded ADC. The SPI programming of the chip and the UART communication of the raw data are also operated by the μC .

The ASIC has the task of converting the current signal coming from the SiPM matrix. It is constituted by a low-impedance input stage that conveys the current signal into a self-triggered gated integrator filter ($3\mu\text{A}\div 34\text{mA}$ input current dynamic range). Two selectable additional capacitors are in-

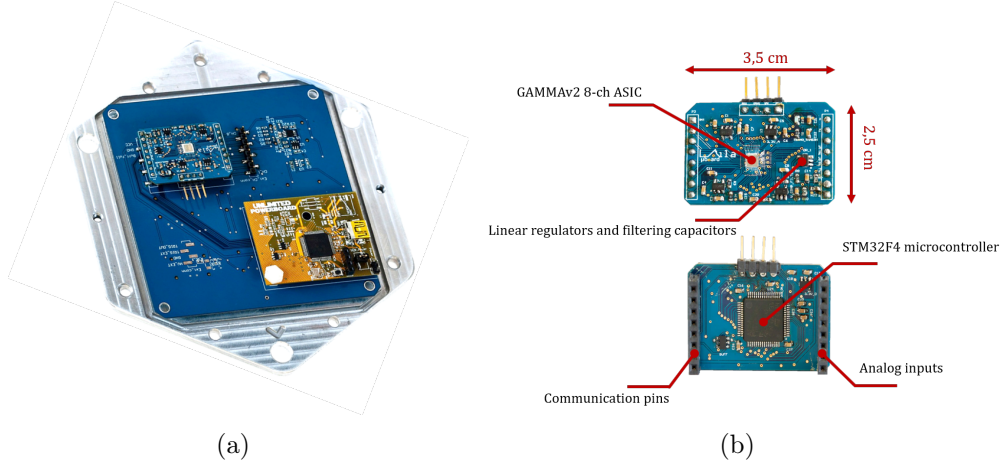


Figure 4.3: *a) Photograph of the system. The LAILA (blue) and Powerboard (yellow) PCBs are visible. The 144 SiPM detectors array is mounted on the back and optically coupled to a $\text{LaBr}_3(\text{Ce}^{3+})$. b) Photograph of the compact LAILA board ($3.5\text{cm} \times 2.5\text{cm}$) with the bottom plane hosting the microcontroller and the top one hosting the GAMMA ASIC.*

roduced to boost the gain of the filter at low energies.

The positive-feedback input stage allows to keep a large phase margin and signal bandwidth even connecting a large capacitive load (associated to SiPM cells) to the input node [17].

The trigger circuit is fed in parallel to the integrator stage and is composed of a trans-impedance stage and a high-pass filter. The chip has been realized in AMS $0.35\mu\text{m}$ CMOS process and has a total area of $2.9 \times 3.1 \text{ mm}^2$. The voltage outputs of the ASIC are multiplexed to the STM32 and converted by its 12 bit, SAR internal ADC.

In figure 4.4 on the next page the block scheme of the LAILA-based gamma spectrometer is shown. The GAMMA ASIC includes a novel Amplitude Gain Control (AGC) circuit, that allows for a dynamic modulation of the gain as a function of the coarse input signal amplitude while keeping a linear transfer function, an important instrumentation requirement for accurate energy calibration in spectroscopy applications. The AGC works in this way: if the filter output signal overcomes a voltage threshold within a fixed time from the start of the integration, the gain is reduced

by adding capacitances in parallel to the original feedback capacitance in the integration stage, in order to increase its value. The final coarse gain values are then provided at the output, for each event, as digital bits.

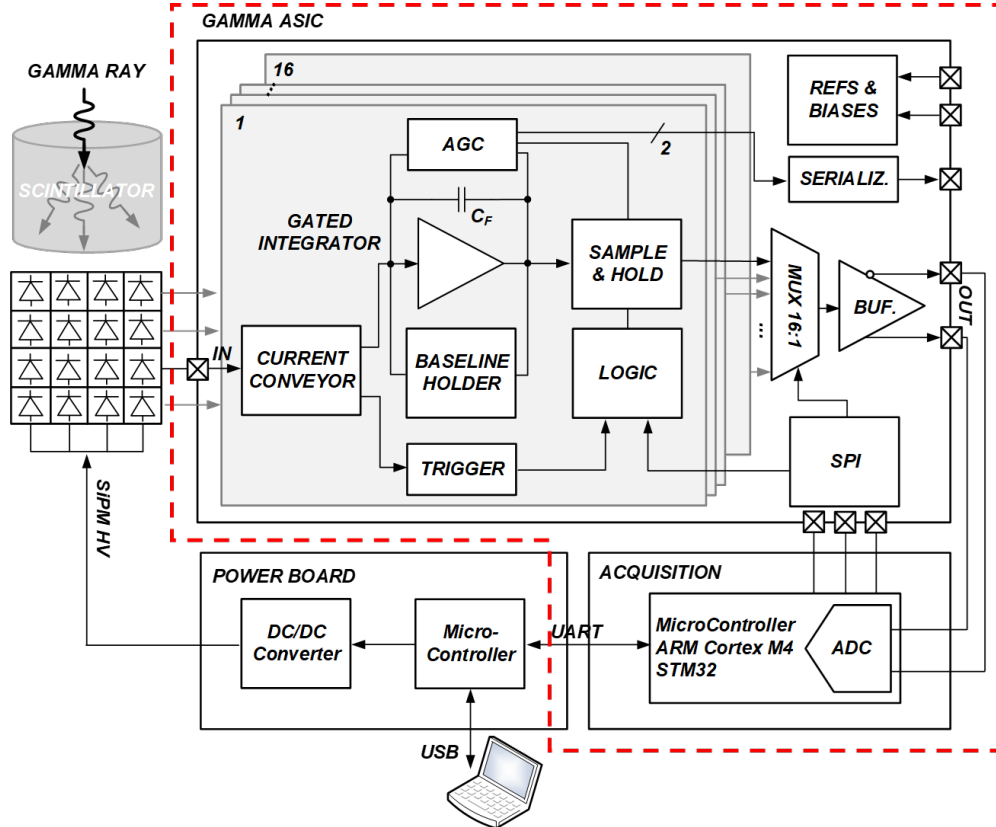


Figure 4.4: Architecture of the prototype based on LAILA module (enclosed in the dashed line) for readout of SiPM currents pulses with peak amplitudes spanning from $3\mu A$ to $30mA$.

Due to temperature fluctuations the gain of the SiPM detectors drifts. This phenomenon is particularly detrimental for the position reconstruction task since the training data, which are acquired during the calibration phase, and the test data, which are acquired during the test phase and belong to the γ irradiations whose source direction is wanted to be localized, are performed in different time periods and experimental conditions. Therefore, as the temperature in the two acquisitions is not the same and since it evolves differently throughout the two measurements, the two datasets will be acquired with a different gain of the SiPMs. This

introduces an uncorrelated noise in the datasets, that is not easy to be distinguished and then removed, which makes it harder for the ML model to generalize the relations between features and output classes, established during the training phase, to new data, leading to errors in the classification.

To compensate these gain drifts, the Powerboard, a custom PCB designed for detector polarization and USB communication with MATLAB environment, is used: it acquires the detectors temperature and then adjusts the bias voltage in closed loop.

The module is powered and operated via the USB connection. A custom GUI allows for GAMMA ASIC setting optimization and data acquisition.

4.3 Embedded reconstruction algorithm

The goal of the experiment is to build a micro-controlled based gamma spectrometer that is capable to reconstruct the direction of the interacting gamma photons and at the same time to move the position reconstruction algorithm computations from the central to the peripheral node of the system.

To fulfill the first requirement of the experiment, that is the ability to localize the direction of the impinging γ -rays, a ML reconstruction algorithm can be employed, following the same principles seen in section 3.3 for the position of interaction reconstruction. Even if the same ML algorithms can be employed in both circumstances, there are a few differences between the two reconstruction tasks: indeed, while in the first case the objective is the reconstruction of the position of absorption of the γ -photon inside the scintillator crystal, in this case the goal is to reconstruct the direction from which the γ -photon is emitted.

Since the pixel configuration is the same in the two problems, the features are identical. The distinction lies in the modalities of acquisition of the training dataset, which means that the output classes are different: in the position of scintillation reconstruction problem the calibration

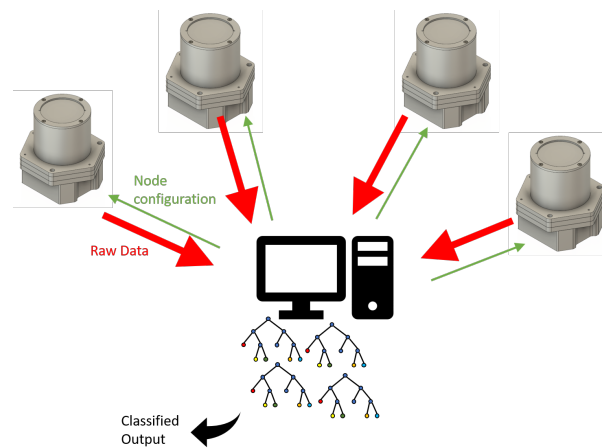
phase is performed by scanning the crystal surface from the bottom side by means of a ^{137}Cs collimated source; instead in the source localization problem, the gamma source is moved in determined positions along the 2π angle around the crystal on the detectors plane (as shown in figure 4.1) to obtain a training dataset where each class corresponds to an angle between the spectrometer reference system and the gamma source. The training dataset is then used in the ML algorithm to associate each event of new datasets to the correct class, so to the correct direction.

It should be reminded that, in order to be able to recognize the direction of the incoming γ radiation, for isotropic sources, the absorption length of gamma photons in the crystal at the energy range of interest has to be sufficiently short. Otherwise γ -photons would be absorbed not only in the first half of the scintillator crystal but also in the second half, making impossible to understand whether the incoming γ -ray direction is from one side or the other.

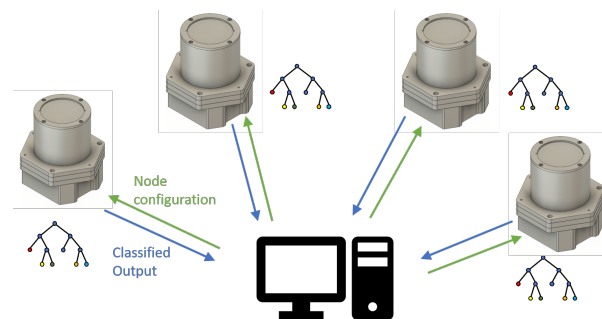
The second requirement that has to be satisfied, is the possibility to move the direction reconstruction algorithm computations from the central to the peripheral nodes of the system.

If the target application involves embedding the system in mobile units, the relocation of the reconstruction algorithm computations brings different advantages. Indeed, in real time operations, if the classification algorithm is entirely executed in the central node, the bottle-neck of the system, in terms of maximum count rate, is given from the data reception and processing speed of the same node. Instead by running the classification algorithm independently in the peripheral nodes, the constraints on communication speed are relaxed. Moreover each node is allowed to independently train, change the algorithm hyperparameters and adjust its position and orientation in space, when mounted on mobile units, to optimize the detection procedure of the cooperative, ML-based dynamic network. These concepts are illustrated in figure 4.5 on the facing page.

In order to be able to execute the ML reconstruction embedded in the micro-controller, not all the ML algorithms can be employed. As an example it can be considered that, even applying the Principal Component



(a) Computation in the central node



(b) Computation in the peripheral nodes

Figure 4.5: *a) Classification algorithm computations run in the central node: the bottle-neck of the system is given from the data reception and processing speed of this same node. b) Classification algorithm computations run in the peripheral nodes: constraints on communication speed are relaxed and each node is allowed to independently train, change the algorithm hyperparameters and adjust its position in space when mounted on mobile units.*

Analysis, to reduce the number of dimensions and so the complexity of the problem, the usage of the K-NN algorithm is prohibitive because of the training dataset dimension and the classification computational complexity. Indeed, when the K-NN algorithm is applied, for each event to be classified, the distance from all the events belonging to the training dataset has to be computed.

On the other hand, the decision tree algorithm seems more suitable for this application: once the decision tree is created and uploaded in the peripheral nodes, only a minimum amounts of data has to be stored and the classification time is short if the tree depths are kept small.

To minimize the misclassification error of the decision tree algorithm the hyperparameters optimization procedure can be performed. It should be emphasized that this operation has to be executed only one time after the calibration phase; then, once the optimum hyperparameters are found, the decision trees are built from the central node of the architecture and then uploaded on the LAILA boards, where the reconstruction is performed in real time with the acquisition.

The optimum classifier, in the case of a single peripheral node, can be easily obtained by performing the hyperparameters optimization procedure available in MATLAB, based on the Bayesian Optimization. On the other hand, the optimum hyperparameters calibration procedure in the distributed architecture and how each node setting should influence other nodes in the network is an open question.

Because the decision tree predictors correspond to digital values that are proportional to the number of photons impinging on the SiPMs detectors, each decision tree is built with a reduced training dataset that only includes events in a fixed energy interval (e.g. events closer than one FWHM from the photopeak), and is used to classify events that belong to the same energy interval.

4.4 Experimental Results

The directional gamma spectrometer has been tested using a ^{57}Co source for both the training phase and test phase. The $\varnothing 3'' \times 3''$ $\text{LaBr}_3(\text{Ce}^{3+})$ scintillation crystal was coupled to a 12×12 array of NUV-HD SiPMs and the signal charge was collected by a LAILA module front-end, whose embedded STM32 μC also operates the gamma events classification.

To read the charge signal of all SiPMs with only 8 channels, the output of the detectors was merged following the same pattern used for the post-processing XY interaction position reconstruction illustrated in chapter 3 (spectroscopy readout configuration).

It must be emphasized that one of the eight acquisition channels has been excluded from the training and the test dataset since it was faulty at the time the experimental measurement was taken. Therefore the reconstruction task is more difficult to achieve, considering that only 7 features are available instead of 8.

The source positions chosen for the training dataset acquisition are shown in figure 4.6(a) on the next page: the ^{57}Co source has been moved in 6 different locations, labeled in the figure by letters, equally spaced along the full circle in the detectors plane. Each one of the six training directions corresponds to a given class. The features used as predictors in the implemented decision tree correspond to the quantized ADC output of each channel.

After the calibration phase, the decision tree with optimized hyperparameters, was generated by the central node of the system and then uploaded to the micro-controller of the LAILA board.

In figure 4.7 on page 131 are shown the results of the hyperparameters optimization procedure. Overall it was inferred that the optimum classifier is characterized by Twoing Rule as split criterion, minimum leaf size equal to 41 and maximum number of splits equal to 1690.

Subsequently, a second set of acquisitions, with the source moved in the same locations adopted in the training phase, was performed. During the acquisition of this test dataset, the μC performed in real time the

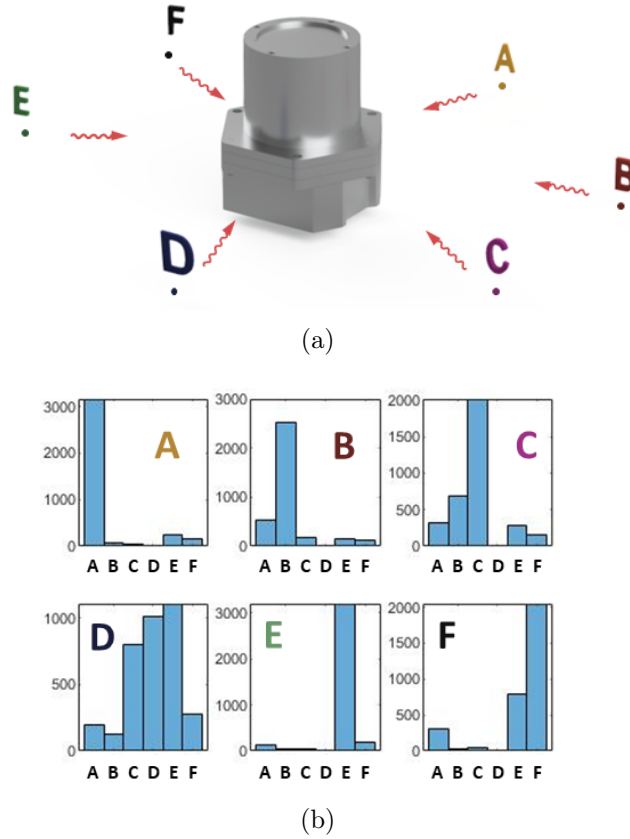
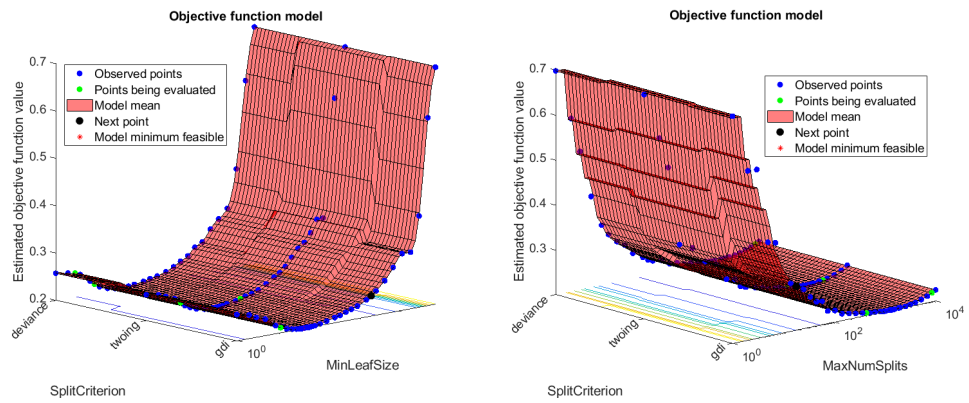


Figure 4.6: a) Schematic representation of the source positions scanned during the training phase: the ^{57}Co source is moved in 6 different positions equally spaced along the full circle in the detectors plane. b) Histograms of the classified outputs for events belonging to a second set of γ irradiations from the same positions adopted in the calibration phase.

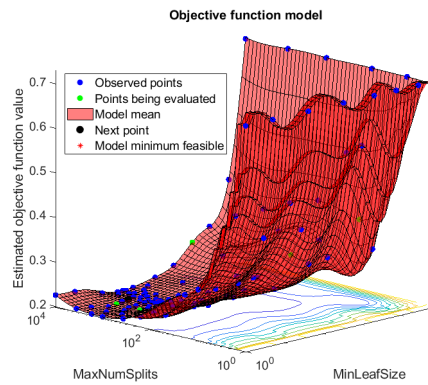
γ -ray direction reconstruction task, and then provided to the MATLAB environment the reconstructed class of each event together with the corresponding pixel signals.

In figure 4.6(b) the classified outputs histograms of the test dataset for each source position are shown.

It should be highlighted that most of the gamma photons generated when the source is in position D, interact with the crystal in close proximity to the detector area whose related channel has been excluded from the acquisition. This explains why the histogram corresponding to the D



(a) Split criterion - Minimum leaf size (b) Split criterion - Maximum number of splits



(c) Maximum number of splits - Minimum leaf size

Figure 4.7: *Hyperparameters optimization. The objective function corresponds to the complement of the algorithm accuracy (or cross-validation error). Increasing too much the leaf size or tree depths induces overfitting problems.*

position reveals a worse classification performance with respect to all the other cases, where the peak of the reconstructed classes correctly shifts towards right as the source is moved from position A to position F.

The confusion matrix, showing, on the main diagonal, the algorithm correct classification rate for each source position, is reported in figure 4.8.

A	86.0%	1.9%	1.3%	0.1%	6.3%	4.4%
B	14.8%	71.3%	5.2%	0.5%	4.4%	3.8%
C	9.5%	19.8%	57.9%	0.4%	8.0%	4.4%
D	5.5%	3.7%	22.7%	29.1%	31.2%	7.9%
E	3.3%	1.2%	1.5%	0.4%	88.1%	5.5%
F	9.3%	1.1%	1.2%	0.4%	24.5%	63.5%
	A	B	C	D	E	F

Predicted Direction

Figure 4.8: *Confusion matrix of the source position classification. The percentage on the main diagonal of the matrix indicates the relative number of correct classification. Elements close to the diagonal on the same row represent direction classes that are spatially adjacent to the real class.*

From the matrix it can be observed that, although one of the eight acquisition channels has been excluded from the training and the test dataset (inducing a correct classification rate lower than 30% for position D) the centroid of the reconstructed positions distribution correctly identifies the gamma source position for every class in the test dataset.

The input count rate for the spectrometer was about 1.5 kcps, only limited by the gamma source low activity. Thanks to the low computational complexity of the algorithm, the maximum acquisition rate of the system was not affected by the embedded classification.

Chapter 5

Conclusions and Future Developments

In this chapter conclusive considerations on the developed algorithms are presented, upon the obtained experimental results. Challenges and future perspective for the projects are discussed.

5.1 Conclusions

The contribution brought by the present thesis work to the three projects that have been addressed, together with the expected future development of the systems, are summarized in the following sections.

5.1.1 INSERT project

The first part of the work places itself in the last stages of INSERT Project, a European collaboration to implement a MR-compatible SPECT scanner aimed at enhancing the diagnosis of gliomas and monitoring their therapy. After the successful validation of the preclinical instrument (50 mm × 50 mm crystals and 10 modules) inside 3T MRI scanner, the characterization of the clinical instrument began.

In particular, in the framework of this master thesis, the depth of interaction (DOI) reconstruction, that can provide useful information to correct

the parallax error, was investigated through Monte Carlo simulations and through experimental measurements. Given the specific requirements of the system, the reconstruction method needs to be able to classify the DOI of the events in at least the bottom and the top half of the crystal. With regard to this, the results shown in the thesis are promising, as the proposed algorithm is able to distinguish four DOI groups in all the central region of the camera.

As a future development, the DOI reconstruction should be extended to the crystal lateral borders, where light reflection and asymmetry make the analysis more difficult.

Moreover, the validation with a tilted gamma beam with a higher degree of collimation is expected to bring the experimental results even closer to the simulated ones, thanks to a more precise correspondence between the real X and Z coordinates of gamma event interaction.

In addition, the possibility to calibrate the crystal (i.e. to generate the DOI LUTs) with only a flood field acquisition rather than with a grid collimator, can be investigated in order to reduce the overall calibration time, since the uniform irradiation can be performed for all the cameras simultaneously, without the need to interlock a specific collimator to the single modules.

5.1.2 GAMMA project

The second part of this thesis work is located in the context of GAMMA project, which consists of an innovative SiPM-based gamma detection module capable of replacing the PMTs in the readout of large Lanthanum Bromide crystals, obtaining results similar to those of PMTs in terms of energy and spatial resolution (3% FWHM and 1 cm respectively). The requirement in terms of spatial resolution comes from the necessity to compensate the Doppler broadening effect which affects the nuclear physics experiments where the GAMMA instrument is adopted.

In the framework of this master thesis, different algorithms for the position of interaction reconstruction of γ -rays inside the scintillator crystal

of the GAMMA system are presented. The first proposed reconstruction method is based on the cross-correlation between the average light distribution of calibration irradiations and the light distribution of each event that has to be reconstructed, and, tested on experimental measurements, provides a spatial resolution lower than 1 cm for the events near the center of the SiPM matrix and always below 1,5 cm when the interaction is closer to the lateral crystal surfaces.

Subsequently an in-depth study of the data distribution was carried out and the Principal Component Analysis (PCA) was performed for the dimensionality reduction and to identify which are the most important features of the problem. Eventually the K-Nearest Neighbours and Decision Tree machine learning reconstruction algorithms were tested on experimental measurements, giving similar results in terms of spatial resolution: lower than 1 cm for the events near the center of the SiPM matrix and below 1,5 cm when the interaction is closer to the lateral crystal surfaces. With these methods the percentage of events assigned to their true class is higher with respect to the cross-correlation case, therefore the mean value of the probability distribution is closer to its correct value. The Support Vector Machine algorithm has also been tested, however it was discarded since it is too slow without bringing significant improvement in the classification task.

Overall all the tested reconstruction ML algorithms give similar results in terms of classification accuracy. This could be due to the fact that a physical limit, for what regards the ability to distinguish scintillation events in different positions, may have been reached for the proposed SiPMs merging configurations. However the next step of the project will be to readout the 144-SiPM matrix coupling each SiPM with a dedicated ASIC input. The reconstruction capabilities of this system should be further investigated, even adopting other reconstruction approaches such as the ensemble classification or neural-network based algorithms. Indeed, since a different readout configuration, characterized by a large number of small pixels, is adopted, the reconstruction capabilities of the system are expected to be much higher. It should be reminded that in this context,

where the problem will be defined in a 144-dimensional space, the role of the PCA could become much more relevant if not fundamental for a fast and efficient position reconstruction.

5.1.3 Embedded Machine Learning

In the last part of this thesis work is presented an innovative system constituted by a micro-controlled based gamma spectrometer that is capable to reconstruct the direction of the interacting gamma photons and at the same time to move the position reconstruction algorithm computations from the central node to the peripheral ones, adopting embedded machine learning reconstruction directly in the external nodes of the system. The instrument that was employed as a prototype is the gamma spectrometer, based on a thick $\varnothing 3'' \times 3''$ lanthanum bromide ($\text{LaBr}_3(\text{Ce}^{3+})$) crystal coupled to a 144 NUV- HD SiPM array, developed in GAMMA project.

The goal is to embed the algorithms on the front-end micro-controller, allowing for a reduced dataset to be transferred when the source position is classified and distribution of computational complexity over the network for real-time operation when multiple spectrometers are used.

For the embedded direction reconstruction task the decision tree machine learning algorithm has been chosen since only a minimum amounts of data has to be stored and the classification time is short if the tree depths are kept small.

From the experimental validation, adopting a single spectrometer, the prototype was proven to be able to perform real-time localization of the gamma ray source with an accuracy always higher than 58%, with a peak of 88% for a specific gamma source position.

As a future development a more complex prototype, to experimentally validate the system in case multiple spectrometers are used, could be adopted: in this way it could be investigated how to carry out the optimum hyperparameters calibration procedure in the distributed architecture case and how each node setting should influence other nodes in the network.

Bibliography

- [1] Glenn F Knoll. *Radiation detection and measurement*. John Wiley & Sons, 2010 (cit. on pp. 2–4, 9, 17, 23).
- [2] F Scholze, H Rabus, and G Ulm. “Mean energy required to produce an electron-hole pair in silicon for photons of energies between 50 and 1500 eV”. In: *Journal of Applied Physics* 84.5 (1998), pp. 2926–2939 (cit. on p. 5).
- [3] INFN. *AGATA (Advanced Gamma Tracking Array) Project*. URL: <http://home.infn.it/it/approfondimenti/esperimenti/1368-agata> (cit. on p. 6).
- [4] Roberta Peloso et al. “Development of a detector based on Silicon Drift Detectors for gamma-ray spectroscopy for astronomy applications”. In: *2012 IEEE Nuclear Science Symposium and Medical Imaging Conference Record (NSS/MIC)*. IEEE. 2012, pp. 918–921 (cit. on p. 6).
- [5] P Dorenbos, J Th M de Haas, and CWE Van Eijk. “Non-proportionality in the scintillation response and the energy resolution obtainable with scintillation crystals”. In: *IEEE Transactions on Nuclear Science* 42.6 (1995), pp. 2190–2202 (cit. on p. 9).
- [6] Stefan Gundacker et al. “High-frequency SiPM readout advances measured coincidence time resolution limits in TOF-PET”. In: *Physics in medicine and biology* (2019) (cit. on p. 11).
- [7] Hal O Anger. “Scintillation camera”. In: *Review of scientific instruments* 29.1 (1958), pp. 27–33 (cit. on p. 11).

-
- [8] Osman Ratib and Thomas Beyer. *Whole-body hybrid PET/MRI: ready for clinical use?* 2011 (cit. on p. 14).
- [9] DJ Herbert et al. “Study of SiPM as a potential photodetector for scintillator readout”. In: *Nuclear Instruments and Methods in Physics Research Section A: Accelerators, Spectrometers, Detectors and Associated Equipment* 567.1 (2006), pp. 356–359 (cit. on pp. 16, 37).
- [10] M Grodzicka, M Moszyński, and T Szcześniak. “Silicon photomultipliers in gamma spectroscopy with scintillators”. In: *Nuclear Instruments and Methods in Physics Research Section A: Accelerators, Spectrometers, Detectors and Associated Equipment* (2018) (cit. on pp. 19, 31).
- [11] European Union Seventh Framework Programme. *Development of an integrated SPECT/MRI system*. URL: <http://www.insert-project.eu/> (visited on June 2019) (cit. on p. 19).
- [12] Brian F Hutton et al. “Development of clinical simultaneous SPECT/MRI”. In: *The British journal of radiology* 91.1081 (2018), p. 20160690 (cit. on p. 19).
- [13] Michele Occhipinti. “Development of a gamma-ray detection module for multimodal SPECT/MR imaging”. PhD thesis. Italy, 2015 (cit. on pp. 25, 45).
- [14] Paolo Trigilio. “Development of an ASIC for SiPM readout in SPECT applications”. In: (2016) (cit. on p. 25).
- [15] INFN. *GAMMA Project*. URL: <http://home.mi.infn.it/en/categoria-attivita-ricerca-eng/113-fisica-nucleare/683-gamma-eng.html> (cit. on p. 26).
- [16] N Blasi et al. “Position sensitivity in large spectroscopic LaBr₃: Ce crystals for Doppler broadening correction”. In: *Nuclear Instruments and Methods in Physics Research Section A: Accelerators, Spectrometers, Detectors and Associated Equipment* 839 (2016), pp. 23–28 (cit. on pp. 27, 30).

-
- [17] Giovanni L Montagnani et al. “GAMMA: an 8-channel High Dynamic Range ASIC for SiPM-Based Readout of Large Scintillators”. In: *2017 IEEE Nuclear Science Symposium and Medical Imaging Conference (NSS/MIC)*. IEEE. 2017, pp. 1–3 (cit. on pp. 28, 122, 123).
- [18] Matteo Grandi. “Development of GAMMA: a 16-channels high dynamic range readout ASIC for SiPMs”. MA thesis. Politecnico di Milano, Italy, 2018 (cit. on p. 28).
- [19] Valerio Gennari Santori. “FPGA-based data acquisition system for multichannel radiation detector instrumentation”. MA thesis. Politecnico di Milano, Italy, 2018 (cit. on p. 28).
- [20] Matteo Colugnat. “A compact detection module based on SiPMs, readout ASIC and DAQ: hardware and firmware development”. MA thesis. Politecnico di Milano, Italy, 2018 (cit. on p. 28).
- [21] A Giaz et al. “Investigation on gamma-ray position sensitivity at 662 keV in a spectroscopic 3” x 3” LaBr₃: Ce scintillator”. In: *Nuclear Instruments and Methods in Physics Research Section A: Accelerators, Spectrometers, Detectors and Associated Equipment* 772 (2015), pp. 103–111 (cit. on p. 29).
- [22] F Biocchi et al. “Position sensitivity of large volume LaBr₃: Ce detectors”. In: *2009 IEEE Nuclear Science Symposium Conference Record (NSS/MIC)*. IEEE. 2009, pp. 1403–1405 (cit. on p. 30).
- [23] Saint-Gobain. *Saint-Gobain Crystals Physical Properties of Common Inorganic Scintillators*. URL: https://www.crystals.saint-gobain.com/sites/imdf.crystals.com/files/documents/physical-properties-of-inorganic-scintillators_0.pdf (visited on Dec. 2018) (cit. on p. 31).
- [24] Alain Iltis et al. “Lanthanum halide scintillators: Properties and applications”. In: *Nuclear Instruments and Methods in Physics Research Section A: Accelerators, Spectrometers, Detectors and Associated Equipment* 563.2 (2006), pp. 359–363 (cit. on p. 32).

-
- [25] Saint-Gobain. *BrilLanCeTM 380 Material datasheet*. URL: https://www.crystals.saint-gobain.com/sites/imdf.crystals.com/files/documents/brilliance380-material-data-sheet_69765.pdf (visited on Dec. 2018) (cit. on p. 32).
- [26] Saint-Gobain. *Lanthanum Bromide and Enhanced Lanthanum Bromide datasheet*. URL: <https://www.crystals.saint-gobain.com/sites/imdf.crystals.com/files/documents/lanthanum-material-data-sheet.pdf> (visited on Dec. 2018) (cit. on pp. 32, 121).
- [27] Saint-Gobain. *BrilLanCeTM Scintillators Performance Summary*. URL: <https://www.crystals.saint-gobain.com/sites/imdf.crystals.com/files/documents/brilliance-scintillators-performance-summary.pdf> (visited on Dec. 2018) (cit. on p. 32).
- [28] Alan Owens et al. “Assessment of the radiation tolerance of LaBr₃:Ce scintillators to solar proton events”. In: *Nuclear Instruments and Methods in Physics Research Section A: Accelerators, Spectrometers, Detectors and Associated Equipment* 572.2 (2007), pp. 785–793 (cit. on p. 32).
- [29] Saint-Gobain. *Handling and Care of Crystal Scintillation Detectors*. URL: https://www.crystals.saint-gobain.com/sites/imdf.crystals.com/files/documents/handling-and-care-of-crystal-scintillation-detectors_70413.pdf (visited on May 2018) (cit. on p. 33).
- [30] Peter R Menge et al. “Eliminating Fractures in Large Lanthanum Bromide Crystal Packages”. In: *IEEE Transactions on Nuclear Science* 60.2 (2013), pp. 1039–1043 (cit. on p. 33).
- [31] Anna Camp, Arturo Vargas, and José M Fernández-Varea. “Determination of LaBr₃ (Ce) internal background using a HPGe detector and Monte Carlo simulations”. In: *Applied Radiation and Isotopes* 109 (2016), pp. 512–517 (cit. on p. 34).

-
- [32] R Nicolini et al. “Investigation of the properties of a 1" × 1" LaBr₃:Ce scintillator”. In: *Nuclear Instruments and Methods in Physics Research Section A: Accelerators, Spectrometers, Detectors and Associated Equipment* 582.2 (2007), pp. 554–561 (cit. on p. 34).
- [33] JK Hartwell and RJ Gehrke. “Observations on the background spectra of four LaCl₃ (Ce) scintillation detectors”. In: *Applied radiation and isotopes* 63.2 (2005), pp. 223–228 (cit. on p. 34).
- [34] Mikhail S Alekhin et al. “Improvement of γ -ray energy resolution of LaBr₃:Ce³⁺ scintillation detectors by Sr²⁺ and Ca²⁺ co-doping”. In: *Applied Physics Letters* 102.16 (2013), p. 161915 (cit. on p. 35).
- [35] M Moszynski et al. “A Comparative Study of Silicon Drift Detectors With Photomultipliers, Avalanche Photodiodes and PIN Photodiodes in Gamma Spectrometry With LaBr₃ Crystals”. In: *IEEE Transactions on Nuclear Science* 56.3 (2009), pp. 1006–1011 (cit. on p. 35).
- [36] Davide Di Vita. “Development of a 3" LaBr₃ SiPM-Based Detection Module for High Resolution Gamma Ray Spectroscopy and Imaging”. MA thesis. Politecnico di Milano, Italy, 2019 (cit. on p. 36).
- [37] Nepomuk Otte. “The silicon photomultiplier—a new device for high energy physics, astroparticle physics, industrial and medical applications”. In: *Proceedings of the IX International Symposium on Detectors for Particle, Astroparticle and Synchrotron Radiation Experiments*. 2006, pp. 1–9 (cit. on p. 37).
- [38] VD Kovaltchouk et al. “Comparison of a silicon photomultiplier to a traditional vacuum photomultiplier”. In: *Nuclear Instruments and Methods in Physics Research Section A: Accelerators, Spectrometers, Detectors and Associated Equipment* 538.1-3 (2005), pp. 408–415 (cit. on p. 37).
- [39] Debora Salvado et al. “Collimator design for a clinical brain SPECT/MRI insert”. In: *EJNMMI physics*. Vol. 1. 1. SpringerOpen. 2014, A21 (cit. on p. 41).

-
- [40] Michela Massara. “Processing methods for reconstruction of detected gamma events in a SPECT-MRI imaging system”. In: (2018) (cit. on pp. 41, 46).
- [41] T Ling, TK Lewellen, and RS Miyaoka. “Depth of interaction decoding of a continuous crystal detector module”. In: *Physics in Medicine & Biology* 52.8 (2007), p. 2213 (cit. on pp. 44, 51, 58, 59).
- [42] A Morozov et al. “ANTS2 package: simulation and experimental data processing for Anger camera type detectors”. In: *Journal of Instrumentation* 11.04 (2016), P04022 (cit. on p. 45).
- [43] NIST. *Photon cross section data for a single element, compound, or mixture*. URL: <https://physics.nist.gov/PhysRefData/Xcom/html/xcom1.html> (visited on Jan. 2019) (cit. on p. 46).
- [44] Roberto Pani et al. “A Novel Method for Gamma-photons Depth-of-Interaction Detection in Monolithic Scintillation Crystals”. In: *IEEE Transactions on Nuclear Science* 63.5 (2016), pp. 2487–2495 (cit. on pp. 51, 53).
- [45] VN Solovov et al. “Position reconstruction in a dual phase xenon scintillation detector”. In: *IEEE Transactions on Nuclear Science* 59.6 (2012), pp. 3286–3293 (cit. on pp. 58, 64).
- [46] Robert S Miyaoka, Sung-Kwan Joo, and Kisung Lee. “Detector light response modeling for a thick continuous slab detector”. In: *Journal of nuclear science and technology* 45.7 (2008), pp. 634–638 (cit. on p. 58).
- [47] A Morozov et al. “Iterative reconstruction of detector response of an Anger gamma camera”. In: *Physics in Medicine & Biology* 60.10 (2015), p. 4169 (cit. on p. 64).
- [48] A Morozov et al. “Iterative reconstruction of SiPM light response functions in a square-shaped compact gamma camera”. In: *Physics in Medicine & Biology* 62.9 (2017), p. 3619 (cit. on p. 64).

-
- [49] M Carminati et al. “Study of Position Sensitivity of Large LaBr 3: Ce Scintillators Readout by SiPMs”. In: *2017 IEEE Nuclear Science Symposium and Medical Imaging Conference (NSS/MIC)*. IEEE. 2017, pp. 1–3 (cit. on pp. 76–78).
- [50] GL Montagnani et al. “Development of 3" LaBr 3 SiPM-Based Detection Modules for High Dynamic Range Gamma Ray Spectroscopy and Imaging”. In: *2018 IEEE Nuclear Science Symposium and Medical Imaging Conference Proceedings (NSS/MIC)*. IEEE. 2018, pp. 1–2.
- [51] Tom Dietterich. “Overfitting and undercomputing in machine learning”. In: *ACM computing surveys* 27.3 (1995), pp. 326–327 (cit. on p. 91).
- [52] Saint-Gobain. *Absorption efficiency of BrillanCe™ 380 (LaBr₃(Ce))*. URL: <https://www.crystals.saint-gobain.com/sites/imdf.crystals.com/files/documents/efficiency-calculations.pdf> (visited on Nov. 2019) (cit. on p. 105).
- [53] A. Gola et al. “NUV-sensitive silicon photomultiplier technologies developed at Fondazione Bruno Kessler”. In: *Sensors* 19.2 (2019), p. 308 (cit. on p. 121).
- [54] G.L. Montagnani et al. “Spectroscopic performance of a Sr co-doped 3" LaBr₃ scintillator read by a SiPM array”. In: *Nuclear Instruments and Methods in Physics Research Section A: Accelerators, Spectrometers, Detectors and Associated Equipment* 931 (2019), pp. 158–161 (cit. on p. 121).
- [55] G. L. Montagnani et al. “A Compact 4-Decade Dynamic Range Readout Module for Gamma Spectroscopy and Imaging”. In: *2019 IEEE International Symposium on Circuits and Systems (ISCAS)*. IEEE. 2019, pp. 1–5 (cit. on p. 122).

List of Abbreviations

AGC	Amplitude Gain Control
ANTS2	Anger camera type Neutron detector: Toolkit for Simulations
APD	Avalanche Photodiode
ASIC	Application Specific Integrated Circuit
CERN	Conseil européen pour la recherche nucléaire
CMOS	Complementary Metal-Oxide Semiconductor
CT	Computerized Tomography
DAQ	Data Acquisition
DCR	Dark Count Rate
DOI	Depth Of Interaction
DR	Dynamic Range
ENF	Excess Noise Factor
FBK	Fondazione Bruno Kessler Fondazione Bruno Kessler is a research non-profit public interest entity located in Trento, Italy. www.fbk.eu
FBP	Filtered Back-Projection

FOV	Field Of View
FPGA	Field Programmable Gate Array
FWHM	Full Width at Half Maximum
GM-APD	Geiger Mode Avalanche Photodiode
INFN	Istituto Nazionale di Fisica Nucleare Founded on 8th August 1951, the National Institute for Nuclear Physics (INFN) is the Italian research agency dedicated to the study of the fundamental constituents of matter and the laws that govern them, under the supervision of the Ministry of Education, Universities and Research (MIUR). It conducts theoretical and experimental research in the fields of subnuclear, nuclear and astroparticle physics. home.infn.it
K-NN	K-Nearest Neighbours
LAILA	Large dynamic range Acquisition Interface for Lanthanum bromide crystals
LRF	Light Response Function
LUT	Lookup Table
ML	Machine Learning
MLE	Maximum Likelihood Estimation
MRI	Magnetic Resonance Imaging
MSS	Multi-mini Slit-Slat
OSEM	Ordered Subset Expectation Maximization
PCA	Principal Component Analysis
PCB	Printed Circuit Board
PDE	Photon Detection Efficiency

PERA	Planar Event Reconstruction Algorithm
PET	Positron Emission Tomography
PMT	Photomultiplier Tube
PSPMT	Position Sensitive Photomultiplier Tube
SDD	Silicon Drift Detector
SiPM	Silicon Photomultiplier
SNR	Signal to Noise Ratio
SPAD	Single Photon Avalanche Diode
SPECT	Single Photon Emission Tomography
SVM	Support Vector Machine
TOF-PET	Time Of Flight PET
UFOV	Useful Field Of View